1-1-2012

Effects of transition metal doping on multiferroic ordering in ni3v2o8 and fevo4

Akila Deeghayu Kumarasiri
Wayne State University,

EFFECTS OF TRANSITION METAL DOPING ON MULTIFERROIC ORDERING IN $Ni_3V_2O_8$ AND $FeVO_4$

by

AKILA KUMARASIRI

DISSERTATION

Submitted to the Graduate School

of Wayne State University,

Detroit, Michigan

in partial fulfillment of the requirements

for the degree of

DOCTOR OF PHILOSOPHY

2012

MAJOR: PHYSICS

Approved by:

_____
Advisor   Date

_____

_____

_____

ACKNOWLEDGEMENTS

This thesis and the related research work would not have been possible without the support of a group of remarkable people who have guided and assisted me both on a professional level and a personal level during my time at the Wayne State University. First and foremost, I'm truly grateful to my advisor Dr. Gavin Lawes, whose support during the last four years of research work at Wayne State Physics has been invaluable to me. His constant guidance and suggestions, and his uncanny ability to approach a problem logically and methodically have helped me in countless occasions. His help in editing and consultation that went into completing this thesis was also instrumental. Secondly, I'm grateful to Dr. Ratna Naik, my dissertation committee member and department chair, for her constant support throughout these years. Her advice and constant looking out for the well-being of the students is greatly appreciated. I'd also like to thank Dr. Zhixian Zhou and Dr. Matthew J. Allen for their support and advice as my dissertation committee members, as well as allowing me to use the facilities in their labs for some of the sample preparations and characterization.

I'd also like to thank the graduate advisor Dr. Jogindra Wadehra who was always available to discuss any issues, and my teachers at WSU Physics, Drs. Paul Keyes, J. J. Chang, Robert Harr, Paul Karchin, Caroline Morgan, and William Rolnick. I am deeply grateful to Dr. Parashu Kharel, Dr. Ambesh Dixit, Dr. Rajesh Regmi, and Dr. Chandran Sudakar who helped me immensely in learning new techniques and adapting to new instruments when I started out my research in the lab. I'm also grateful to my current lab mates Maheshika Perera, Ehab Hamdy, Suvra Laha, and all my friends at Wayne State Physics for their support.

TABLE OF CONTENTS

LIST OF FIGURES

x

CHAPTER 1

INTRODUCTION

One of the most discussed themes in current materials science research is the study of complementary functionalities in the same system. Within this broad effort, there is considerable interest in understanding the materials properties underlying the development of simultaneous ferroic orders in materials. Four ferroic orders are currently known, which are characterized by the formation of domains and therefore showing hysteresis behavior in a field- response loop. Ferromagnetism is the most commonly observed ferroic order, where a spontaneous non-zero magnetization develops even in the absence of an external magnetic field. Similarly, ferroelectric materials develop a spontaneous electrical polarization even in the absence of an external electrical field. In addition to ferromagnetism and ferroelectricity, two other ferroic orders exist; a ferroelastic material exhibits a spontaneous stretching without applying an external strain, and a ferrotorroidic material shows a spontaneous development of magnetic vortices. Figure 1.1 shows these four ferroic orders under the parity operations of space and time. Ferromagnetic order parameter breaks time reversal symmetry, while ferroelectric order parameter breaks the spatial inversion symmetry. Ferrotorroidicity breaks both symmetries, while ferroelasticity is invariant under both time and space reversal.

If a material exhibits two or more of these ferroic orders simultaneously, such a material is known as a multiferroic. The most interesting and functional multiferroics are those where the two ferroic orders are coupled. If this coupling is between ferromagnetism and ferroelectricity, it

is referred to as magnetoelectric coupling, and such a material is known as a magnetoelectric multiferroic.
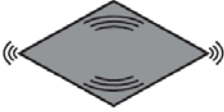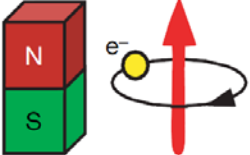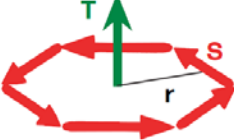
Figure 1.1: All forms of ferroic orders under the parity operations of space and time [1]

Magnetoelectric multiferroic materials have attracted considerable interest in recent years. Aside from the fundamental importance of understanding the coexistence of multiple ferroic orders, the possibility of mutual control of electric and magnetic properties provide the opportunity for developing new applications in magnetic storage and spintronics [2, 3]. Since a ferromagnetic material will show hysteresis in an M-H loop and a ferroelectric material will show hysteresis in a P-E loop, a magnetoelectric multiferroic will have an overlap of these properties where the magnetic (electric) polarization can be induced by applying an external electric (magnetic) field, as shown in figure 1.2. Since an electric field is much easier to apply than a magnetic field, switchable at a much faster rate, and inherently has low energy consumption, it is desirable to use an electric field rather than a magnetic field in device

development. Multiferroics provide the possibility of utilizing electrically switchable magnetic properties, and alternately magnetically switchable polarization in developing potential devices.
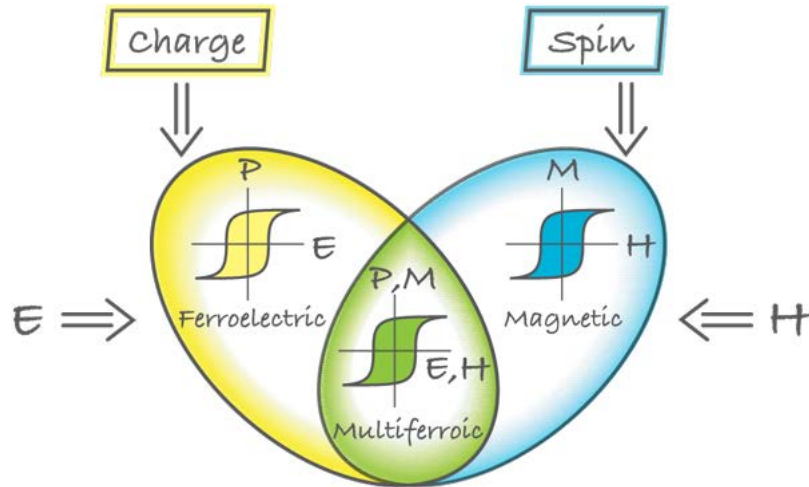
Figure 1.2: Magnetoelectric multiferroics combine ferroelectric and ferromagnetic properties [4]

Although a number of multiferroic materials have been identified and studied, due to the inherently exclusive nature of the development of ferromagnetic and ferroelectric orders, the coupling between these two properties for most multiferroics remain small. For use in device development, mutual control of electric and magnetic properties can be achieved only through materials that show strong coupling between these two properties. Hence, understanding and tuning the properties of such materials has recently been a topic of great interest. In this thesis, a systematic doping study done on studying the multiferroic behavior of two strongly coupled magnetoelectric multiferroic materials; $Ni_3V_2O_8$ and $FeVO_4$ will be presented. Doping is often used as a tool to perturb the magnetic lattices of these materials, and how the introduction of

different spins into the lattice changes the multiferroic ordering as well as the magnetic phase transitions are studied.

$Ni_3V_2O_8$ is a geometrically frustrated Kagome staircase system which develops strongly coupled ferroelectric and antiferromagnetic order simultaneously at T = 6.3 K, and has a rich magnetic phase diagram due to a multitude of different competing magnetic interactions [5,6]. It provides a great platform for investigating doping effects in multiferroics since the spin structures and phase diagram for this material are well understood, and there is only one magnetic ion present. We investigated how the magnetic phases of $Ni_3V_2O_8$ were affected through systematic doping of transition metal ions, both magnetic (Zn) and non-magnetic (Cu, Co, Fe, Mn). $FeVO_4$ is a recently discovered multiferroic [7,8] which develops multiferroic ordering at T= 15 K. $FeVO_4$ also has only one magnetic ion, but the lattice however has a very low symmetry, unlike $Ni_3V_2O_8$ which has a high symmetry Ni^{2+} lattice. In this study, both these materials were studied through perturbation of their magnetic lattice by introducing non-magnetic and magnetic dopants into the lattice, and studying how the multiferroic ordering as well as the other magnetic ordering temperatures changes.

This thesis contains three main parts; an introduction to multiferroics and a literature review, the experimental procedure including data analysis, and finally a discussion and future work. In chapter 2, basic concepts of ferromagnetism and ferroelectricity, including the underlying principles of development of multiple ferroic orders in a material are discussed. Chapter 3 is dedicated to reviewing the previous work done on different multiferroics, with the main focus on the two materials under study in this thesis: $Ni_3V_2O_8$ and $FeVO_4$.

Chapters 4 through 7 present the experimental work. Chapter 4 discusses the synthesis of the ceramic $Ni_3V_2O_8$ and $FeVO_4$ samples, and the characterization techniques used including X-ray diffraction, Raman Spectroscopy and Energy Dispersive Spectroscopy.

Chapter 5 discusses the non-magnetic Zn doping of $Ni_3V_2O_8$, where $Ni_{1-x}Zn_xV_2O_8$ samples are synthesized for x=0 to x=0.3, and the magnetic transitions are studied using magnetization, dielectric, pyrocurrent and heat capacity measurements. A doping fraction vs. temperature phase diagram is also constructed and discussed in view of Ising and Heisenberg spin models. Chapter 6 continues this discussion with the study of magnetic dopants. $Ni_{1-x}M_xV_2O_8$ for M = Cu, Co, Fe, and Mn is studied, and a combined phase diagram for transition metal doping of $Ni_3V_2O_8$ is created.

Chapter 7 discusses the non-magnetic (Zn) and magnetic (Cr and Mn) doping of $FeVO_4$. The final chapter, chapter 8, compares and discusses the behavior of both $Ni_3V_2O_8$ and $FeVO_4$ under these different dopants, while discussing the possible future work that could be done. The appendix contains separate work done on Gd_2O_3 nanoparticles; how post synthesis heat treating modifies the crystallinity and magnetic properties of these nanoparticles.

CHAPTER 2

FUNDAMENTAL PROPERTIES OF MULTIFERROICS

2.1 Origin of Magnetism

Magnetism is known to exist in many different forms and origins of these forms have been a challenge to understand for centuries. All materials can be broadly divided into two categories; materials which show long range magnetic ordering, and materials that do not. The materials that do not show long range magnetic order and in turn do not possess a net permanent magnetic moment can be split into two classes, paramagnets and diamagnets. If the magnetization of the material is **M** in an applied magnetic field **H**, the *Magnetic Susceptibility* (χ) for a linear media can be defined as

$$\chi = \mathbf{M} / \mathbf{H} \qquad\qquad (2.1)$$

Depending on the sign of χ, materials are divided into the two categories mentioned above; a material with a positive magnetic susceptibility is referred to as a paramagnetic material while a material with a negative magnetic susceptibility is referred to as a diamagnetic material.

2.1.1 Paramagnetism

In a paramagnetic material, an atom will have a permanent magnetic moment due to the net spin from the unpaired electrons. Minimizing the free energy in a system requires a combination of the highest entropy and the lowest energy, so sufficient thermal motion can cause

the spins to align randomly (fig 2.1 (a)). In equilibrium, the dynamically fluctuating spins will cancel each other out resulting in a zero net magnetization. However, when an external magnetic moment is applied, these spins will interact with the external field and align along the field to help minimize their internal energy, which will produce a net magnetic moment in the system as shown in figure 2.1 (b).

M = 0

(a)

M ≠ 0

(b)
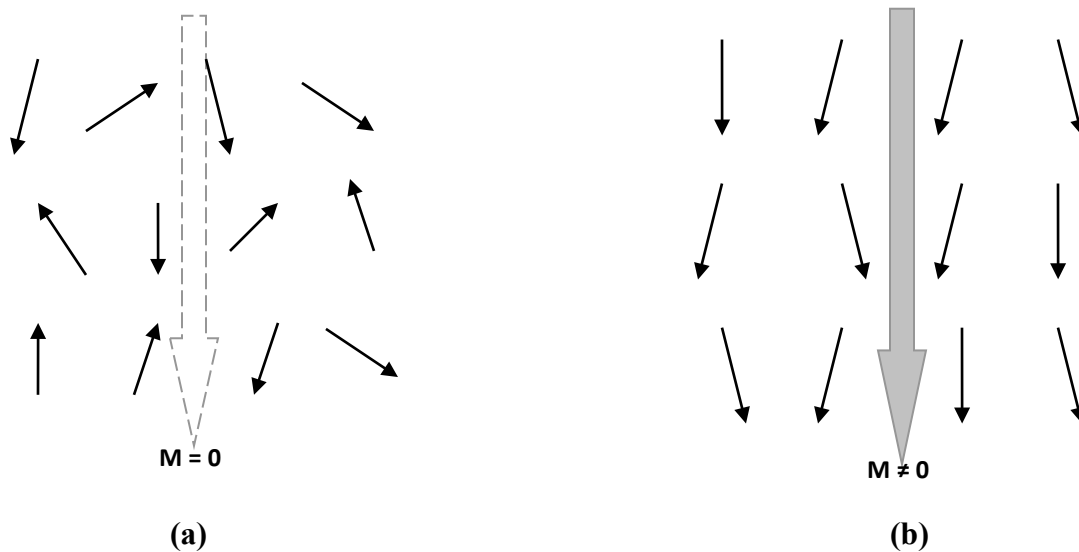
Figure 2.1: (a) In a paramagnetic material, random alignment of spins leads to M=0 at thermal equilibrium (b) under an external field, spins align in the general direction of the field in the material and leads to M ≠ 0

2.1.2 Diamagnetism

Unlike paramagnetism which arises from unpaired electrons, diamagnetism occurs when the atom has completely filled shells so the ground state will have zero orbital angular momentum and zero spin. When an external field is applied, it alters the electron kinetic energy

and thus their angular momentum. This leads to a change in the magnetic dipole moment to oppose the applied field, while the spin remains zero which leads to a net magnetic moment opposite to the applied field. This mechanism is typically much weaker than the effects giving rise to paramagnetism. Consequently, the magnetic susceptibilities of diamagnetic materials are much smaller than those of paramagnetic materials. As an example, water which is diamagnetic, has $\chi = - 8 \times 10^{-6}$, while $CuSO_4$ which is paramagnetic, has $\chi = 3.8 \times 10^{-4}$.

2.1.3 Magnetic Ordering in Solids

Both paramagnetism and diamagnetism are defined by the response to an external field. However, some materials spontaneously develop long range magnetic ordering which in turn may produce non-zero net magnetization even in the absence of an external field. Figure 2.2 shows the three simplest types of magnetic ordering along with some of the more complex non-collinear ordering. If all of the magnetic atoms are aligned in the same direction so that they add to give the net magnetization, the material is a ferromagnet. If the moments are aligned with antiparallel orientations to give a zero net magnetization, the material is an antiferromagnet. Antiferromagnetism occurs in multiple forms. For example, in G-type cubic antiferromagnets every nearest neighbor is antiferromagnetically coupled, while in A-type antiferromagnets each adjacent layer of spins can be antiferromagnetically coupled with adjacent spins in a single layer being ferromagnetically coupled. If the moments are aligned with antiparallel orientation but still give a non-zero net magnetization the material is a ferrimagnet. Ferrimagnetic order can develop when the neighboring moments have different magnitudes.
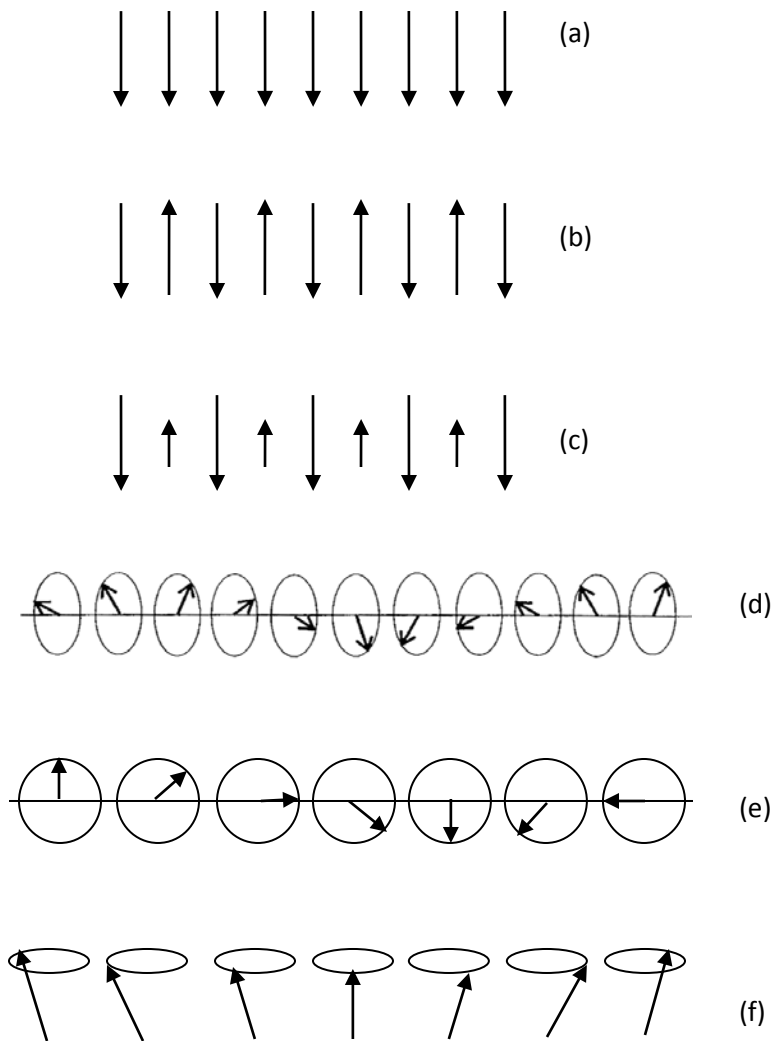
Figure 2.2: Simple magnetic ordering types (a) ferromagnetic ordering (b) antiferromagnetic ordering (c) ferrimagnetic ordering (d) helical ordering (e) cycloidal ordering (f) spin spirals

In addition to these simple anti/ferro/ferrimagnetic structures, non-collinear spin structures like helical ordering (figure 2.2 (d)), cycloidal ordering (figure 2.2 (e)) or spin spirals (figure 2.2 (e)) can also develop, particularly when longer range interactions (next nearest neighbor, etc.) become relevant. These can be considered as a special case of antiferromagnetic

order since the net moment would still be zero over a large volume. Geometrical frustration (which will be discussed later) of antiferromagnets can also lead to non-collinear ordering. There are also materials that develop incommensurate order, which have long range ordering of spins, however, the periodicity is not commensurate (i.e. not a rational multiple) with the crystal structure.

2.1.4 Exchange Interaction

It has been long known that magnetic interactions play the pivotal role in allowing the magnetic moments to spontaneously arrange into a long range order, however Classical models have failed to explain long range magnetic ordering sufficiently. If two classical magnetic dipoles μ_1 and μ_2 are separated by a distance r, the corresponding energy of interaction can be written as;

$$\mathrm{E} = \frac{\mu_0}{4\pi r^3}\left[\mu_1 . \mu_2 - \frac{3}{r^2}(\mu_1.\boldsymbol{r})(\mu_2.\boldsymbol{r})\right] \tag{2.2}$$

However, if two typical magnetic dipoles $\mu_1 = \mu_2 = 1$ μ_B that are separated by r $= 10^{-10}$ m are considered, the interaction energy according to the above equation is roughly 10^{-23} J, which is equivalent to less than 1 K in temperature [9] . This clearly indicates that if classical magnetic dipole interaction is responsible for magnetic ordering, no material will have an ordered magnetic structure above a few Kelvin. However, as a large number of observed anti/ferromagnetic materials have Neel/Curie temperatures well above the room temperature, it becomes evident that magnetic dipole interaction alone is much too weak to account for magnetic ordering.

It is now understood that magnetism is purely a quantum mechanical phenomenon, arising due to exchange interaction. To properly explain magnetic properties including paramagnetism and diamagnetism and why ferromagnets exhibit a permanent magnetic moment it is necessary to consider the concept of spin. First considered by Wolfgang Pauli in 1924, quantum mechanical spin can take only integer or half integer values when measured along specific directions. The magnitude of the spin in a system is given by $S = \hbar\,[s(s+1)]^{1/2}$ where s is the spin quantum number and $\hbar = h/2\pi$ with h being Planck's constant. The spin quantum number is a fundamental intrinsic property of elementary particles. Electrons have spin $s = \frac{1}{2}$ making them Fermions. Because of this quantum mechanical spin, an electron will have a quantum mechanical dipole moment given by $\mu = gS\,(q/2m)$ where g is the Lande g-factor, m is the mass and q is the charge.

$$\psi\,(\mathbf{r}_1, \mathbf{s}_1 : \mathbf{r}_2, \mathbf{s}_2) = -\,\psi\,(\mathbf{r}_2, \mathbf{s}_2 : \mathbf{r}_1, \mathbf{s}_1) \qquad (2.3)$$

Since the electron is a spin $\frac{1}{2}$ Fermion, the total wave function of a pair of electrons is always anti-symmetric under the exchange of the two electrons, as given by equation 2.2. The allowed states of the electrons are governed by Fermi-Dirac statistics and the Pauli Exclusion Principle. When the spin and spatial coordinates are exchanged, the wave function vanishes for identical spatial and spin components, so there is no possible way for two electrons with same spin to exist at the same spatial coordinates. Parallel spins will therefore be found further apart and will have a smaller Coulomb repulsion energy than anti-parallel spins (which can be in close proximity) due to the anti-symmetric nature of the wave function.

The exchange energy decreases rapidly as the distance between the atoms is increased. In reality, several magnetic atoms with many electrons will interact and the net effect of these couplings can be described by the Heisenberg Hamiltonian given by equation 2.4. Here J_{ij} is the exchange energy.

$$H = -\sum_{i}\sum_{j\neq 1}J_{ij}S_iS_j \tag{2.4}$$

The sign and magnitude of J depends on the specific details of how the electron wave functions overlap. In local moment magnets, the sign of J from superexchange (discussed in section 2.1.6) is determined by the Goodenough-Kanamori rules [10, 11, 12] which are based on the symmetry and electron occupation of the overlapping atomic orbitals. According to these rules, the bond angle between two magnetic ions (M) separated by an intermediate non-magnetic ion (for example O^{2-}) will govern the sign of J and hence the type of magnetic ordering. An M-O-M bond angle of 180° will lead to antiferromagnetic coupling while a bond angle of 90° will lead to ferromagnetic coupling. In addition, superexchange interactions between two magnetic ions with-half-occupied orbitals through an intermediary non-magnetic ion will lead to antiferromagnetic ordering while ferromagnetic ordering will be preferred if one magnetic ion has an empty orbital and the other a half filled orbital, or alternately if one magnetic ion has a full orbital and the other a half filled orbital.

Exchange interaction in solids can have several different mechanisms, and are discussed in sections 2.1.5 to 2.1.8.

2.1.5 Direct Exchange

When the electrons in the nearest neighboring magnetic atoms directly interact with each other, it is known as direct exchange. Direct exchange is relevant only when there is a sufficiently large overlap of the electronic wavefunctions of the neighboring magnetic atoms. Often, direct exchange plays a small role because many materials do not possess this overlap. For example, many insulators possess strongly localized wavefunctions where the exchange integral becomes small. Similarly, rare earth metals have strongly localized 4f electrons, making direct exchange insignificant. Even in some of the transition metals (Ni, Co, etc.) which have 3d orbitals extending further from the nucleus, direct exchange is not enough to explain their magnetic properties.

2.1.6 Superexchange

Some materials have effective magnetic interactions between non-nearest neighbor magnetic ions through a non-magnetic ion sandwiched between its two magnetic neighbors. This indirect exchange interaction mechanism in a solid is known as Superexchange. Superexchange occurs when the electron can reduce its kinetic energy by delocalizing over the bond and couple antiferromagnetically. As shown in figure 2.3, each transition metal has a single unpaired d electron and if the oxygen has two p electrons, antiferromagnetic coupling will lower the energy of the system through allowing the electrons to delocalize through the whole bond.
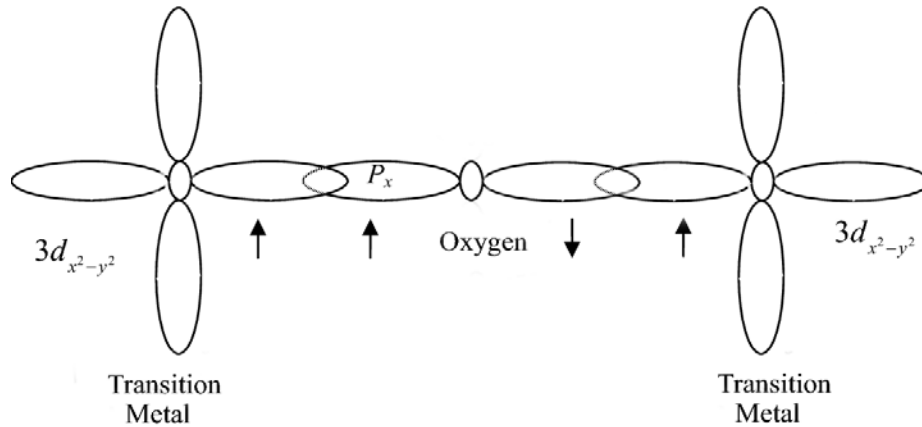
Figure 2.3: Superexchange between two antiferromagnetically coupled transition metal ions

2.1.7 RKKY interaction

In a metal, the exchange interaction mechanism varies as the exchange interaction between the d or f shell electrons in the magnetic ions will be modulated by the conduction electrons in the metal. This mechanism is named after its founders Ruderman, Kittel, Kasuya and Yosida, and is known as RKKY interaction [13]. The sign of this interaction oscillates with the distance between magnetic ions and depends on the Fermi energy.

2.1.8 Double Exchange

Double exchange is observed in materials that show mixed valency (as often observed in Mn^{3+}/Mn^{4+} materials). For example consider the following Mn-O-Mn bond. The ability of an electron to be exchanged between the two Mn ions will oversee whether the material is ordered ferromagnetically or antiferromagnetically. In this case, the electron in the e_g state of Mn^{3+} can hop to the neighboring Mn^{4+} if it has a vacancy in the e_g state and if both are coupled

ferromagnetically. If the two are antiferromagnetically coupled, this hopping is energetically unfavorable and will be suppressed by Hund's rules.
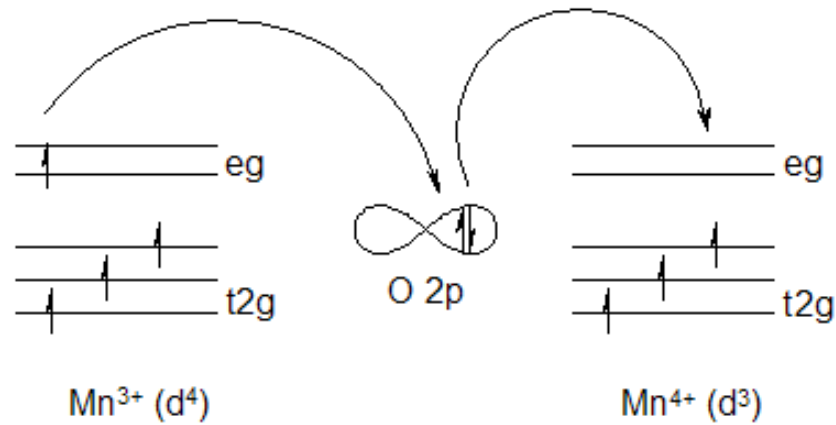
Figure 2.4: Double exchange between two ferromagnetically coupled Mn^{3+}/Mn^{4+} ions

2.1.9 Anisotropic Exchange Interaction

Direct exchange, superexchange and double exchange are all modeled by equation 2.4 which has a scalar $(S_1 \cdot S_2)$. However, when spin-orbit interaction plays a role and if the crystal structure breaks the spatial inversion symmetry, a vector term $(S_1 \times S_2)$ can appear in the Hamiltonian. This anisotropic exchange interaction is known as Dzyaloshinski-Moriya interaction and the Hamiltonian is given by

$$H = -\sum_i \sum_{j \neq 1} D_{ij} \cdot (S_i \times S_j)$$

(2.5)

Here the vector D vanishes if the crystal field has inversion symmetry with respect to the two magnetic ions, and is the source of the anisotropy. In general D will not vanish and will

depend on the symmetry, and will lie parallel or perpendicular to the line connecting the two spins.

Similar to magnetic ordering seen in ferromagnetic materials, in some materials the structural distortions will lead to non-zero ferroelectric polarization even in the absence of an external electric field. Many properties of ferroelectric materials are analogues to the properties of ferromagnets, with the electric field **E** corresponding to magnetic field **H,** and the polarization acting as the order parameter as opposed to magnetization in ferromagnetic materials [14, 15]. Origins of ferroelectric ordering in multiferroics will be discussed in more detail in section 2.3.

2.2 Types of multiferroics

As discussed in chapter 1, a material which shows anti/ferromagnetism and ferroelectricity simultaneously (i.e. in the same phase) is known as a multiferroic. A need for the classification of different multiferroics has become necessary as different mechanisms give rise to the ferroelectric order observed in multiferroic materials. Therefore, multiferroics have been broadly classified into two categories depending on the origin of the multiferroic order; type-I multiferroics and type-II multiferroics [4].

2.2.1 Type-I Multiferroics

Magnetic ordering and ferroelectric ordering exist independently in type-I multiferroics, and hence they show well separated magnetic and ferroelectric ordering temperatures. These materials have fairly weak coupling of ferroelectricity and ferromagnetism, as the origins of magnetic and ferroelectric properties are independent. These materials usually exhibit large

polarization and ferroelectricity is usually observed at higher temperatures than magnetism. These can be a composite of ferromagnetic and ferroelectric material, as in the case of $CoFe_2O_4$ and $BaTiO_3$ [16], or individual materials like $YMnO_3$ [17] or $BiFeO_3$ [18], the only known room temperature multiferroic.

2.2.2 Type-II Multiferroics

Type-II multiferroics have strong coupling, where a clear change in polarization can be observed with an externally applied magnetic field. In these systems, ferroelectricity and ferromagnetism comes from the same source. Here, magnetic ordering usually drives the ferroelectric order, and the magnetic ordering temperature usually coincides with the ferroelectric ordering. Well known multiferroics that belong to type-II are $TbMnO_3$ [19], $Ni_3V_2O_8$ [5, 6, 20, 21] and $FeVO_4$ [7, 8, 22], of which the latter two are the focus of this thesis.

The simultaneous existence of ferroelectricity and ferromagnetism is often hindered by physical restrictions. Typically, magnetic ordering requires localization of electrons into partially filled d (or f) shells and is usually seen in transition metals or rare earth metals. Conversely, electrical polarization requires a structural distortion of the lattice occurring usually from empty d shells, and ferroelectrics tend to be insulators. Hence the co-existence of both orders is rare, and generally occurs when the electrical polarization (or magnetic ordering, although unusual) finds an alternate microscopic mechanism [23].

2.3 Origin of ferroelectricity in type-I Multiferroics

Depending on the type of the multiferroic, the onset of ferroelectricity can have multiple origins. Since ferroelectricity is independent from the magnetic ordering in type-I multiferroics, the underlying mechanism of ferroelectric ordering is also independent, while in type-II multiferroics, the magnetic ordering drives the ferroelectric ordering.

2.3.1 Ferroelectricity due to lone pairs

Lone pair driven multiferroic behavior is observed in type-I multiferroics like $BiFeO_3$ and $BiMnO_3$ [24, 25] where the ferroelectric ordering temperature is much higher than the magnetic ordering temperature. Since type-I multiferroics have different sources of origins for magnetic and ferroelectric ordering, it can be anticipated that these materials will show weak coupling between the two properties. In $BiFeO_3$ or $BiMnO_3$, the Fe ion or Mn ion will exhibit the long range magnetic order. However they do not contribute to the ferroelectric behavior, which is in fact a direct result of the "lone pair" of $6S^2$ electrons on the larger Bi^{3+} ion. The Bi^{3+} ion is displaced from the center with respect to the oxygen neighbors due to the activity of the unstable lone pair of electrons. This lattice distortion breaks the spatial inversion symmetry and introduces ferroelectricity into the system.

2.3.2 Ferroelectricity due to charge ordering

In some multiferroics, ferroelectricity can be caused by charge ordering. This is mostly seen in type I multiferroics, examples being $LuFe_2O_4$ [26] and the perovskite $(PrCa)MnO_3$ [27].

However, this can also be observed in type II multiferroics like RMn_2O_5 [28] which has inequivalent bond lengths in the lattice synonymously with ions of different charges. The mechanism by which charge ordering induces ferroelectricity can be explained using figure 2.5 [29]
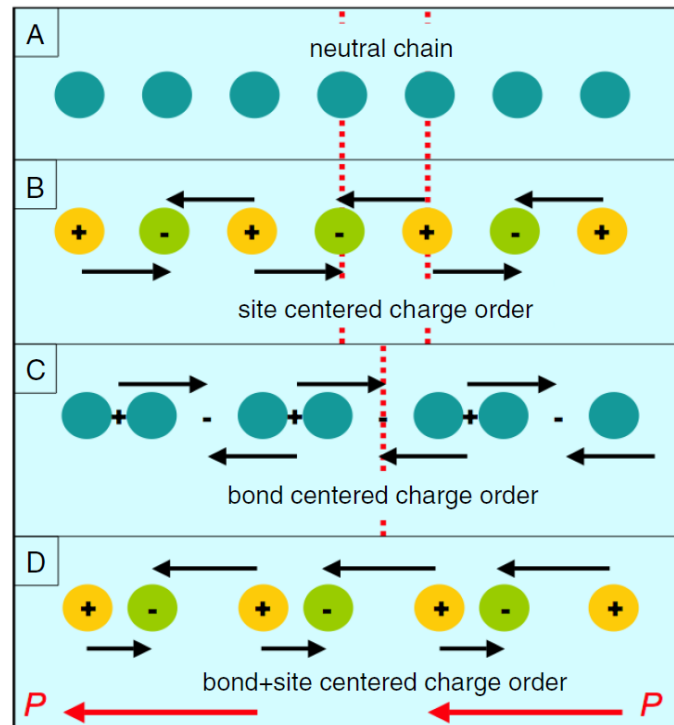
Figure 2.5: (A) A neutral 1-dimensional chain which exhibits (B) site-centered charge ordering, (C) bond-centered charge ordering and (D) a linear combination of these two that is ferroelectric; taken from [29]

If a neutral 1-dimensional chain undergoes a charge ordering where the sites will become inequivalent (but bonds will remain the same) and will contain alternate positive and negative charges as shown in figure 2.5 (b), this chain will still retain the spatial inversion symmetry and hence will not show ferroelectric behavior. Alternately, as shown in figure 2.5 (c), if the chain

dimerizes where the sites remain equivalent but bonds will change and alternate between strong and weak bonds, the chain is still centrosymmetric and will still not show ferroelectricity. However, if these two processes combine in a system as shown in figure 2.5 (d) and changes both sites and bonds, spatial inversion symmetry is broken and a polarization can be observed as indicated by the red arrows. This mechanism is commonly observed in systems which have mixed valence transition metal ions, Mn^{3+}/Mn^{4+} systems being common examples.

2.3.3 Geometric Ferroelectricity

An example for geometric ferroelectricity is the RMnO3 family (R=Y, Sc) which has been studied comprehensively recently. For example, in $YMnO_3$ the cause is the rotation of rigid MnO_5 polyhedra in combination with the unusual coordination of the Y ions [17]. This rotation leads to the formation of electrical dipoles which lead to the onset of ferroelectric behavior seen in these type I multiferroics. A recent theoretical study based on first principle has suggested that hexagonal $RGaO_3$ and $RInO_3$ may also show geometric ferroelectricity [30]. However, the underlying mechanism of geometric ferroelectricity is still not fully understood.

2.4 Origin of ferroelectricity in type-II Multiferroics

All 3 of the previously discussed mechanisms for ferroelectric ordering occur in type I multiferroics, where the ferroelectricity is independent from the magnetic ordering. However, in type-II multiferroics, the inversion symmetry breaking magnetic structure itself will govern the ferroelectric behavior, and two macroscopic origins have been identified that give rise to this magnetically driven ferroelectric order.

2.4.1 Ferroelectricity in spiral magnets due to spin-orbit interaction and geometric frustration

Spin-orbit interaction driven ferroelectricity can be observed commonly in materials with non-collinear spin structures such as the perovskites $RMnO_3$ and RMn_2O_5 (R=Tb, Ho, Dy), Kagome staircase compound $Ni_3V_2O_8$ [5, 6, 20, 21], and $MnWO_4$ [31, 32]. In a recent theoretical study in perovskite $RMnO_3$ (R=Gd, Tb, Dy) The mechanism that gives rise to the ferroelectric order and the strong coupling between the ferroelectricity and incommensurate magnetic order has been described as an inverse Dzyaloshinski-Moriya effect [33].

Geometric frustration is seen in systems that have geometries that do not allow the simultaneous minimization of internal energy and maximization of entropy. Even a simple 2-dimentional triangular lattice, shown in figure 2.6 (a) leads to frustration. Consider Ising spins (which are discussed in section 2.5) that are antiferromagnetically coupled. Each spin would have to align anti-parallel to each other to minimize energy and maximize entropy. If one spin points up and one spin down with antiferromagnetic interactions, the third spin cannot minimize its energy whether pointing up or down, because both these orientations would give the same energy. Hence the ground state of the system becomes degenerate. A famous example of a geometrically frustrated lattice is a Kagome lattice made up of corner sharing triangles and hexagons. To settle in a minimum energy configuration, geometrically frustrated spins may develop non-collinear spin structures (which are also discussed in section 2.5), which often lead to coexisting ferroelectric order and ferromagnetic order.

(a)   (b)
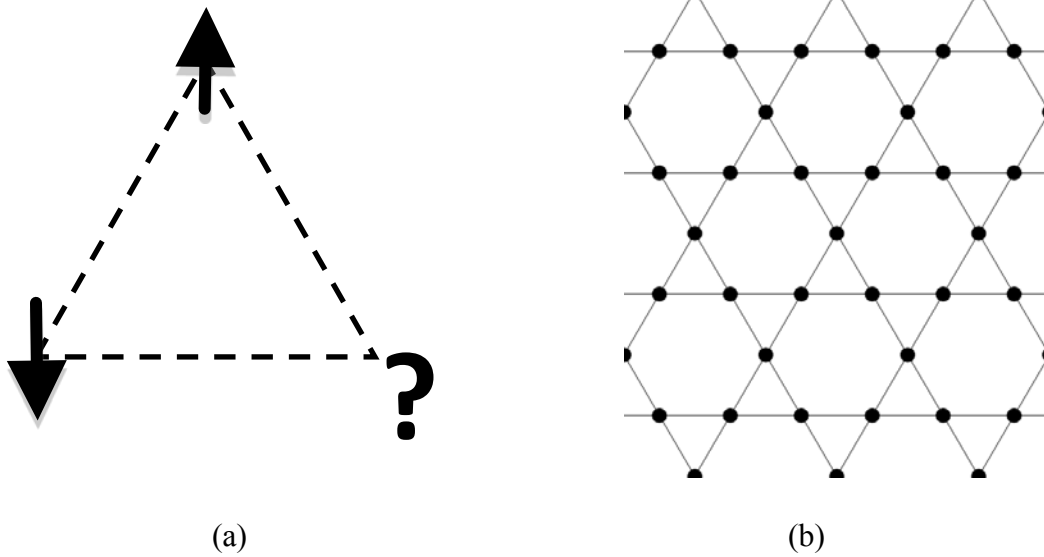
Figure 2.6: (a) Antiferromagnetically interacting spins in a triangular arrangement (b) a Kagome lattice which is inherently highly frustrated

Frustrated magnetic systems have been studied as early as 1950 [34], where a study of the Ising model on a triangular lattice with nearest-neighbor spins coupled antiferromagnetically was undertaken. However, recent years have seen a surge in research on geometrically frustrated multiferroic materials with the discovery of Kagome staircase materials like $Ni_3V_2O_8$, as they often have a strong coupling between the ferroic orders.

2.4.2 Ferroelectricity due to magnetorestriction

Collinear magnetic structures which have inequivalent magnetic ions with different charges can show ferroelectric ordering due to magnetorestriction. The mechanism is explained in figure 2.7, taken from [29]. Here, if the magnetic structure alone is considered, it is centrosymmetric and does not break the inversion symmetry. Similarly, if the charge structure

alone is also symmetric, but however has a different inversion center. So when both spin and charge structures are considered together, the system loses inversion symmetry and a ferroelectric polarization is developed in the direction shown by the red arrow in 2.7 (B). This type of ferroelectric behavior is observed in the system Ca_3CoMnO_6 which has an up-up-down-down magnetic structure, where Co^{2+} and Mn^{4+} ions alternate along the chain [35].
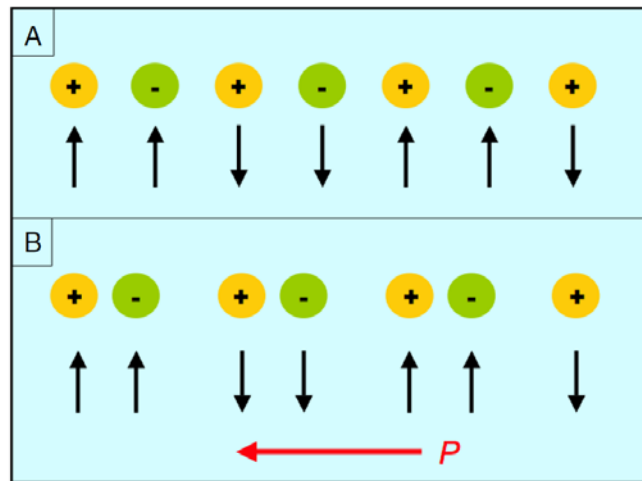
Figure 2.7: Mechanism of magnetorestrictive ferroelectricity (A) A spin up-up-down-down chain which has alternating positive and negative charges (B) magnetorestriction can shorten the ferromagnetic bonds creating a polarization [29].

2.5 Spin Models

It is necessary to use models to explore complex magnetic structures to understand the interactions between the spins and how they may produce ferroelectric or magnetic ordering. Two of the most commonly used models are Ising spin model and Heisenberg spin model.

2.5.1 Ising spin model

Ising model is widely used because it is simple, yet it has the ability to represent rich and complex systems and because it can be solved analytically in 2-D. The Ising model treats the system as a discrete collection of spins which are pointing either up or down, and subject to nearest neighbor interactions in the simplest case. This treatment is especially useful for representing diluted magnetic materials, since replacing some of these spins (magnetic ions) with spin-0 ions (non-magnetic ions) is equivalent to removing some of the spins from the lattice (figure 2.8(b)). This connection is described in more detail in chapter 5.

(a)   (b)
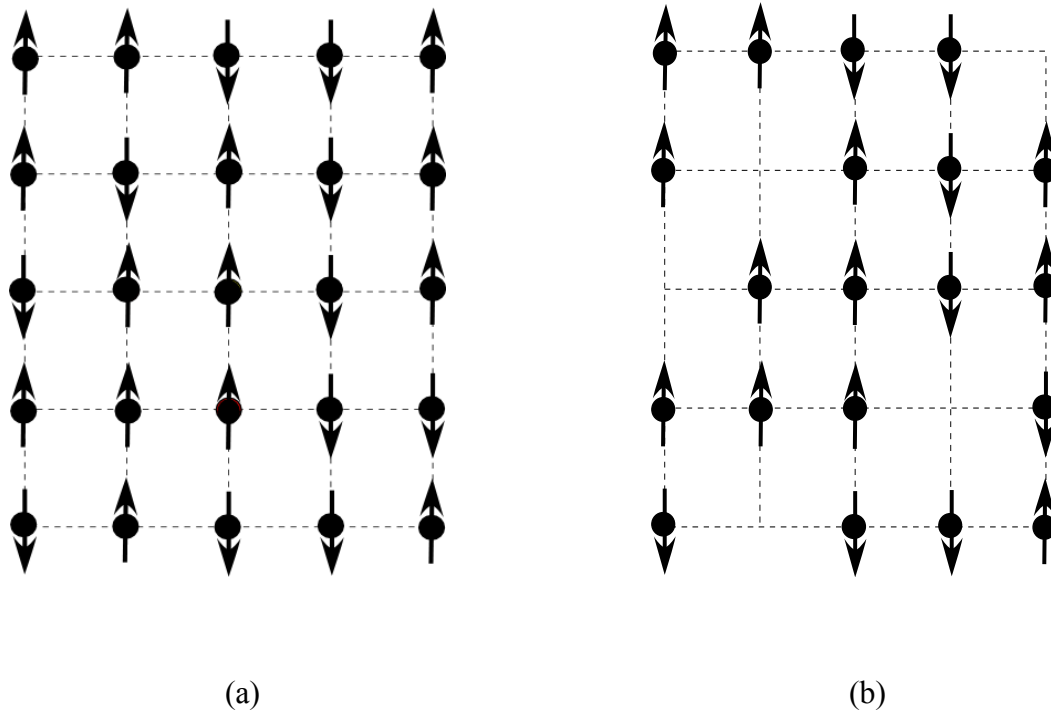
Figure 2.8: (a) Ising spins (b) Ising spins with some of the spins removed, reminiscent of simple site dilution

The Hamiltonian for Ising spins can be written as

$$H = J_1 \sum_i S_i^z S_{i+1}^z + J_2 \sum_i S_i^z S_{i+2}^z + \cdots \tag{2.6}$$

Where the first term represents the nearest neighbor interaction and the second term represents the next-nearest neighbor interactions and so on.

2.5.2 Heisenberg spin model

The Heisenberg spin model treats the spins of a magnetic system 3-dimentionally and as a quantum mechanical operators rather than pointing simply up or down as in Ising model for which the spin vector operator is only one dimensional. Heisenberg model is based on the exchange interaction between neighboring magnetic dipoles on different lattice sites which leads to long range ferromagnetic order. The commonly used nearest-neighbor Heisenberg model has the Hamiltonian given in equation 2.7, where S_i and S_j are 3 dimensional vectors unlike in the case of Ising model.

$$H = \sum_{<ij>} J_{i,j} \boldsymbol{S}_i \cdot \boldsymbol{S}_j \tag{2.7}$$

Where $J_{i,j} = J$ for nearest neighbors and $=0$ if else.

Two further parameters can be defined, dimensionality d of the lattice itself, and the dimensionality of the order parameter D, which is in general the same as the dimensionality of the spins [9]. In the case of a one dimensional Ising model, both d and D will be equal to 1 where long range ordering is unlikely above T=0 due to large entropy gains when a defect is introduced into a long chain. However, two-dimensional Ising models ($D=1$, $d=2$) are possible at a non-zero

critical temperature. The 2-dimensional Ising model was solved statistically after an extremely rigorous calculation by Lars Onsager in 1944 [36].

In summary, magnetism is purely a quantum mechanism phenomenon arising from exchange interaction. Various types of magnetic ordering exist, including simple ferromagnetic, antiferromagnetic and ferrimagnetic ordering, and non-collinear ordering such as helical, cycloidal and spin spirals. In type-I multiferroics, ferroelectric ordering occurs due to lone pairs or charge ordering, or can occur in the form of geometric ferroelectricity. In type-II multiferroics, the sources of ferroelectric ordering are spin-orbit interaction, geometric frustration and magnetorestriction.

CHAPTER 3

REVIEW OF PREVIOUS WORK

Although ferroelectricity and ferromagnetism coexist rarely due to reasons discussed in the previous chapter, a fair number of multiferroics have been identified and studied over the years. Landau and Lifshitz postulated the existence of multiferroics in 1959 [37], however, the interest in multiferroics has been fairly low for a few decades until Ramesh, *et. al.* [18] synthesized multiferroic $BiFeO_3$ thin films in 2003. Since then, a number of multiferroics have been identified, with the most common being the perovskite transition metal oxides. These include the rare earth magnetites $RMnO_3$ for R = Dy, Tb, Gd and RMn_2O_5 for R = Dy, Tb, Ho, as well as ferrites such as $BiFeO_3$, the only known room temperature multiferroic. Vanadates which wall into type-II multiferroics such as $Ni_3V_2O_8$ and $FeVO_4$ have also attracted a lot of attention due to their strong magnetoelectric coupling.

3.1 $Ni_3V_2O_8$

$Ni_3V_2O_8$ is a type-II multiferroic material where the magnetic ordering drives the ferroelectric order [5, 6]. It is a geometrically frustrated material having an orthorhombic unit cell, belonging to the material group with common formula $M_3V_2O_8$ (M=Zn, Cu, Ni, Co). The only magnetic ions present, the spin-1 Ni^{2+} ions form a highly frustrated layered buckled Kagome lattice. Because of this spin frustration, $Ni_3V_2O_8$ has a rich magnetic structure with a set of complex phase transitions taking place at low temperatures, out of which one phase is multiferroic. $Ni_3V_2O_8$ has attracted considerable attention in the recent years because of this

behavior [5, 6, 20, 21]. Although it is not feasible to exploit $Ni_3V_2O_8$ for fabricating magnetoelectronic devices as the multiferroic behavior develops only at very low temperatures, it provides a very useful platform for studying the nature of complex magnetic phase transitions as well as probing the spin structure in geometrically frustrated materials.
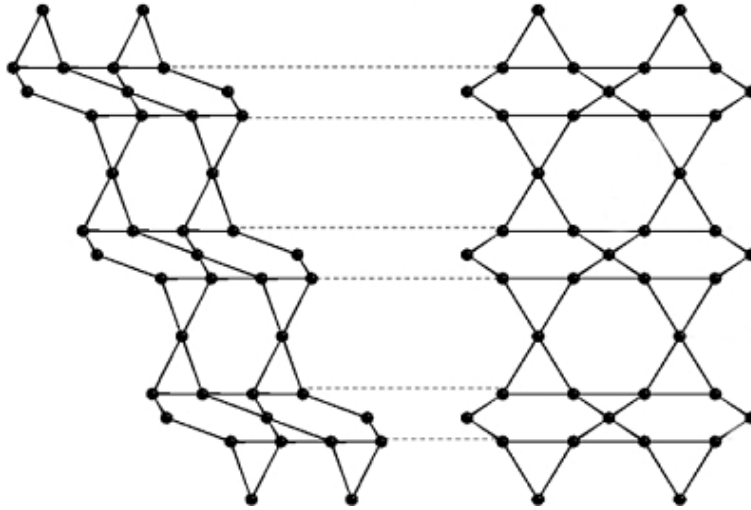
Figure 3.1: Ni sub-lattice found in $Ni_3V_2O_8$ [5]

Figure 3.1 shows the schematic representation of Ni atoms in the $Ni_3V_2O_8$ lattice [5]. The magnetic Ni^{2+} ion layers have the coordination and 2 dimensionality of a Kagome lattice but they are buckled, forming a Kagome staircase geometry with the Kagome planes perpendicular to the crystallographic b-axis. Because of layered nature of the Kagome staircase, the Ni^{2+} can be approximated by a 2-dimensional Kagome lattice, which will be discussed further in chapter 5. $Ni_3V_2O_8$ phase transitions have been comprehensively studied. [5, 6, 20, 21]. The phase diagram of $Ni_3V_2O_8$ is shown in figure 3.2 for the magnetic field applied along the 3 crystallographic axes, plotted as a function of temperature vs. applied field. $Ni_3V_2O_8$ is paramagnetic (PM) at room temperature. It undergoes a phase transition to a so called High Temperature

Incommensurate (HTI) phase at T=9.2 K followed by an inversion symmetry breaking transition to a Low Temperature Incommensurate (LTI) phase at T=6.3 K, both of which are second order phase transitions. It has been well established that this LTI phase shows magnetically driven ferroelectric ordering. Cooling down further, the system undergoes a first order phase transition to a Canted Antiferromagnetic phase (CAF) at T=3.9K. Finally, $Ni_3V_2O_8$ undergoes a second order phase transition to a C' phase which is believed to be a purely commensurate antiferromagnetic phase [38] at T=2.1 K. Recently there have been some evidence of another magnetically induced incommensurate phase below 2 K [38, 39], however this is still under investigation.
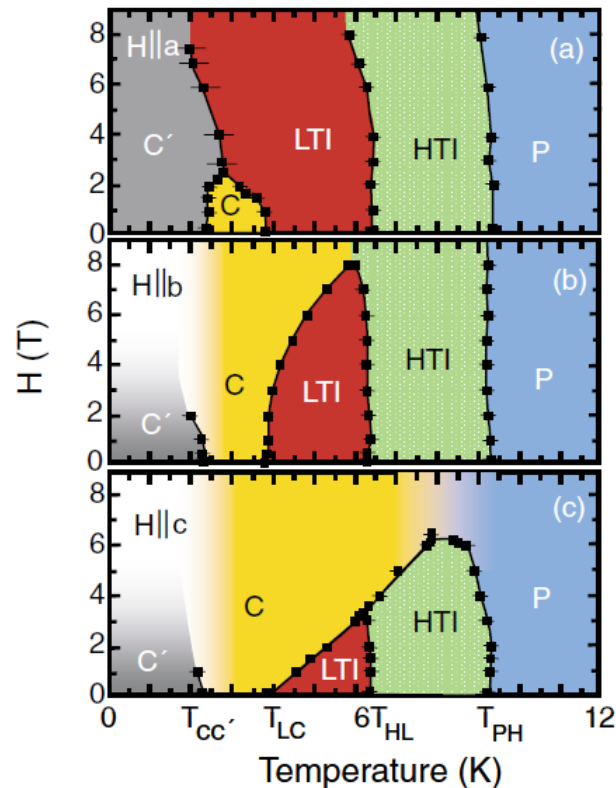
Figure 3.2: $Ni_3V_2O_8$ phase diagram along different crystallographic axes [6]

These different phases have unique magnetic ordering. Figure 3.3 taken from [20], shows there are two different kinds of Ni^{2+} spin types in the lattice which are usually referred to as *spine* and *cross tie* spins. The complex phase diagram, as well as the different magnetic structures for each phase is a result of the magnetic anisotropy and the competition between several weak magnetic interactions.
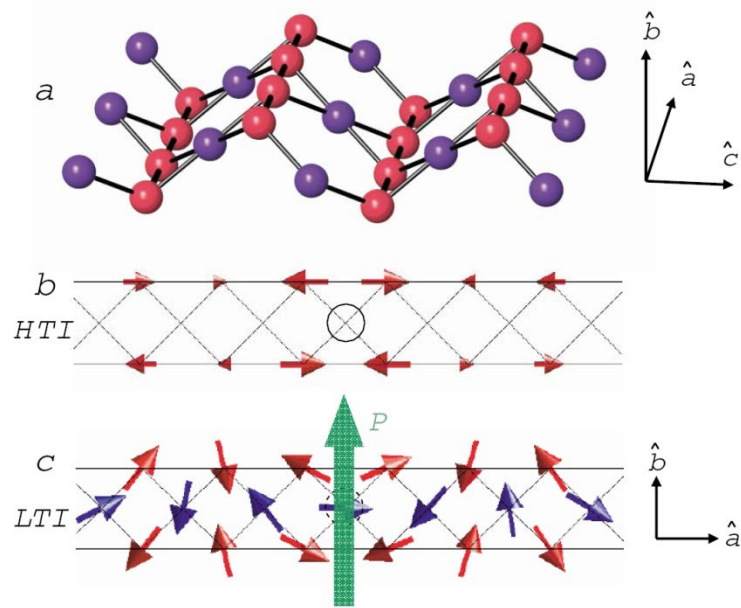
Figure 3.3: $Ni_3V_2O_8$ magnetic structure (a) Crystal structure showing spin-1 Ni^{2+} spine sites in red and cross tie sites in blue. (b), (c) Simplified schematic representation of spin arrangement in the antiferromagnetic HTI and LTI phases [20]

In each of these ordered magnetic phases, the symmetry of the magnetic lattice plays a key role in understanding the magnetic properties of $Ni_3V_2O_8$. On the HTI phase, as seen in figure 3.3 (b), the spine Ni^{2+} sites contribute mostly to the magnetic ordering, where they point

along the crystallographic b axis to produce an Ising like antiferromagnetic structure. Here the isotropic nearest neighbor interactions between the cross tie sites produce zero mean field. This phase has inversion symmetry and as a result no ferroelectric polarization is possible. In the LTI phase however, both spine and cross tie spins contribute to the magnetic structure where they rotate on the *a-b* plane. The competing Nearest Neighbor, Next Nearest Neighbor, and Dzyaloshinski-Moriya interactions in this phase leads to an incommensurate state that breaks spatial inversion symmetry and produce magnetically driven ferroelectric order [40]. Neutron studies have confirmed that the HTI phase has predominantly Ising spin behavior and LTI phase shows Heisenberg spin behavior. The LTI phase of $Ni_3V_2O_8$ is multiferroic. Thus, $Ni_3V_2O_8$ also provides a platform to study how this multiferroic order may change when the spin structure is modified. Studies have been done on the effect of Zn and Co doping on $Ni_3V_2O_8$ that show how the multiferroic ordering is affected when doped, and will be discussed in more detail in section 3.3.

3.2 FeVO$_4$

FeVO$_4$ is a recently discovered type-II multiferroic which has a triclinic structure and belongs to the $\overline{P1}$ space group [7]. It undergoes two antiferromagnetic transitions at low temperatures. It has a Neel temperature T_{N1} of 21 K where it forms a collinear incommensurate structure, and at T_{N2} ~15 K it undergoes a second antiferromagnetic transition to a non-collinear incommensurate structure [7, 8, 41]. The T_{N2} ~15 K transition has been recently shown to be ferroelectric [7,8].
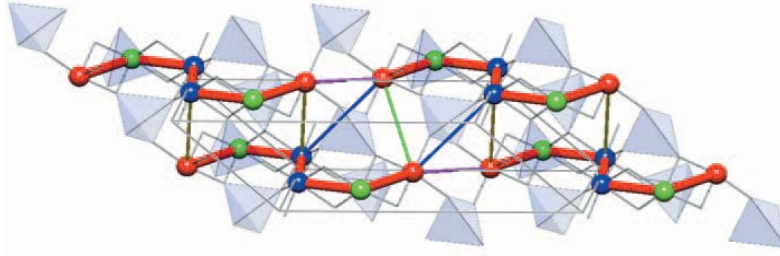
Figure 3.4: Crystal structure of $FeVO_4$. The three inequivalent Fe^{3+} ions are shown in red, green and blue while Fe-O bonds are shown in grey lines, and VO_4 tetrahedra in gray [7]

Unlike $Ni_3V_2O_8$ which has a high symmetry magnetic structure, $FeVO_4$ is a low symmetry crystal, with three different unique Fe^{3+} sites in the magnetic lattice. Figure 3.4, taken from [7] shows these three Fe^{3+} sites, where the intra-cluster interaction is shown in thick red lines. The thin lines between the different Fe sites indicate the Fe-Fe interactions which have contributions from direct exchange between Fe-Fe and superexchange between Fe-O-Fe.

Specific heat capacity measurements and magnetization measurements on single crystals (shown in figure 3.5 (a) and (b)) have clearly identified the two anomalies associated with these two magnetic phase transitions [7]. Dielectric measurements on polycrystalline $FeVO_4$ samples show a clear dielectric anomaly associated with the development of ferroelectric order at $T_{N2} =$ 15.4 K. The ferroelectric polarization measured by integrating the pyrocurrent is 6 $\mu C\ m^{-2}$, which is much smaller than that observed for $Ni_3V_2O_8$ (150 $\mu C\ m^{-2}$), but is consistent with many other magnetically driven ferroelectric materials.
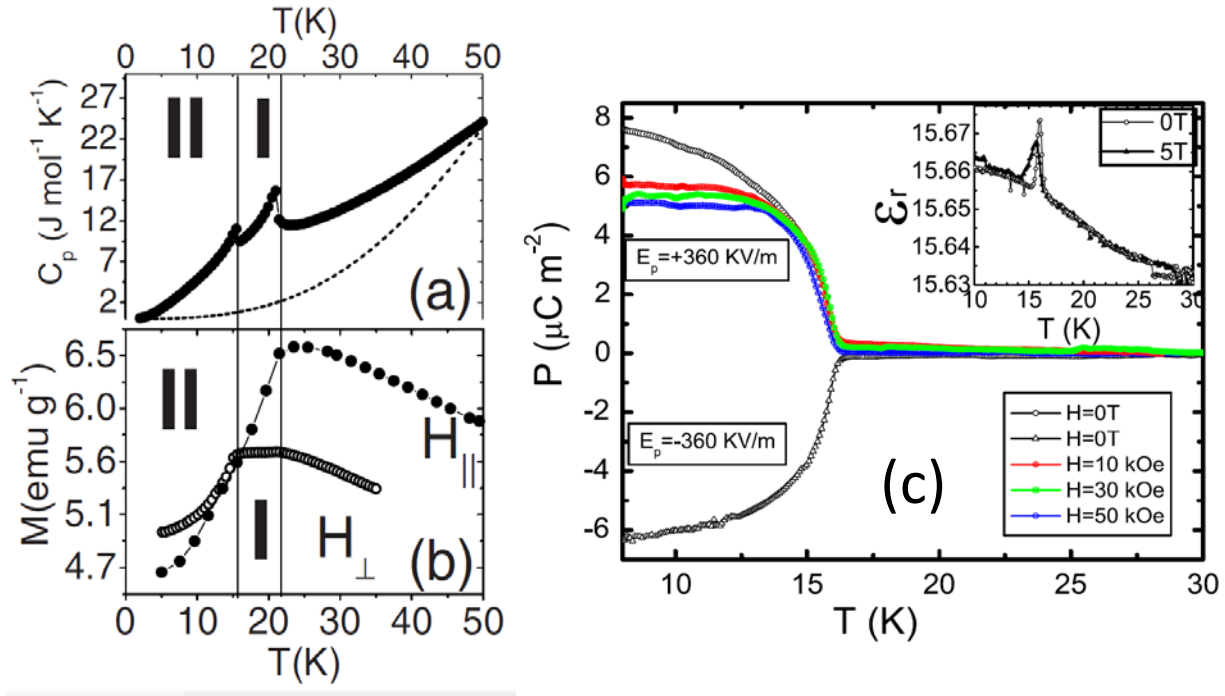
Figure 3.5: (a) Specific heat [7] (b) magnetization [7] (c) ferroelectric polarization with relative dielectric constant (inside panel) [8] measurements of $FeVO_4$

Because of the low symmetry in $FeVO_4$, the direction of the polarization is not determined simply from the magnetic structure, but also depends on details of the microscopic magnetoelectric interaction [22]. Since most of the other known multiferroics are high symmetry structures, $FeVO_4$ provides a great platform to study magnetoelectric interactions in a complex multiferroic, because information on these interactions can be more readily available.

3.3 Doping studies on multiferroics

Doping can be used as a very useful tool to perturb the magnetic structure and obtain information about how the magnetic lattice parameters are affected when doped with small amounts [42, 43, 44]. As an example, the multiferroic $RMnO_3$ systems have an orthorhombically

distorted perovskite structure where the ferroelectric order is driven by the magnetic interactions. Substitution at the R site can induce distortions in the lattice, changing the M-O-M bond angle and hence the magnetic exchange interaction, which finally changes the magnetic and ferroelectric properties [45]

Doping can also be used to study how the multiferroic ordering temperature changes and microscopic magnetic interactions which give rise to the multiferroic behavior are affected under perturbations, providing evidence on how stable the magnetic interactions are against perturbing the magnetic lattice with different spins [44, 46]. $BiFeO_3$, a room temperature multiferroic having ferroelectric and magnetic transitions at ~1100 K and ~640 K respectively, has also been investigated in great detail by doping especially rare earth metals into the lattice to increase the magnetoelectric coupling [47, 48]. Doping studies done on $MnWO_4$, where magnetic Mn^{2+} ions were substituted by nonmagnetic Zn and Mg, have shown that the phase transition temperatures were suppressed linearly with doping fraction [49]. Another recent study finds that the multiferroic phase of $MnWO_4$ is also remarkably stable against such doping by non-magnetic ion, which persists up to a 50% Zn fraction [50]. However, magnetic dopants have found to have a more drastic effect on the multiferroic ordering on $MnWO_4$. A recent study on doping $MnWO_4$ with magnetic Fe find a strong suppression of the multiferroic phase, which completely vanishes at an Fe fraction of x=0.05 [51]. Doping with Co however, seems to have a smaller effect on the multiferroic phase transition than doping with Fe. A study done on $Mn_{0.85}Co_{0.15}WO_4$ single crystals finds the material is still clearly ferroelectric even at 15% Co doping. [52]. However, the magnitude which magnetic dopants affect the multiferroic order is in direct contrast to doping $MnWO_4$ with non-magnetic Zn, where the multiferroic phase persists to doping fractions of x=0.50 [50].

Some recent studies have concentrated on how the $M_3V_2O_8$ structures (especially for M=Ni and Co) behave when doped with Co/Ni. $Co_3V_2O_8$ bears identical crystal symmetry and similar structural parameters to $Ni_3V_2O_8$, but behaves quite different magnetically. Co^{2+} ions also arrange in a Kagome staircase with two inequivalent spine and cross tie sites, similar to $Ni_3V_2O_8$. At $T_N = 11.4$ K, Co^{2+} spine site spins arrange mostly along the crystallographic a axis leading to an antiferromagnetic order similar to the HTI phase of $Ni_3V_2O_8$. Then however, $Co_3V_2O_8$ displays a commensurate AFM phase at 8.6 K, incommensurate phase at 6.8 K and an AFM phase at 6.5 K, before finally going into a ferromagnetic phase below 6.2 K [53]. $Cu_3V_2O_8$ on the other hand, has been studied rarely [54] where a single magnetic transition was observed at $T_N = 29$ K. Studies on $(Co_xNi_{1-x})_3V_2O_8$ ceramics using magnetization and neutron diffraction measurements found evidence that the $Co_3V_2O_8$ magnetic structure is maintained only for x>0.98, while the HTI $Ni_3V_2O_8$ magnetic structure is realized for x<0.71 [55]. Furthermore, they find a minimum Neel temperature of $T_N = 5.5$ K at x~0.76 [56]. Measurements on single crystal samples also suggest a cross-over between $Ni_3V_2O_8$ and $Co_3V_2O_8$ antiferromagnetic structures near x~0.8 [57].

A recent report on Zn, Co, and Mn doped $Ni_3V_2O_8$ finds that the ferroelectric order becomes more stable when doped with a small amount of Co or Mn, and that the system undergoes a single magnetic phase transition when doped with larger Co fractions (x=0.36) [55]. Finally, investigations on doping $Ni_3V_2O_8$ with magnetic Co^{2+} and non-magnetic Mg^{2+} ions indicate that changes in the magnetocrystalline field induced by chemical disorder may significantly affect the magnetic properties of the system [58].

In this work, we first explore the response of magnetic ordering in $Ni_3V_2O_8$ to simple non-magnetic Zn doping, followed by more complex magnetic (Cu, Co, Fe and Mn) doping. We also present both magnetic and non-magnetic doping studies on $FeVO_4$ for the first time, and present phase diagrams for all the dopants we introduced in to the lattice for these two materials.

CHAPTER 4

SYNTHESIS AND CHARACTERIZATION TECHNIQUES

4.1 Introduction to characterization techniques

Following the synthesis, a sample has to undergo both structural and chemical characterization techniques to check whether the correct phase is attained, as well as to confirm the stoichiometry, especially on doping studies. Structural characterization is often carried out using x-ray diffraction as well as Raman spectroscopy, while the chemical composition is confirmed via energy dispersive spectroscopy.

4.1.1 X-ray diffraction (XRD)

X-ray diffraction is a technique based on using the scattered intensity of an x-ray beam off a sample in order to gain information about its crystal structure. It is widely used for studying the crystal structure of a material, including identifying the structure of an unknown material, measuring the spacings between the atomic planes, to determine the orientation of single crystals as well as to determine the crystalline sizes in a polycrystalline material. X-rays were discovered by Rontgen in 1895, however it was not until 1912 that Laue proposed using crystals as a diffraction grating for x-rays in order to obtain a characteristic diffraction pattern from a crystal [59]. Bragg's law, given in equation 4.1 defines the constructive interference off successive crystallographic planes that is necessary to give a measurable signal when an x-ray is scattered off a lattice plain.

$$2d\sin\theta = n\lambda \qquad\qquad (4.1)$$

If θ is the scattering angle, the path difference between the two adjacent x-rays will be $2d\sin\theta$, which has to be equivalent to an integer multiplier of the wavelength of the x-ray for constructive interference to occur.
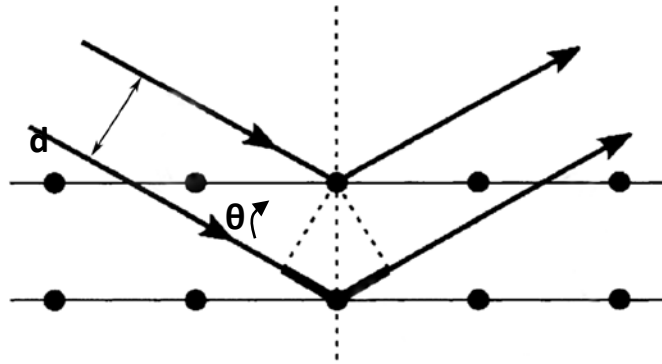
Figure 4.1: Bragg scattering off crystal planes

When x-ray diffraction is used on a polycrystalline powder sample (which consists of randomly oriented crystalline domains) a concentric rings of scattering peaks, which corresponds to the various spacings (d) in the crystal lattice can be observed. A widely used technique is to keep the x-ray tube stationary while rotating the sample θ and the detector by 2θ. Then the angle of diffraction (2θ) is related to the inter-planar spacings, and the diffraction maxima (in terms of observable peaks) will correspond to the abundance of the relevant spacings in the lattice. The user is then able to match these observed peak positions with the existing XRD peak database to identify the peaks and hence the material.

As it is possible to take XRD measurements in a few minutes on a very small area non-destructively, a very small amount of material is sufficient for this technique. However, X-ray

diffraction has the distinct disadvantage of being unsuitable on non-crystalline materials as they provide no Bragg scattering.

4.1.2 Raman Spectroscopy

Raman scattering is a weak inelastic scattering process, which was discovered by Sir Chandrasekhara Venkata Raman in 1928 [60]. Raman spectroscopy is a powerful and sensitive technique that can provide information of molecular or crystalline structures/symmetries and different phases of a material. Unlike XRD, Raman spectroscopy can provide information on the amorphous phases as well, and is much more sensitive than XRD.

When a photon is incident on a molecule or an atom it can excite or de-excite vibrational modes, resulting in scattered photons with decreased or increased energy by the amount of the vibrational transition energies [61]. Raman scattering can be Stokes scattering or anti-Stokes scattering depending on this energy gain or loss by the molecule. Thus, Raman shift is the energy difference between the incident photon and the scattered photon. Rayleigh scattering is an elastic process in which the scattered photon has the same energy as the incident photon [62].
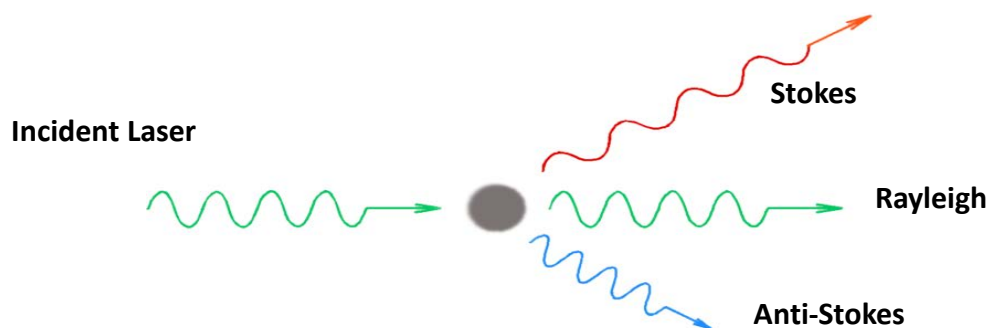
Figure 4.2: A schematic illustration of Raman scattering

For a vibrational mode to be Raman active the polarizability must change during a particular vibration. For a linear molecule with N atoms, there are 3N-5 possible vibrations and for a non-linear molecule 3N-6 possible vibrations can be observed. The vibrational transitions appear in the 10^2 to 10^4 cm^{-1} region in the Raman spectrum [61], however the 10^2 - 10^3 cm^{-1} region contains the more valuable information on the solid state chemical samples.

Quantum mechanically, vibrational energy levels of a molecule can be determined by solving the Schrödinger equation for a molecule. In a molecule, the chemical bond between the atoms can be considered as a spring (with spring constant K) and the motion of the atoms then can be described by Hooke's law. In treating diatomic molecule as a single particle with reduced mass μ, the Schrödinger equation for such a quantum mechanical system (a simple harmonic oscillator) can be written as,

$$\frac{d^2\psi}{dq^2} + \frac{8\pi^2\mu}{h^2}\left(E - \frac{1}{2}Kq^2\right)\psi = 0 \qquad (4.2)$$

Equation 4.2 can be solved for the energy eigenvalues or frequencies of the system, which are given by $E_\upsilon = h\nu\left(\upsilon + \frac{1}{2}\right)$ and $\nu = \frac{1}{2\pi}\sqrt{K/\mu}$. Here υ is called the vibrational quantum number. For a quantum mechanical simple harmonic oscillator, the allowed transitions are $\Delta\upsilon = \pm 1$, whereas for anharmonic systems $\Delta\upsilon = \pm 2, \pm 3,...$ can be observed which are commonly known as overtones.

Raman spectroscopy is particularly useful for doping studies. Because of its high sensitivity to the chemical composition of the sample, Raman can detect extremely small

amounts of possible impurity phases in a sample. Moreover, if the mass of a dopant ion is different from the ion it is replacing, a visible shift in Raman modes may be observable since the vibrational modes corresponding to that chemical bond may change. This can be used to confirm dopants ions are correctly being incorporated in to the lattice, as discussed in chapter 7.

4.1.3 Energy Dispersive X-ray Spectroscopy (EDS)

Energy dispersive spectroscopy is an analytical technique often used in combination with a Scanning Electron Microscopy (SEM) system. A high energy beam of electrons is incident on a sample which will excite some of the ground state electrons into excited states. An electron from an outer shell with higher energy will eventually fill this vacancy, and an x-ray photon will be emitted which will have the energy difference between this higher state and the ground state. These emitted photons will be then captured by a detector where they will give rise to the characteristic x-ray lines which are unique to each element.

4.2 Synthesis and characterization of $Ni_3V_2O_8$ polycrystalline samples

We prepared polycrystalline $(Ni_{1-x}M_x)_3V_2O_8$ powder samples for M = Zn, Cu, Co, Fe and Mn. For M = Zn and Co, we used a standard solution based metal-organic synthesis technique as shown in figure 4.3 (a). We prepared samples in the composition range x = 0 to 0.3 for Zn, and the entire composition range x = 0 to 1 for Co doping. For M = Cu (x = 0 to 0.5), Fe (x = 0 to 0.2) and Mn (x = 0 to 0.2), we used a standard solid state reaction method as shown in figure 4.3 (b), because the liquid based metal-organic synthesis method was not optimal for obtaining the correct phase with these dopants.

To prepare undoped $Ni_3V_2O_8$, we used a mixture of nickel(II) 2-ethylhexanoate and vanadium napthanate oxide in 3:2 atomic ratio. To prepare the Zn doped samples, the appropriate amount of nickel(II) 2-ethylhexanoate was added to obtain the desired atomic composition, while for Co doping cobalt(II) 2-ethylhexanoate was used. These precursors were dissolved in xylene and then mixed in an ultrasonic bath for 30 minutes to increase the homogeneity of the solution. The mixture was then heated up to 450 ^{o}C for 1 hour to burn off the organic compounds. At this stage, the samples turn to a black powder, which were subsequently heated in air to 1000 ^{o}C for 2 hours. The resulting yellow colored flakes were air cooled to room temperature slowly, ground into a fine powder and cold pressed into pellets.
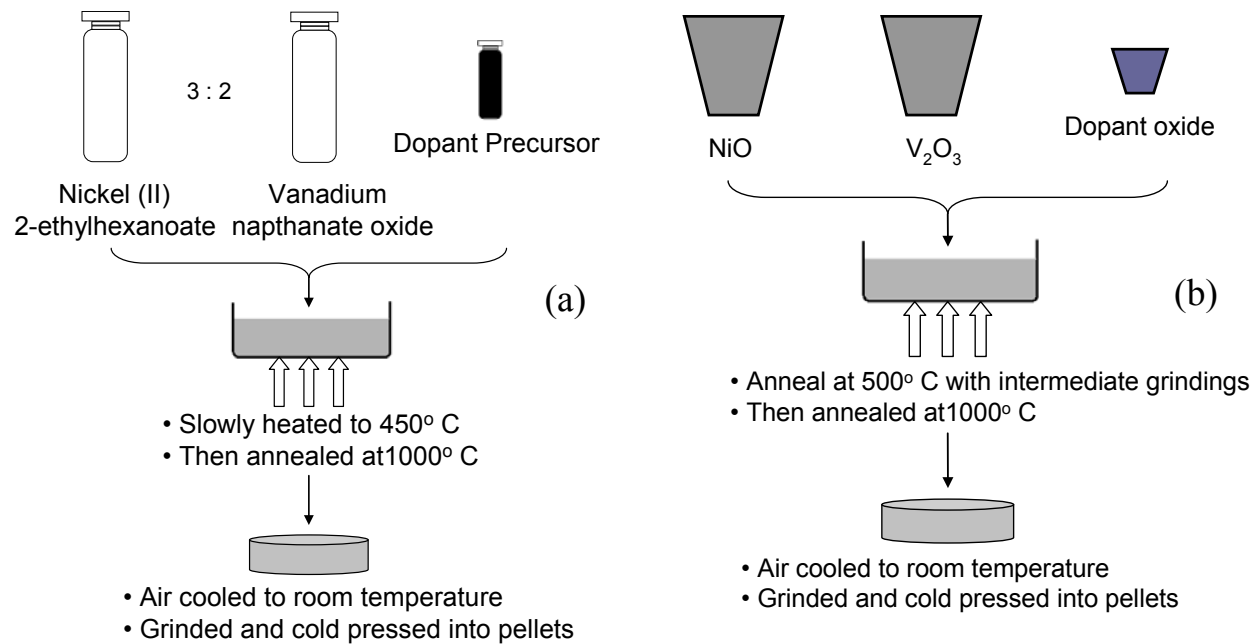
Figure 4.3: Schematic diagrams of (a) the metal-organic synthesis and (b) the solid state reaction method

To prepare the Cu, Fe and Mn doped samples, we used the powder based solid state reaction method shown in figure 4.3 (b). Starting from a mixture of NiO and V_2O_3, the relevant oxide was added to the correct atomic proportion and grinded well. This mixture was annealed at 500° C for 12 hours at a time with intermediate grindings to improve the homogeneity in the powder mixture, and was finally annealed at 1000° C for 2 hours. The resultant $(Ni_{1-x}M_x)_3V_2O_8$ powder was cooled down slowly to room temperature, ground into a fine powder and cold pressed into pellets. The Ni, V, Zn, Cu, Co, Fe and Mn concentrations for these samples were verified by Energy Dispersive x-ray Spectroscopy (EDS) on a Hitachi S-2400 scanning electron microscope equipped with an EDAX spectrometer and found to be in good agreement with the expected values.

We investigated the structure of these samples using X-ray diffraction (XRD) and Raman spectroscopy. Figure 4.4 (a) shows the XRD pattern obtained for pure $Ni_3V_2O_8$ (top panel) and 20% Zn doped $Ni_3V_2O_8$ (bottom panel). In both patterns, all the peaks observed are diffraction peaks expected for $Ni_3V_2O_8$ (PDF#74-1485), while no other additional peaks are observed. Other samples' (x=0.025, 0.048, 0.08, 0.1, 0.14, 0.24 and 0.28) XRD patterns remain identical to pure $Ni_3V_2O_8$ (not shown). Figure 4.4 (b) shows the diffraction patterns obtained for selected $(Ni_{1-x}Co_x)_3V_2O_8$ samples over the entire composition range. For the x=0.15 and x=0.35 samples, all the diffraction peaks expected for $Ni_3V_2O_8$ are observed (PDF#74-1485), while the x=0.8 sample has peaks corresponding to the $Co_3V_2O_8$ crystal structure (PDF#74-1487). The average crystallite size is 30 nm, calculated using the Debye-Scherrer expression. The average crystallite size and peak positions do not change significantly with x, although for x>0.5 the XRD patterns show the presence of $Co_3V_2O_8$ peaks. XRD spectra for $(Ni_{1-x}Cu_x)_3V_2O_8$, plotted in Fig. 4.4 (c), show similar results to those obtained for lower Co fractions, with no evidence for impurity

phases. XRD patterns obtained for $(Ni_{1-x}Fe_x)_3V_2O_8$ and $(Ni_{1-x}Mn_x)_3V_2O_8$ yield the same results with no indication of impurity phases (not shown).
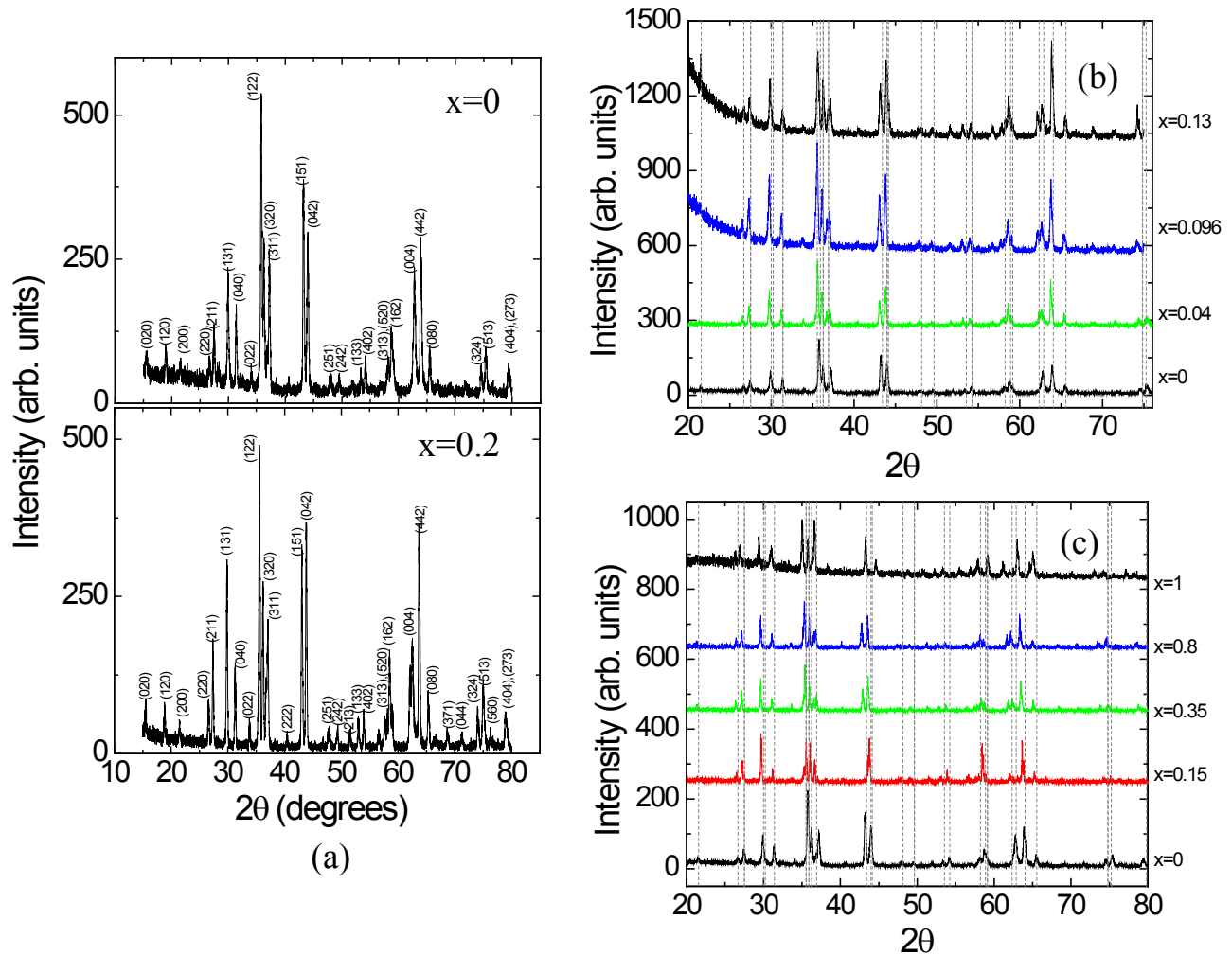
Figure 4.4: XRD patterns obtained from (a) pure and 20% Zn doped $Ni_3V_2O_8$ (b) Co doped $Ni_3V_2O_8$ (c) Cu doped $Ni_3V_2O_8$

We used Raman spectroscopy to confirm structure of the samples and as a sensitive test for the presence of impurity phases. Fig 4.5 (a) shows the Raman spectra obtained from the entire composition range of the Co doped samples. For clarity, only a select few spectra are

presented. Spectra up to x=0.5 are identical with the undoped $Ni_3V_2O_8$ spectrum, while x=0.8 spectrum is similar to $Co_3V_2O_8$ spectrum. This initial data suggests $Ni_3V_2O_8$ is robust against Co doping, while on the Co rich side, $Co_3V_2O_8$ is much more sensitive to Ni doping. This phenomenon is discussed at length later in chapter 5.
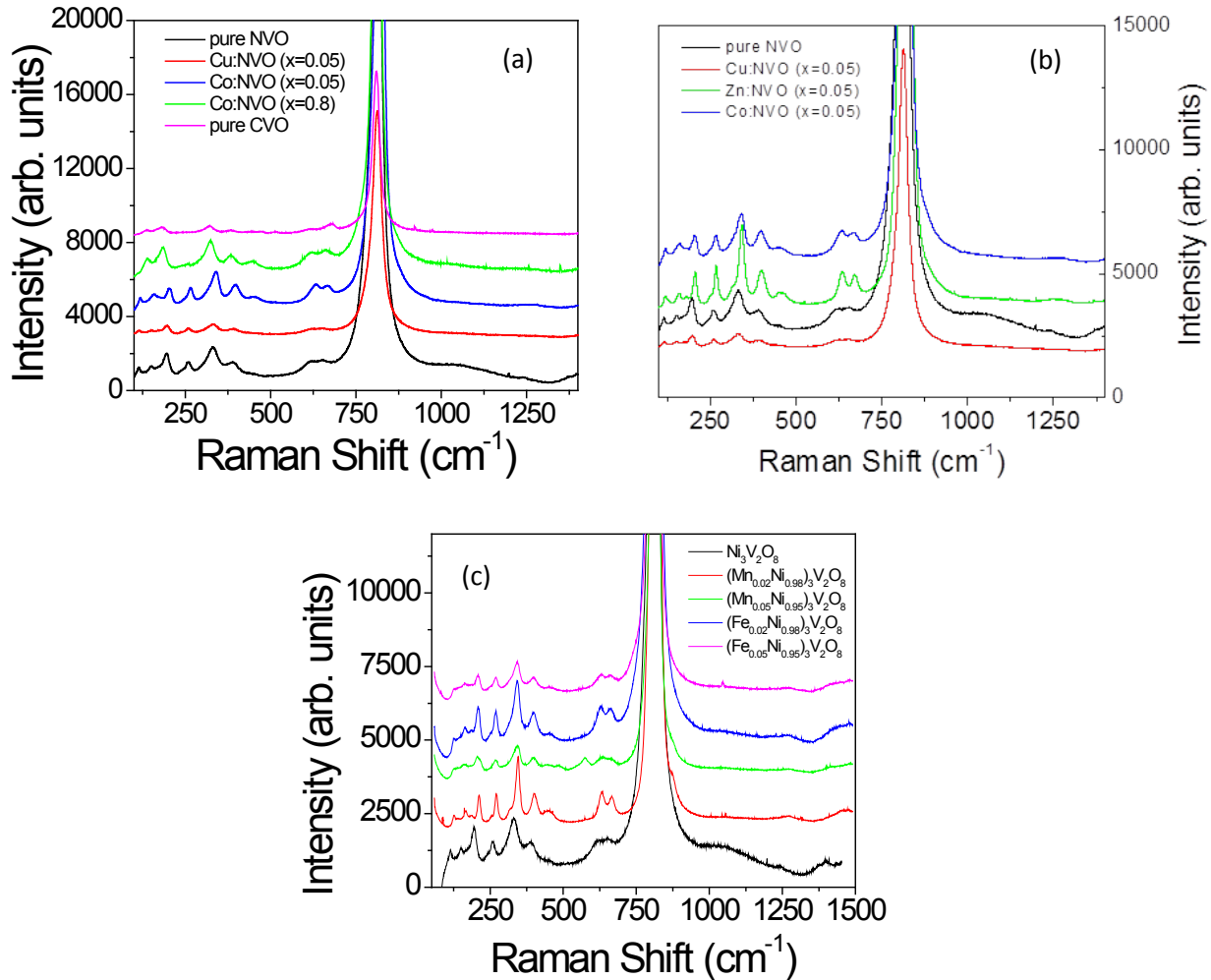
Figure 4.5: (a) Selected Co doped $Ni_3V_2O_8$ samples plotted together with pure $Co_3V_2O_8$ (b) Raman spectra of 5% Cu, Zn and Co doped samples together with undoped $Ni_3V_2O_8$ (c) Raman spectra of 2% and 5% Fe and Mn doped samples together with undoped $Ni_3V_2O_8$

Figure 4.5 (b) shows Raman spectra obtained for $(Ni_{1-x}M_x)_3V_2O_8$ for x = 0.05 for M = Zn, Co and Cu together with pure $Ni_3V_2O_8$, while figure 4.5 (c) shows Raman spectra obtained from a select few Fe and Mn doped samples. All the peaks for the three doped samples correspond to those observed for pure $Ni_3V_2O_8$. These studies suggest that the samples consist solely of transition metal substituted $Ni_3V_2O_8$, albeit with $Co_3V_2O_8$ developing at higher Co fractions, with no significant impurity phases present.

4.3 Synthesis and characterization of FeVO$_4$ polycrystalline samples

We prepared polycrystalline $Fe_{1-x}M_xVO_4$ samples over the composition range of x=0 to ~0.2 using a solid state reaction method similar to the method used for $Ni_3V_2O_8$ samples. Starting with a mixture of powder V_2O_5 and Fe_2O_3, the dopant oxide or nitride powder was added and mixed well. The mixture was then annealed at 550 ^{o}C for four hours, grinded well to improve homogeneity and finally annealed at 700 ^{o}C for an additional 4 hours. The resultant powder was then grinded and cold pressed into pellets as necessary for various measurements. The Zinc, Chromium and Manganese fractions were verified by energy dispersive x-ray spectroscopy (EDS) on a JEOL JSM 6510LV scanning electron microscope equipped with an EDAX spectrometer and found to be in good agreement with the expected values.
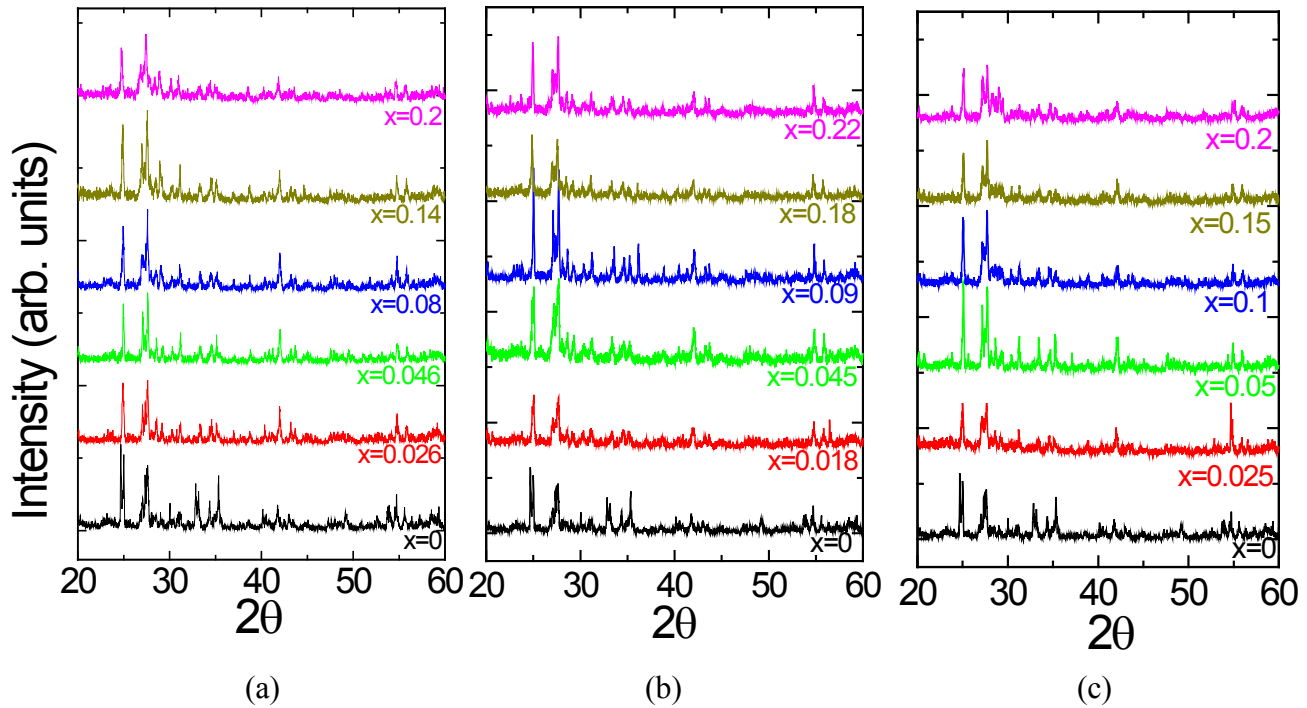
Figure 4.6: X-ray Diffraction patterns from $M_xFe_{1-x}VO_4$ for (a) M = Zn (b) M = Cr (c) M = Mn. All observed peaks match with the undoped $FeVO_4$ peak positions

To investigate the structure of these samples, we carried out X-Ray Diffraction (XRD) studies using a Rigaku RU2000 rotating anode diffractometer. Figures 4.6 (a), (b) and (c) shows the x-ray spectra obtained for $FeVO_4$ doped with Zn, Cr and Mn respectively, plotted together with undoped $FeVO_4$. The curves have been shifted in the vertical direction for clarity. We see all peaks observed in the undoped sample are from the expected $FeVO_4$ structure (PDF# 38-1372), while the same peaks are present in all doped samples and no additional unidentified peaks are present. This suggests samples annealed at 700 ^{o}C crystallized in the correct $FeVO_4$. We also carried out Raman spectroscopic studies, which are very sensitive to impurities in order

to look for small amounts of secondary phases as well as possible impurities in an amorphous phase.
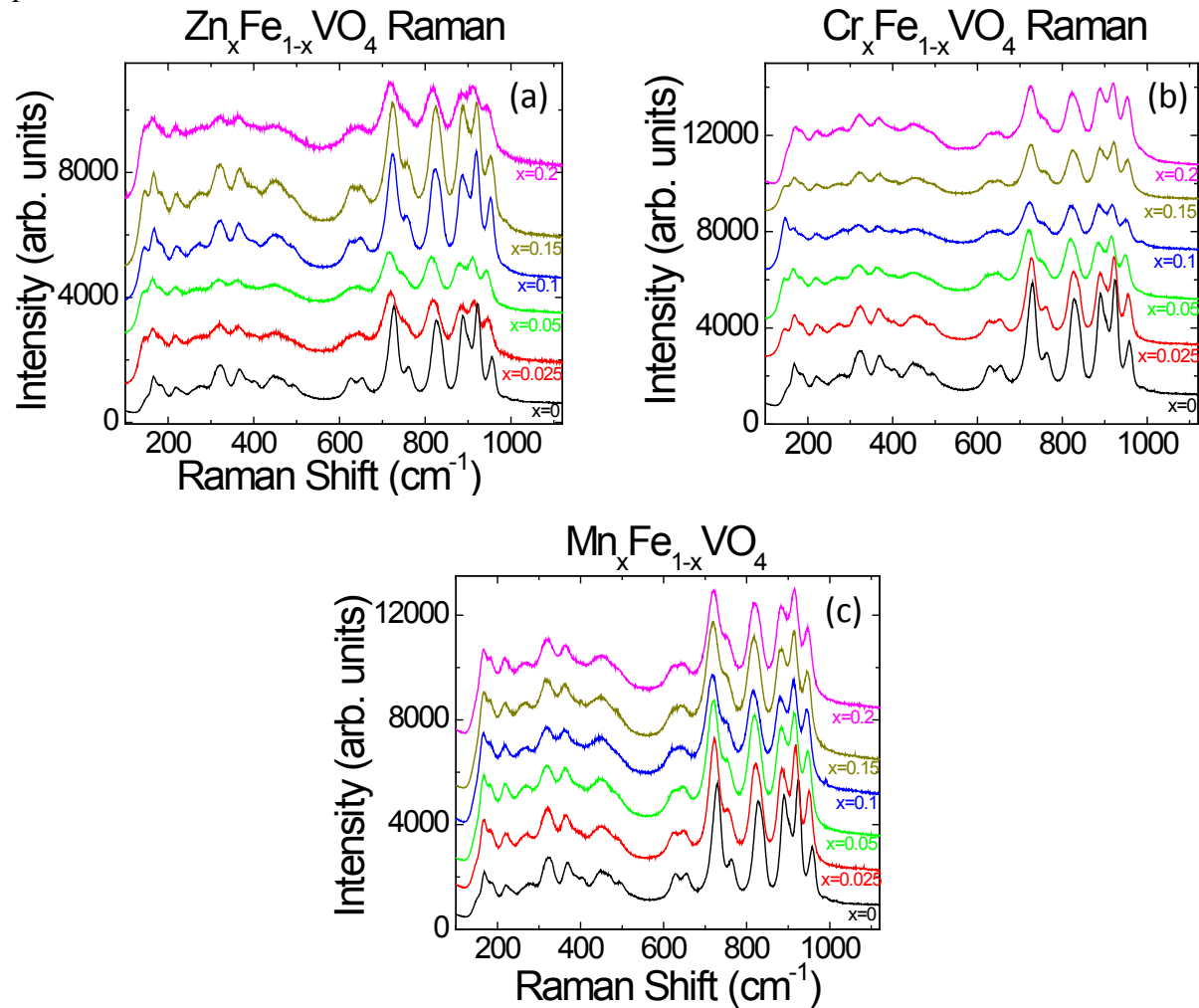
Figure 4.7: Raman spectra from $M_xFe_{1-x}VO_4$ for (a) M = Zn (b) M = Cr (c) M = Mn. All observed Raman modes for doped samples are the same Raman modes observed for undoped $FeVO_4$

Figures 4.7 (a), (b) and (c) shows the Raman spectra collected for $FeVO_4$ doped with Zn, Cr and Mn respectively. The curves have been shifted in the vertical direction for clarity. We observe 17 main Raman modes in undoped $FeVO_4$, which are all present in all the doped

samples' Raman spectra. The absence of any other unidentified peaks in these spectra suggests we have the correct $FeVO_4$ structure with no unidentified impurities. We also observe the Raman modes at 733, 842 and 928 cm^{-1} which are associated with Fe-O and V-O-Fe bonds [63] suppress to lower wave numbers with the increase of Zn doping fraction as indicated in figure 2 (a). This is consistent with the higher mass of Zn (65.4 amu) replacing some of the lighter Fe ions (55.8 amu) so that the vibrational frequencies of the bonds are reduced. On Cr (52 amu) and Mn (54.9 amu) Raman spectra, this effect is not significant as the mass difference between these and Fe is smaller. This indicates the dopant atoms are been incorporated into the Fe lattice effectively.

CHAPTER 5

NON-MAGNETIC DOPING OF Ni$_3$V$_2$O$_8$

After confirming the correct phase and doping fractions using XRD, Raman spectrometry and EDS, we started investigating the magnetic properties of Ni$_3$V$_2$O$_8$ by non-magnetic Zn doping. As discussed in section 2.4, doping with non-magnetic ions is similar to simple non-magnetic site dilution in the simplest case, and the expected behavior may be trivial below the percolation threshold for simple magnetic structures. However, in a complex magnetic lattice such as Ni$_3$V$_2$O$_8$ where the magnetic phase transitions as well as the ferroelectric order is driven by complex competing magnetic interactions which include not only nearest neighbor interactions, but also next nearest neighbor interactions as well as Dzyaloshinski-Moriya interactions, we can expect the behavior due to doping to potentially be more complex. Introducing even a small amount of dopant to the magnetic lattice may disrupt the sensitive balance between these competing magnetic interactions, therefore affecting one or more of these magnetic phases.

5.1 Undoped Ni$_3$V$_2$O$_8$

We started our measurements with undoped Ni$_3$V$_2$O$_8$ which we use as a baseline to compare with the doped samples. The most direct method to identify magnetic transition temperatures in a material is generally to look for features in the magnetic data, but unfortunately, Ni$_3$V$_2$O$_8$ does not show magnetic anomalies at all the transitions because the

magnetic susceptibility of $Ni_3V_2O_8$ does not change significantly at these transitions [6]. Therefore, we have used alternate measurements such as dielectric, heat capacity and pyrocurrent measurements to identify magnetic phase transitions in the undoped and doped $Ni_3V_2O_8$ samples. Figure 5.1 shows these different measurements taken from undoped $Ni_3V_2O_8$.
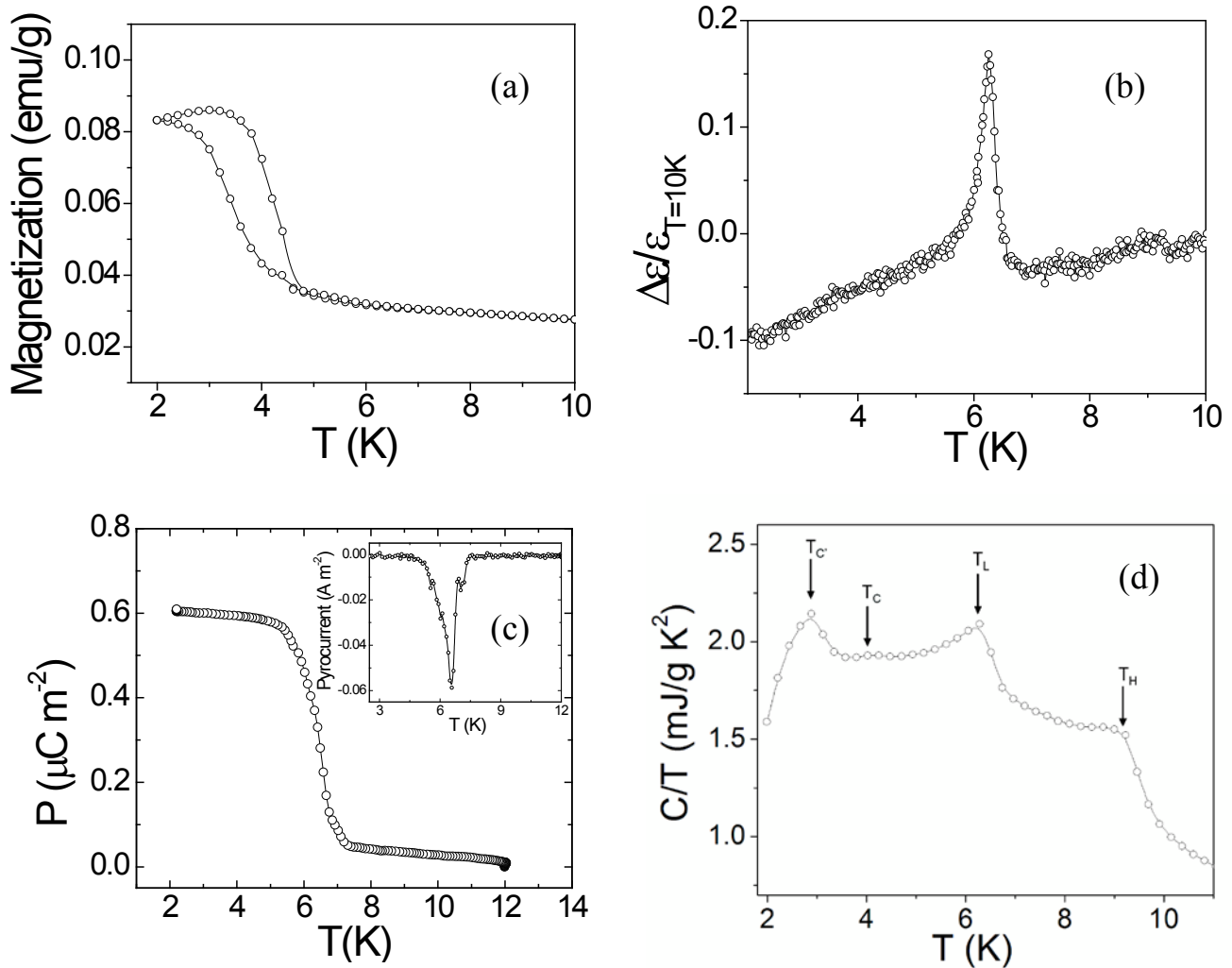
Figure 5.1: Undoped $Ni_3V_2O_8$ (a) Magnetization vs. temperature under H=100 Oe (b) Normalized dielectric constant measured under +1 V and 30 kHz, showing the dielectric

anomaly at T=6.3 K (c) Polarization under +200 V with pyrocurrent as the insert (d) Heat capacity showing all four transitions

We performed magnetic measurements on powder $Ni_3V_2O_8$ using a SQUID based Quantum Design Magnetic Property Measurement System (MPMS). Magnetization curve obtained under H=100 Oe is shown in figure 5.1 (a), and shows a broad feature around T=4 K, which is suggestive of the antiferromagnetic ordering it undergoes. This feature in fact corresponds to the LTI to CAF antiferromagnetisc transition which occurs at T=3.9 K. There is also a small hysteresis developing, which is consistent with previous reports on $Ni_3V_2O_8$ [5].

To measure the dielectric response, the top and bottom surface of the $Ni_3V_2O_8$ pellets were coated with silver epoxy, and wires were attached to form a parallel plate capacitor configuration. Data were taken using a Quantum Design Physical Property Measurement System (PPMS). Change of capacitance, defined as $\Delta C = C\text{-}C_{T=10K}$ was divided by C_{10K} to remove pellet geometric effects which then becomes equivalent to $\Delta\varepsilon$, is plotted as a percentage against temperature, shown in figure 5.1 (a). $Ni_3V_2O_8$ exhibits a well-known dielectric anomaly at T = 6.3 K which signifies the transition from the paraelectric HTI phase to the multiferroic LTI phase, and this feature can be clearly seen in our sample.

To confirm that this dielectric anomaly is associated with the onset of ferroelectricity, the ferroelectric polarization of the same $Ni_3V_2O_8$ sample was measured. As we do not have the facilities to measure the polarization directly, an alternate measurement was used. The sample was cooled down past the critical temperature under a high polling field (usually ± 200 V), and then the pyrocurrent of the sample was measured while warming at a relatively high rate (usually

4 - 6 K/min). Then the drift in the pyrocurrent as well as noise was reduced, and finally was integrated with respect to elapsed time to obtain the ferroelectric polarization of the sample. Figure 5.1 (c) shows a clear non-zero dielectric polarization developing at T=6.3 K, where we expected to see the onset of ferroelectric ordering. The insert shows the raw pyrocurrent data which shows the sharp peak at T=6.3 K.

As none of these measurements can show the other phase transitions including the Neel temperature, we performed specific heat measurements on $Ni_3V_2O_8$ using the same Quantum Design PPMS. We mixed powder $Ni_3V_2O_8$ with Ag powder (Alfa Aesar catalog # 14450) on 1:1 by weight ratio to improve the thermal conductivity as well as to hold the pellet together, and later correct for the contribution to the heat capacity from Ag. Figure 5.1 (d) shows the heat capacity of the $Ni_3V_2O_8$ sample as a function of temperature, which clearly shows 4 features. T_H=9.1 K peak corresponds to the Neal temperature where the system magnetically orders into the antiferromagnetic HTI phase. T_L=6.3 K peak indicates the HTI to LTI multiferroic transition, and the peak temperature matches well with what is observed in dielectric and pyrocurrent measurements. Smaller peak at T=4 K corresponds to the LTI to CAF transition which is usually difficult to see in powder samples, while the peak at T=2.4 K corresponds to the CAF to C' phase. Heat capacity measurements have the advantage of showing all four magnetic transition temperatures from a single measurement, and thus will be used extensively throughout this thesis to track the phase transition temperatures as dopants are introduced into the $Ni_3V_2O_8$ lattice.

5.2 Zn doped $Ni_3V_2O_8$

After confirming pure $Ni_3V_2O_8$ shows the expected behavior, we measured normalized dielectric constant of Zn doped $(Zn_xNi_{1-x})_3V_2O_8$ samples which is shown in figure 5.2 (a). The dielectric anomaly associated with T_L can be clearly seen in x=0.048 (red squares) and x=0.1 (green triangles), while the x=0.15 sample shows a small feature just above 2 K, and the higher doped samples cannot be measured because the feature moves below 2 K which is below the minimum temperature limit for the PPMS. This shows the samples undergo the ferroelectric transition at least up to 15% doping, which is surprising considering the delicate balance of magnetic interactions in $Ni_3V_2O_8$ that may be disrupted.

(a)

(b)
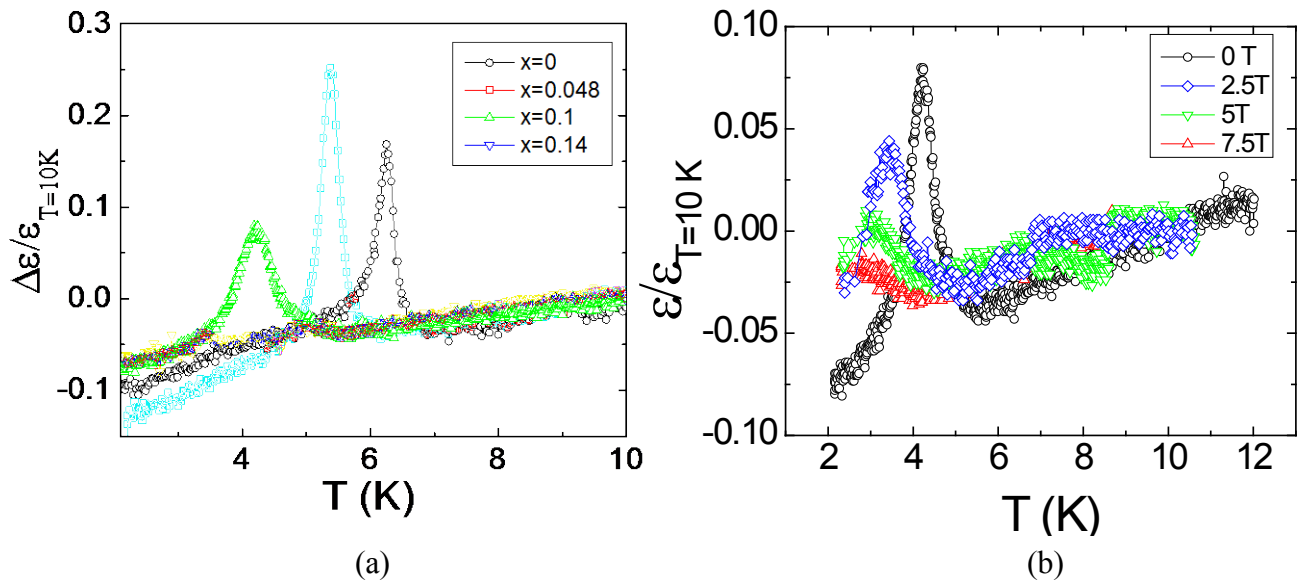
Figure 5.2: (a) normalized dielectric constant vs temperature for $(Zn_xNi_{1-x})_3V_2O_8$ (b) normalized dielectric constant for $(Zn_{0.1}Ni_{0.9})_3V_2O_8$ under different applied magnetic fields

However, we see that the phase transition temperature is suppressed sharply to lower temperatures, while the peak becomes generally shorter and wider as the doping fraction increases, although the transition is not completely destroyed. It is possible the inhomogeneity in these polycrystalline samples is increasing with doping because the peaks become wider. Figure 5.2 (b) shows the behavior of the normalized dielectric constant of the 10% Zn doped $Ni_3V_2O_8$ under different applied fields. The anomaly suppresses to lower temperatures and become less sharp as the externally applied magnetic field is increased, as expected for an antiferromagnetic transition.

To confirm whether this anomaly is indeed observed at the onset of ferroelectricity, we measured the ferroelectric polarization of some of the Zn doped samples. The ferroelectric polarization was calculated by first cooling down the sample past the critical temperature under a high polling field (+/-200 V), then measuring the pyrocurrent while warming up at a fast rate (4-6 K/min, and finally integrating the pyrocurrent with respect to time to obtain the polarization. Figure 5.3 shows the ferroelectric polarization of 10% doped sample plotted together with undoped $Ni_3V_2O_8$. A clear non-zero polarization develops around T ~ 4.5 K, which agrees well with where the dielectric peak observed for this sample, therefore confirming that the dielectric peak is observed indeed at the development of the multiferroic phase.
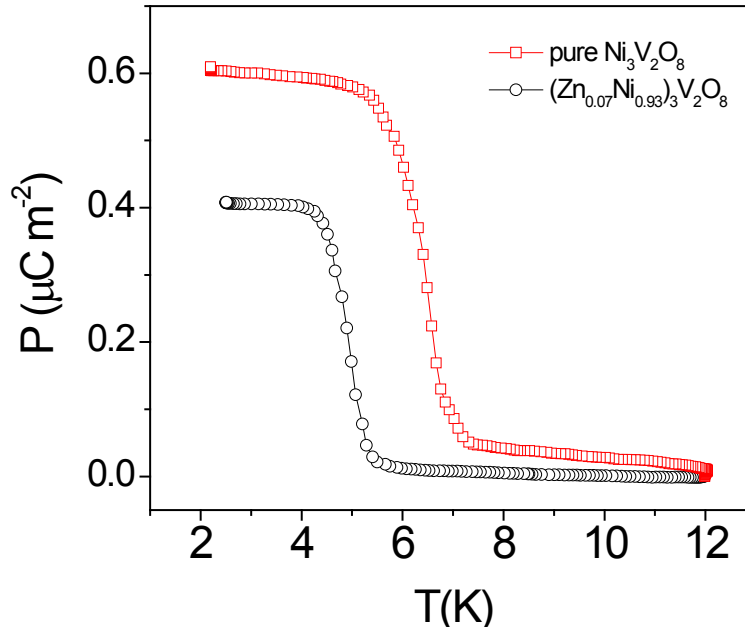
Figure 5.3: Ferroelectric polarization of pure and 7% doped $Ni_3V_2O_8$

To explore what happens to T_H (i.e. the ordering temperature) and the other magnetic phase transitions we measured the specific heat capacity of these samples as a function of temperature, and are shown in figure 5.4 as a plot of C/T vs T. For clarity, only a selected number of Zn doped samples are shown. The curves have been shifted in the vertical direction to further improve clarity. We clearly observe all four phase transitions for lower doped samples, although the peak corresponding to T=4 K transition is hard to observe in higher doped samples as expected. The peak corresponding to T=2.4 K transition moves below the measurable temperature range for higher doped samples, therefore we focus our attention mainly on T_H (Neel temperature) and T_L (multiferroic transition). We see both these transitions suppressing rapidly in temperature with the increase of Zn doping fraction, however both transitions are clearly visible even up to 30% Zn doping.
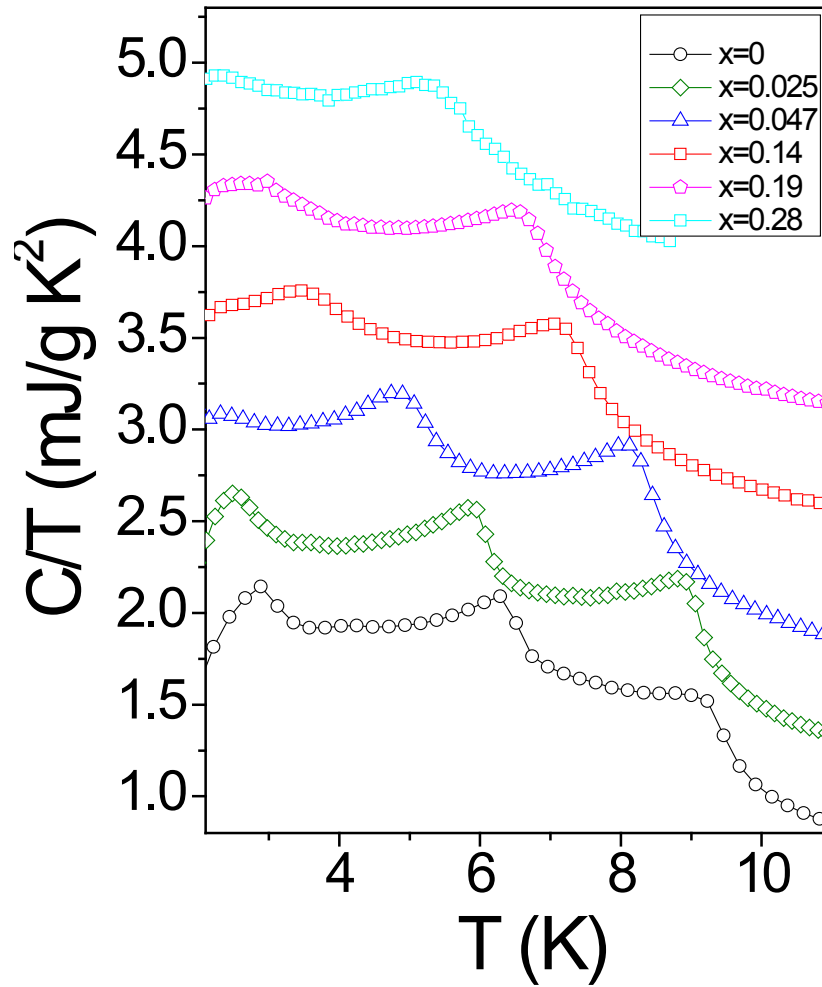
Figure 5.4: Specific heat measurements for $(Zn_xNi_{1-x})_3V_2O_8$

The dielectric data confirms that ferroelectric transition at T_L is persistent at least up to 15% Zn doping, and the heat capacity measurements confirm both T_H and T_L transitions persist even at 30% doping, leading us to believe that the magnetic ordering in $Ni_3V_2O_8$ is remarkably resilient to non-magnetic doping.
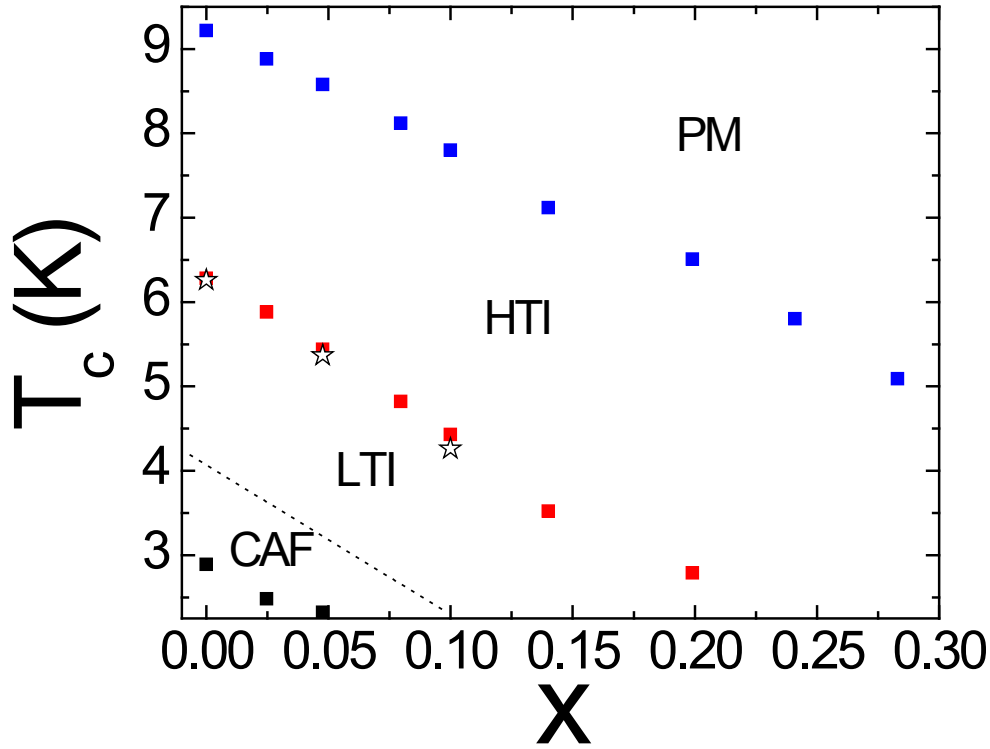
Figure 5.5: $(Zn_xNi_{1-x})_3V_2O_8$ phase diagram; peak temperatures extracted from heat capacity data are shown in squares and the dielectric peak positions are shown in stars, while x represents the Zn doping fraction. The dotted line shows the LTI-CAF phase boundary expected if it follows the same pattern

To further investigate the suppression of the magnetic phases with Zn doping, we plotted the phase transition temperatures as a function of the doping fraction x to create a "phase diagram" for $(Zn_xNi_{1-x})_3V_2O_8$, and is presented in figure 5.5. It immediately becomes evident that the suppression of phase transitions is highly uniform, and is linear in nature. The blue squares represent the phase boundary between the paramagnetic and HTI phase, and corresponds to the T_H suppression, while the red squares represent the phase boundary between the HTI and LTI phase, and corresponds to the multiferroic T_L transition. The black squares represent the

CAF to C' phase boundary, and the dotted line represents how the LTI to CAF boundary would look like if it follows the other phase boundaries' pattern.

To quantitatively investigate the effects of Zn doping, we can analyze the phase diagram in terms of site-diluted Ising and Heisenberg models. As we are limited to a base temperature of 2 K, we have extrapolated phase transition boundaries towards the T=0 axis to probe the suppression. Figure 5.5 shows the behavior of $T_{X=0}$ / T_C plotted against the doping factor x.
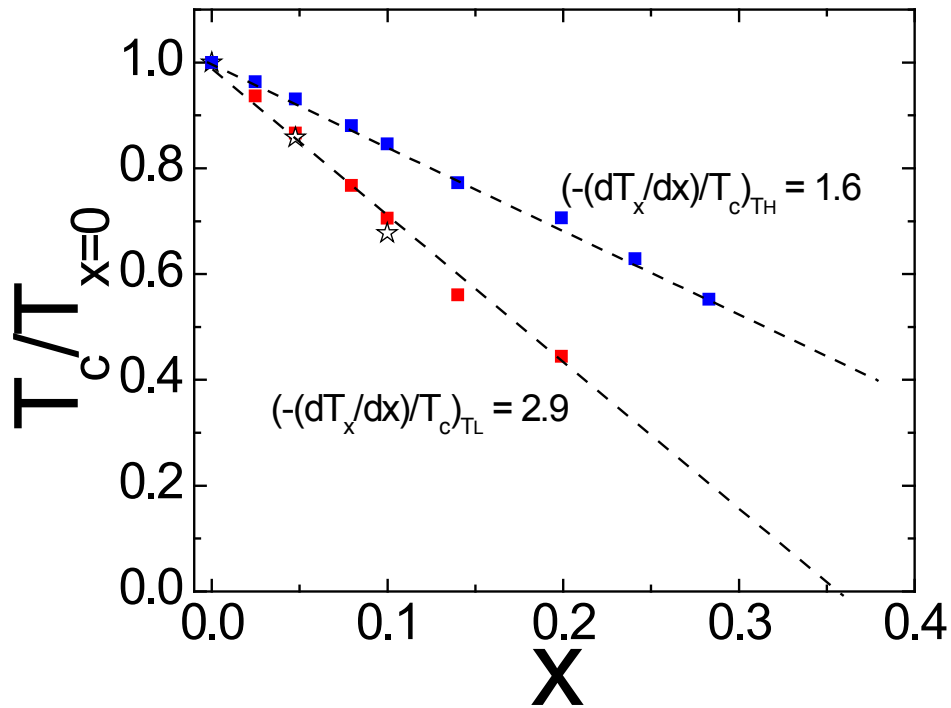
Figure 5.6: of $T_c/T_{x=0}$ plotted against the doping factor x for $(Zn_xNi_{1-x})_3V_2O_8$

From figure 5.6, we can estimate the critical Zn doping percentage necessary to completely suppress the PM to HTI (T_H) and HTI to LTI (T_L) phase transitions from the T = 0 intercepts. These values are $(x_{critical})T_L \approx 0.35$ and $(x_{critical})T_H \approx 0.6$ respectively. For spin-½ Ising spins on a 2-dimensional square lattice, it has been reported that $x_{critical}$=0.41 [64]. Even though

the spin-1 Ni^{2+} ions in $Ni_3V_2O_8$ form a Kagome lattice with triangular components, we have to approximate this to a square lattice since no model currently exists for Spin-½ Ising spins on a triangular lattice.

Furthermore, by calculating the suppression rate (initial slope of the curve), we can extract information about the behavior of spins in the lattice. For 2-D magnetic systems, models predict the slope to be $\approx$ 1.6-1.9 for Ising spins and $\approx$ 3 for Heisenberg spins [65]. The suppression rate calculated for T_H is 1.6, which agrees very well with the expected value for Ising spins. This leads us to believe that the HTI phase has a 2-D Ising like spin structure. The suppression rate for T_L (2.9) agrees well with the expected values of Heisenberg spins. This confirms that the LTI phase predominantly exhibits a 2-D Heisenberg spin structure characteristics while the LTI phase exhibits Ising spin structure characteristics. These results agree well with previous neutron studies on pure $Ni_3V_2O_8$ which have shown the HTI phase has Ising like spins and the LTI phase has Heisenberg like spins as shown in figure 3.3. We were able to confirm the results obtained from neutron studies through our original Zn doping study in 2009, for the first time [66].

Moreover, rather surprisingly, we observed that the magnetic ordering phase transition at T_H clearly persists at 30% Zn doping, from the clear sharp peaks in the heat capacity measurements, while the T_H transition also persists up to this fraction, and remains multiferroic at least up to 15% doping, as verified by the dielectric measurements. Considering the delicate balance of the competing nearest neighbor, next nearest neighbor and Dzyaloshinski-Moriya interactions, the initial expectation was that introducing even a few percent of a dopant into the lattice will destroy at least the magnetically driven ferroelectric ordering, however, the phase

diagrams in figures 5.5 and 5.6 are strong evidence that this is not the case. This leads us to believe that the microscopic magnetic interactions in $Ni_3V_2O_8$ leading to multiferroic ordering as well as the magnetic ordering transition is remarkably resilient against non-magnetic doping. This is an important first step in tuning the properties of multiferroics by doping as a whole, because if a material is resilient to doping at least up to its percolation threshold, this gives the opportunity to explore a wide range of doping fractions in order to enhance its magnetoelectric properties.

Later studies have shown a similar resilience to non-magnetic doping for another multiferroic material, $MnWO_4$. $MnWO_4$ undergoes 3 magnetic phase transitions at low temperatures. It has a magnetic ordering temperature of $T_N = 13.5$ K, while an incommensurate, spatial inversion symmetry breaking helical non-collinear spin structure forms at $T_C = 12.6$ K. A further commensurate spin structure develops at $T_L = 7.8$ K. A study by Meddar *et.al.* [49] finds that the multiferroic transition in $MnWO_4$ persists even at 30% non-magnetic Zn^{2+} and Mg^{2+} doping for polycrystalline samples. Moreover, they find that the magnetic ordering temperature at $T_N = 13.5$ K as well as the multiferroic ordering temperature at $T_C = 12.6$ K suppresses linearly with the increase in Zn^{2+} and Mg^{2+} doping fractions, while the suppression rates remain similar for Zn^{2+} and Mg^{2+}. A similar study by Chaudhury *et.al.* [50] on single crystals finds that $MnWO_4$ retains its magnetic characteristics even at 50% Zn^{2+} doping, where both T_N and T_C are observed in polarization and heat capacity measurements. They also confirm the linear behavior of the suppression of T_N and T_C with the increase of Zn fraction, although T_L shows a much more rapid suppression compared with these.

However, the rate of suppression of non-magnetic ion doped $Ni_3V_2O_8$ and $MnWO_4$ are markedly different. $MnWO_4$ shows a much smaller rate of suppression for T_N and T_C with non-magnetic doping as compared with similar transitions of $Ni_3V_2O_8$. This demonstrates the difference of the dimensionality of spin structures between these two materials; the faster suppression in $Ni_3V_2O_8$ is consistent with site dilution in a 2-dimensional spin system, which agrees well with the layered Kagome type spin structure discovered from neutron studies as discussed earlier, while the relatively small suppression of T_N and T_C in $MnWO_4$ is reminiscent of the 3-dimensional character of the magnetic interactions in $MnWO_4$.

CHAPTER 6

MAGNETIC DOPING OF $Ni_3V_2O_8$

As discussed in the previous chapter, $Ni_3V_2O_8$ is highly resilient to non-magnetic doping with the rate of suppression agreeing well with non-magnetic site dilution for a 2-dimensional spin system. Another multiferroic system, $MnWO_4$, shows similar resilience to non-magnetic Zn and Mg doping. However, studies have found that Fe and Co magnetic doping of $MnWO_4$ is strikingly different from non-magnetic doping [51, 52] where 4% doping of Fe completely destroys the multiferroic ordering in $MnWO_4$. This motivated us to further investigate how the phase transitions including the multiferroic ordering in $Ni_3V_2O_8$ respond to magnetic dopants with different spins. We started with lowest spin (Spin-1/2 Cu) and proceeded to spin-3/2 Co, spin-2 Fe and spin-5/2 Mn, which is the highest spin dopant possible from the transition metal group. All these dopants have roughly the same ionic radii as Ni^{2+}, so we expected these dopant ions would have no problems fitting into the Ni^{2+} site. We start with smaller doping fractions to observe the effects below the percolation threshold, and depending on how the phase transitions are suppressed and how well the samples can be synthesized we move onto higher doped samples.

6.1: Spin-1/2 Cu doping of $Ni_3V_2O_8$

As a first step of creating a taxonomy of effects of different magnetic dopants on $Ni_3V_2O_8$, we started with a lowest non-zero spin transition metal magnetic ion, spin-1/2 Cu.

After confirming the proper phase and the doping fraction dielectric merasurements for different Cu fractions were performed and are presented in figure 6.1 (a). With Cu doping, we see a qualitatively similar behavior to Zn doping where the dielectric peaks are suppressed in temperature while peaks become less intense and wider as the doping fraction increases. However, quantitatively Cu doping differs significantly from Zn. We observe the dielectric anomally associated with the onset of ferroelectric ordering in x=0.03 , 0.04 and 0.05 curves in the form of a sharp peak similar to Zn doped samples, which however completely vanishes by x=0.1. The featureless dielectric curve for x=0.1 sample suggests the multiferroic transition may have been completely destroyed by introducing 10% spin-1/2 Cu ions into the magnetic lattice.
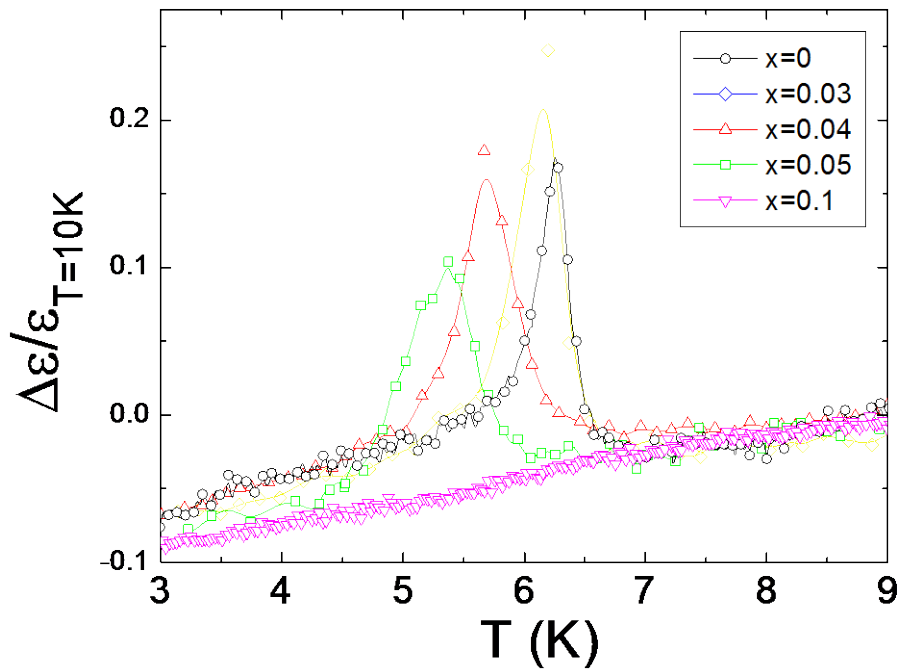
Figure 6.1: Normalized dielectric constant for $(Cu_xNi_{1-x})_3V_2O_8$ compared with undoped $Ni_3V_2O_8$
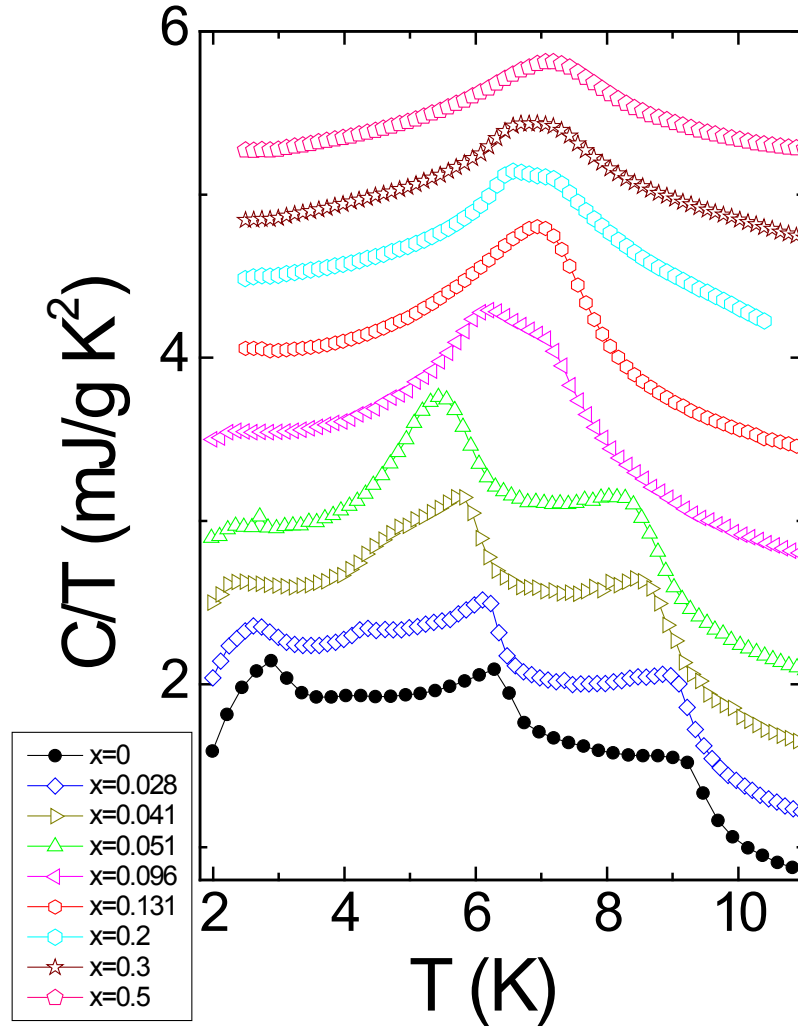
Figure 6.2: Specific heat capacity data plotted as a function of C/T vs T for various $(Cu_xNi_{1-x})_3V_2O_8$ samples. Curves have been shifted in the vertical direction for clarity

To confirm this behavior as well as to explore what happens to T_H with Cu doping, we performed specific heat capacity measurements on Cu doped samples from x=0.03 all the way to x=0.5. At low doping fractions (up to x=0.05) anomalies at both T_L and T_H can be clearly observed at the heat capacity data. At x=0.1, these two features seem to start combining into one feature, and by x=0.13 there is clearly only one feature. This confirms what the dielectric data

suggests, i.e. by 10% doping, the ferroelectric transition is completely suppressed and T_H and T_L combine into a single phase transition.

It should be noted that this single peak at x=0.13 separates slightly to become a broader feature for x=0.2 and x=0.3, which in turn combines into a single peak again at x=0.5. The reason for this may lie in inhomogeneity of the samples due to the different synthesis techniques used. Metal organic synthesis was used to prepare samples up to x=0.13, while the higher doped samples were made through solid state reactions. While all these dopant fractions were verified by EDS and are accurate, EDS confirmed that the x>0.13 samples shows a small spreading of dopant fraction values in the same sample. When different powder samples of the same batch were analyzed using EDS, doping fraction x had a change of about 20%-30% within the sample for x>0.13 samples, hence multiple EDS values for x were averaged to obtain a more accurate number. For x>0.13 samples, if some areas of a particular sample have less Cu concentration than other areas, such an area may show less suppression of the $Ni_3V_2O_8$ features than expected for that particular doping fraction. Hence we observe the combining of the peaks for x=0.13, then a slight separation of peaks for x=0.2 and 0.3 slightly inhomogeneous samples, and finally combining of the peaks at x=0.5 where we can expect there is a sufficient Cu fraction everywhere in the sample (even with inhomogeneities) to completely suppress one phase transition.

This data confirms that Cu doping has a much stronger effect than Zn doping for magnetic ordering temperature as well as the ferroelectric ordering in $Ni_3V_2O_8$. To further investigate this phenomenon, we performed magnetization measurements on the Cu doped samples where something very interesting was discovered. When Cu dopant fraction is

increased, we observed a huge increase in magnetic moments of the samples. Figure 6.3 compares the magnetic moments of the different samples, plotted in units of Bohr magnetons per transition metal ion. While the pure polycrystalline $Ni_3V_2O_8$ samples have a magnetic moment of 0.08 μ_B per Ni Ion, the 5% Cu doped sample has a moment of 0.65 μ_B per TM ion below T_C while the 20% doped sample has a moment of 2.5 μ_B per TM ion. This shows introducing 5% spin-1/2 Cu into the $Ni_3V_2O_8$ lattice can increase the magnetic moment by a factor of 8. This sizeable net magnetic moment in the ferroelectric phase for samples having a small Cu fraction is significant. Almost all of the known multiferroic materials are antiferromagnets and therefore show a negligible (albeit non-zero) magnetization in the multiferroic phase. This result offers the unique possibility of obtaining a net ferroelectric polarization simultaneously with a net magnetization in this system, which is a much desirable property for device development. However, when the doping fraction is increased above x ~0.1, the rapid increase of magnetization in the ordered phase as well as the onset of non-zero magnetization moving towards higher temperatures suggest that the $Cu_3V_2O_8$ type magnetic structure is present and that the $Ni_3V_2O_8$ magnetic structures are strongly suppressed, so the window of interest for Cu doping is limited to x=0.3 to x=0.5.
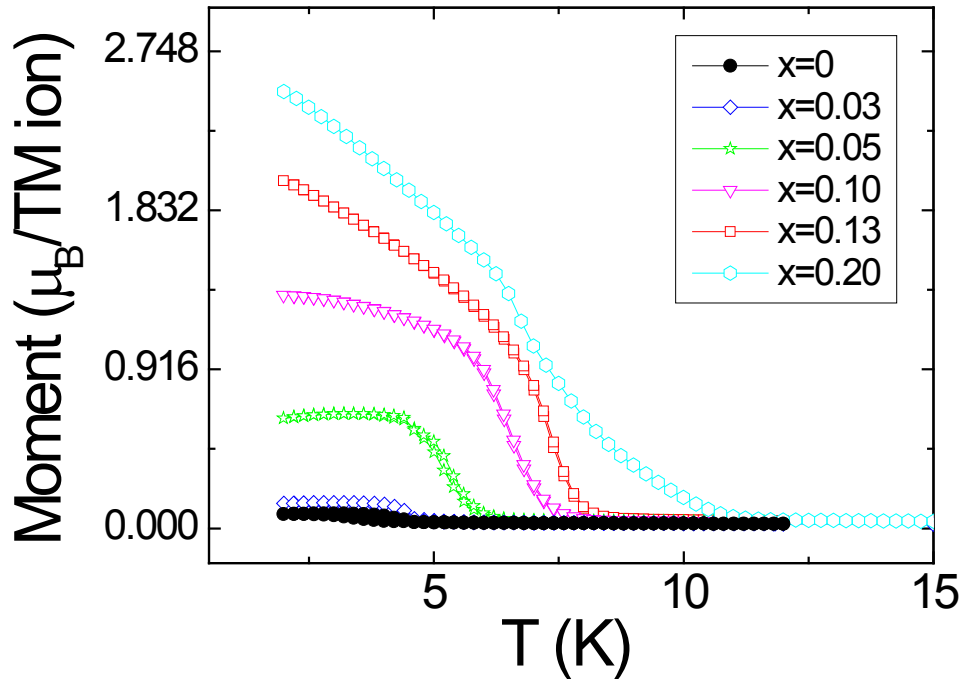
Figure 6.3: Magnetization as a function of T for various $(Cu_xNi_{1-x})_3V_2O_8$ samples

To further investigate this critical region as well as to confirm the onset of multiferroic ordering, we measured the ferroelectric polarization of some of the Cu doped samples and are presented in figure 6.3. Samples doped with small amounts of Cu are clearly ferroelectric as seen from the rapid divergence of magnitude from zero near the T_L=6.3 K transition, while the magnitude of polarization also increases for smaller Cu fractions. However, it should be noted that due to the nature of the pyrocurrent measurements, noise removal is necessary and as a result the magnitude of final polarization may not be extremely accurate, while the temperature axis remains very accurate. So we do not put much significance on the magnitude of polarization. The 10% Cu doped sample shows no pyrocurrent peak, and hence shows no calculable ferroelectric polarization.
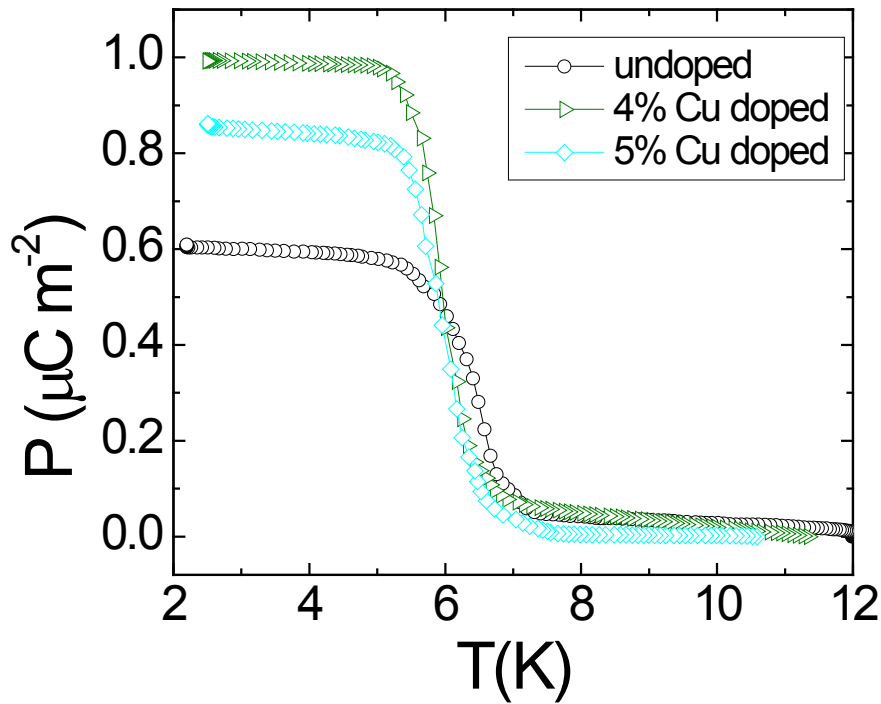
Figure 6.4: Development of ferroelectric polarization for various $(Cu_xNi_{1-x})_3V_2O_8$ samples

From these results, 5% was chosen as the optimal doping limit for coexistence of polarization and a relatively large net magnetic moment. To check for magnetoelectric coupling in this doping region, we measured the field dependent dielectric constant of the 5% Cu doped sample. This is shown in figure 6.5, which shows a clear dependence of the dielectric constant on the applied field, although the change in dielectric constant remains small and is just under 1% at +/- 4 T applied field.
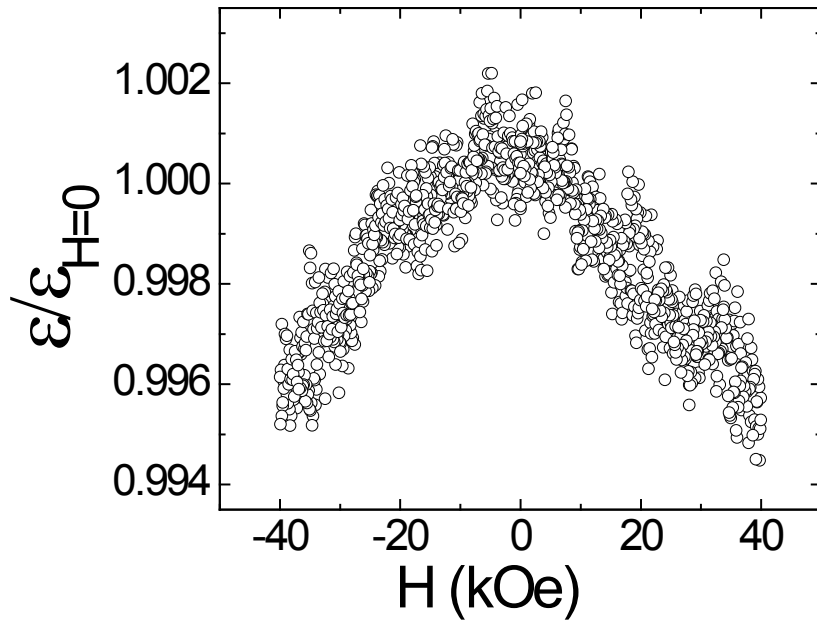
Figure 6.5: Field dependent dielectric constant for $(Cu_{0.05}Ni_{0.95})_3V_2O_8$, plotted as a function of $\varepsilon/\varepsilon_{zero\ field}$ vs applied magnetic field

This confirms that the 5% Cu doped sample shows clear signs of magnetoelectric coupling, while showing a sizable net magnetization as well as a ferroelectric polarization. This is a desirable property to have in a material used for device development, and shows the exciting prospect of having all 3 properties in multiferroic materials. These motivating Cu doping results as well as the Co doping presented in the next section has been reported in Physical Review B in 2011 [67].

6.2: Spin-3/2 Co doping of $Ni_3V_2O_8$

Cu doping offered the enticing possibility of obtaining net ferroelectric polarization simultaneously with a net magnetization for a very small dopant range, although above the critical dopant fraction x=0.1, the magnetic ordering of $Ni_3V_2O_8$ suppresses completely. To compare how other magnetic dopants behave as a part of this systematic study, results from spin-3/2 Co doping is presented in this section.
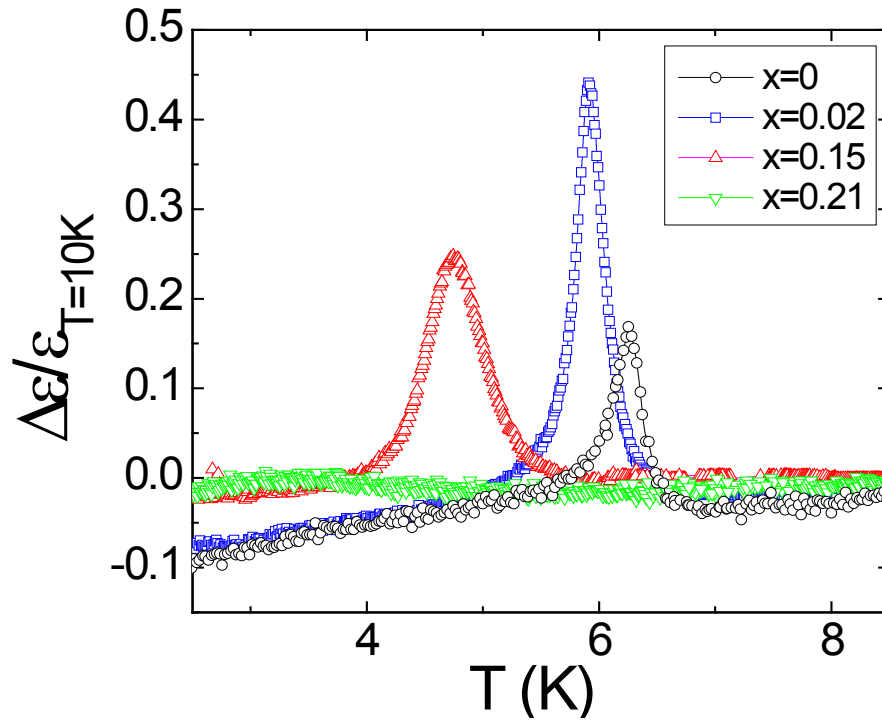
Figure 6.6: Normalized dielectric constant for $(Co_xNi_{1-x})_3V_2O_8$ compared with undoped $Ni_3V_2O_8$

We follow the same experimental procedure and measured the temperature dependent dielectric constant for Co doped $Ni_3V_2O_8$ samples. Figure 6.6 shows the normalized dielectric constant for selected samples (2%, 15% and 21% doped), in which a sharp dielectric anomaly

associated with the onset of ferroelectric ordering persists in samples up to x=0.15. The x=0.21 doped sample also show a wide peak just below 4 K. It becomes evident that spin-3/2 Co affects the multiferroic ordering to a much lesser extent that Cu doping, which destroyed the multiferroic ordering above x=0.1.

To confirm that this dielectric anomaly is observed at the onset of ferroelectric ordering, we measured the ferroelectric polarization of some of the Co doped samples using the same pyrocurrent integration method discussed earlier.
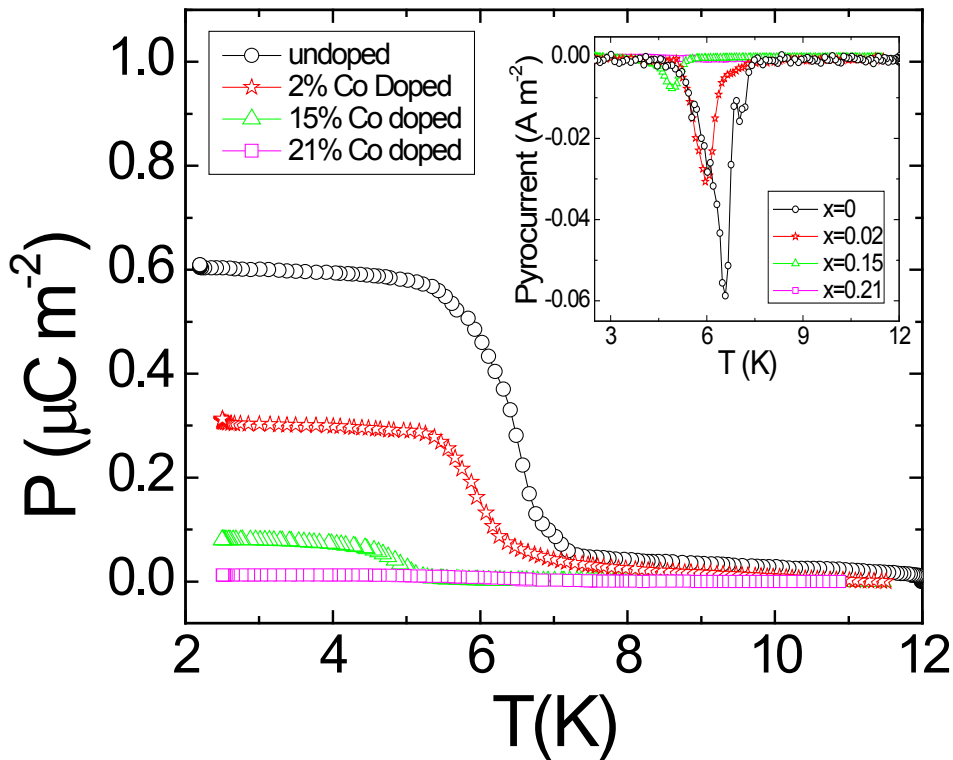
Figure 6.7: Ferroelectric polarization of selected $(Co_xNi_{1-x})_3V_2O_8$ samples compared with undoped $Ni_3V_2O_8$. Insert: the corresponding pyrocurrent curves

Figure 6.7 shows the ferroelectric polarization of $(Co_xNi_{1-x})_3V_2O_8$ samples for x=0, 0.02, 0.15 and 0.21. The insert figure shows the raw pyrocurrent curves that were integrated to obtain the polarization. Sharp pyrocurrent peaks that translates to clear non-zero polarizations in the vicinity of the T_L = 6.3 K transition can be observed for samples up to x=0.15, while a very small feature and a small non-zero polarization can be seen for the x=0.21 sample. It is also evident that the onset of the polarization shifts to lower temperatures with the increase of the Co doping fraction. This confirms that the multiferroic ordering in the $(Co_xNi_{1-x})_3V_2O_8$ system persists at least until x~0.21.

To investigate the behavior of the magnetic ordering temperature (T_H) with Co doping, we measured the specific heat capacity of $(Co_xNi_{1-x})_3V_2O_8$ samples. Figure 6.8 plots the heat capacity data for selected of the $(Ni_{1-x}Co_x)_3V_2O_8$ samples for the composition range x = 0 all the way to x=1. The two peaks associated with T_H and T_L can be clearly seen in these samples. When the Co content is increased, both transitions shift to lower temperatures. However, the peak associated with the multiferroic transition remains visible until a Co fraction of x = 0.25. The higher temperature anomaly, associated with the transition into the HTI phase, remains visible and suppresses to lower temperatures similarly. However, it shows considerable broadening for x>0.30, but is still visible at compositions up to x=0.56. This motivated us to prepare and study samples all the way up to x=1 (pure $Co_3V_2O_8$). $Co_3V_2O_8$ has a very similar crystal structure to $Ni_3V_2O_8$, although it has not shown multiferroic behavior. However, due to the complex lattice, $Co_3V_2O_8$ phase diagram remains similarly complex.
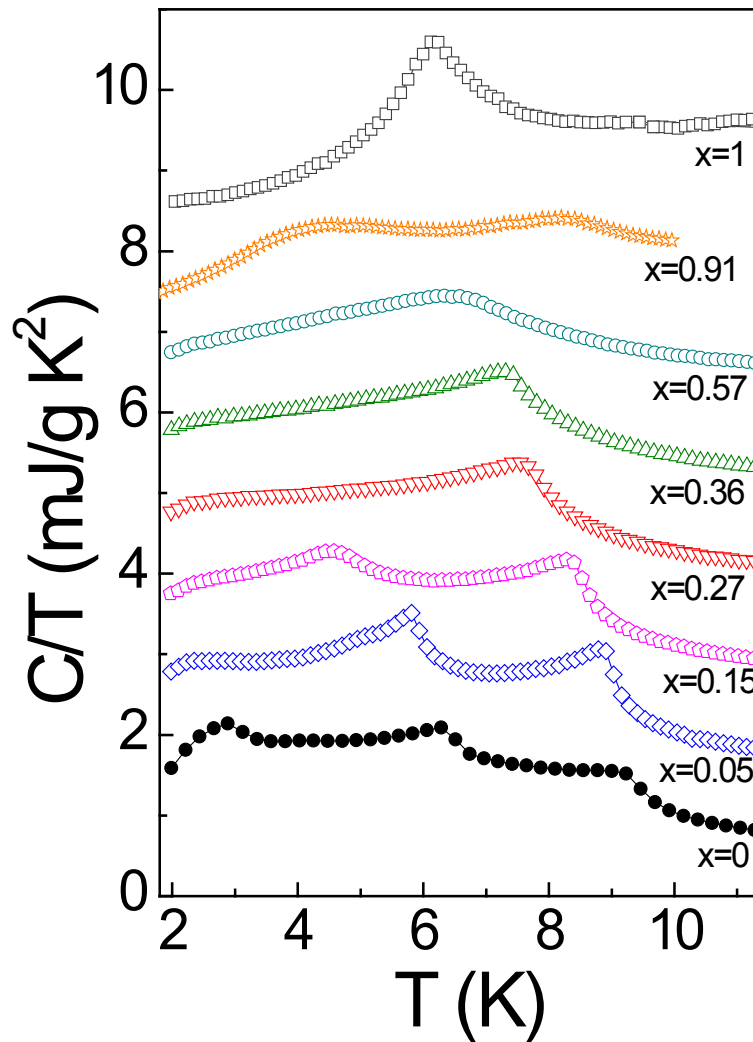
Figure 6.8: Specific heat capacity data plotted as a function of C/T vs T for various $(Co_xNi_{1-x})_3V_2O_8$ samples. Curves have been shifted in the vertical direction for clarity

When we measured the heat capacity of pure $Co_3V_2O_8$, we observed two peaks corresponding to phase transitions at 6.1 K and 11.7 K. Although $Co_3V_2O_8$ exhibits multiple magnetic phase transitions [68], these are the two transitions most readily distinguished in heat capacity measurements on powder samples [69] because the sharp peaks associated with

multiple transitions in a very small temperature range is difficult to discern in polycrystalline samples, and would only be visible on a single crystal measurement. When we consider the Co rich side of the heat capacity data, we observe these two transitions are also suppressed with increasing Ni fraction (decreasing values of x), with the rate of suppression being much larger that observed for $Ni_3V_2O_8$ on doping with Co. Rather unexpectedly, these results suggest that doping with spin-1/2 Cu more strongly suppresses the magnetic transition temperatures in $Ni_3V_2O_8$ than doping with spin-3/2 Co.

As a first step of parameterizing how Zn, Cu and Co change the magnetic properties of $Ni_3V_2O_8$, using the magnetization data of these samples under an external field of 100 Oe, the inverse magnetic susceptibility of four representative samples, 10% Zn, Cu, and Co doped samples together with undoped $Ni_3V_2O_8$ are plotted as a function of temperature and is presented in figure 6.9. As expected, all four samples show linear behavior that is anticipated from the paramagnetic region of these samples. The effected moment per transition metal ion in the higher temperature region of these samples can be calculated using the Curie-Weiss law, $\chi=C/(T-T_\theta)$, where $C=Ng^2\mu_B^2 J(J+1)/3k_B$ is the Curie constant and T_θ the Weiss temperature. The spin-only value (J=S) agree better with the measured values. This is attributed to the orbital quenching observed in many transition metal oxides. The effective moment per Ni ion is 3.5 μ_B for undoped $Ni_3V_2O_8$, while the effective moments per transition metal ion are 3.3 μ_B, 3.4 μ_B and 4.0 μ_B for $Ni_3V_2O_8$ doped with Zn, Cu, and Co respectively.
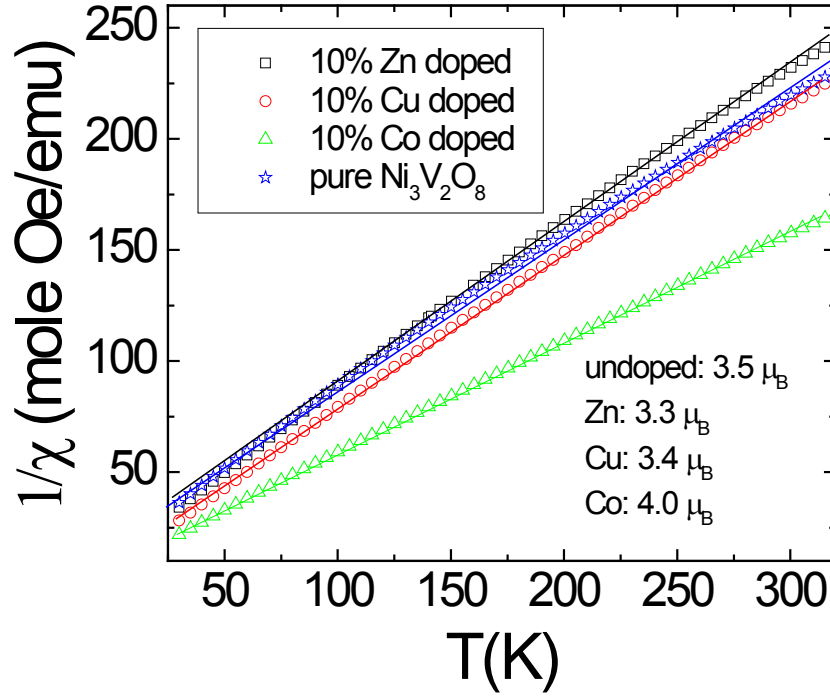
Figure 6.9: Magnetic Susceptibility of 10% Zn, Cu and Co dopes samples plotted together with undoped $Ni_3V_2O_8$. The lines show the best linear fit from which effective moments are calculated

As the spin-1 Ni^{2+} ions are replaced with lower spins, i.e. spin-0 Zn and spin-1/2 Cu, it can be expected that there will be a net reduction of the effective moment. Therefore, the 3.3 μ_B, 3.4 μ_B values for Zn and Cu doped samples, compared with 3.5 μ_B for the undoped sample, correspond to the expected change in the system. Similarly, as the spin-1 Ni^{2+} ions are replaced with higher spins, spin-3/2 Co^{2+} in this case, there should be an increase in effective moment and the 4.0 μ_B moment in the Co doped sample represent this expected change in the magnetic response of the system. The Curie-Weiss temperatures can also be calculated from this data, which for pure $Ni_3V_2O_8$ is T_c = -31.96 K which agrees with the published values which ranges

from ~-17 K to 30 K [70, 5]. For 10% Zn, Cu, and Co doped $Ni_3V_2O_8$, the Curie-Weiss temperatures are -21.45 K, -14.04 K, and –17.52 K respectively.

In order to further understand the effects of the different dopants on the magnetic phases of $Ni_3V_2O_8$, we plot a combined phase diagram for $(Ni_{1-x}Co_x)_3V_2O_8$ for x = 0 to x = 1, and $(Ni_{1-x}Cu_x)_3V_2O_8$ for x = 0 to x = 0.5 in figure 6.10. This figure constructed by extracting peak positions from dielectric, magnetic, and heat capacity measurements allows us to directly compare the effects of the 3 dopants discussed so far.
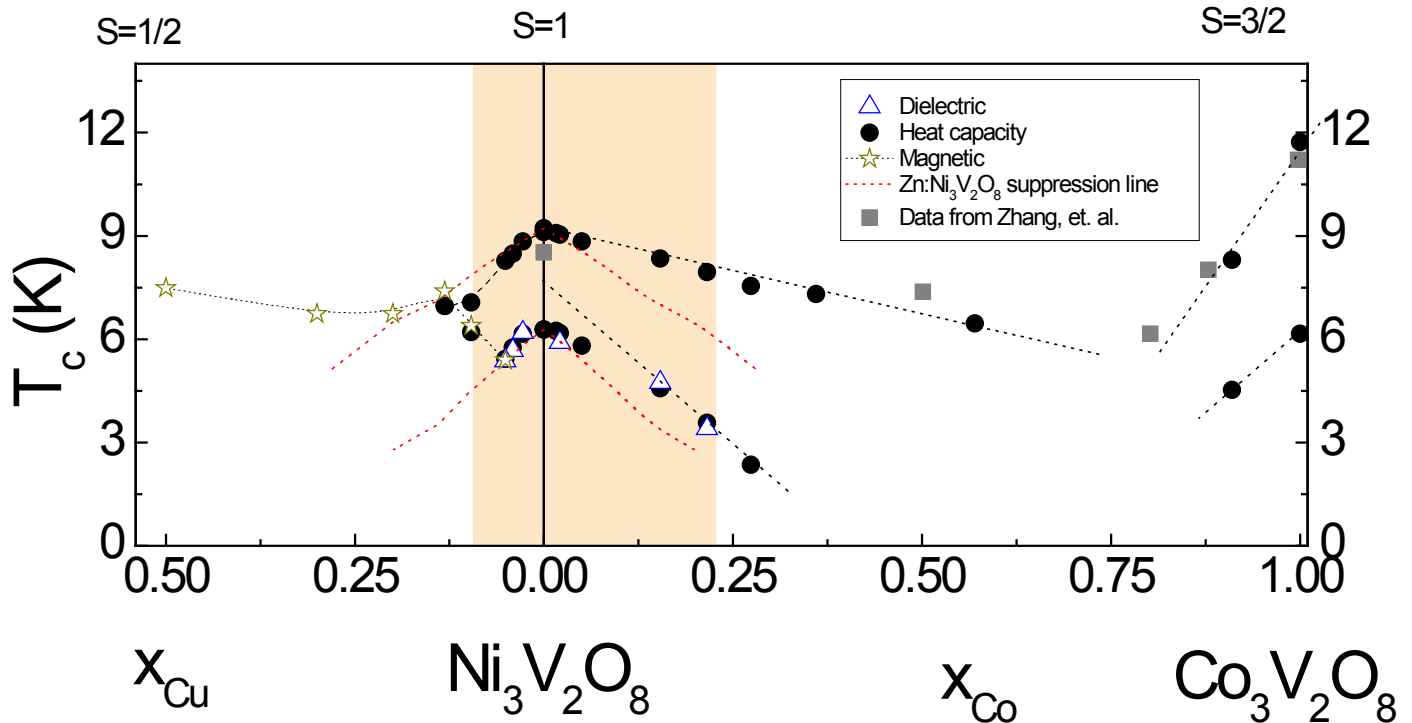
Figure 6.10: Combined phase diagram for Cu and Co doped $Ni_3V_2O_8$. Left panel shows Cu doping and the right panel shows Co doping, while spins change from ½ to zero to 3/2 along the x axis. Red dotted line indicates the suppression line for Zn doping

This phase diagram is presented as a gatefold figure, with the chemical composition x varying along the horizontal axis. The dopant spin also varies from s = ½ (Cu) to s = 3/2 (Co) from left to right on the x axis. Open triangles represent the phase transitions extracted from dielectric measurements, while the phase transitions determined from heat capacity data are shown as solid circles, and the transitions determined from magnetic measurements for x>0.13 for Cu doping is denoted by open stars. The red dotted lines shown on both sides of the fold show the Zn substituted $Ni_3V_2O_8$ phase boundaries presented in the previous chapter, and are included as a guide for comparing between the different dopants. The black dotted lines are also drawn as a guide, showing the paramagnetic-HTI and HTI-LTI phase boundaries. The shaded region indicates the compositional range developing multiferroic order according to the various measurements. The temperatures extracted from peak positions of heat capacity, polarization and magnetization measurements agree very well with each other. Figure 6.10 also includes the magnetic ordering temperature for $(Ni_{1-x}Co_x)_3V_2O_8$ for different compositions measured by Zhang et. al [57] (gray squares), which are in good qualitative agreement with our results.

The magnetic transitions in $Ni_3V_2O_8$ doped with spin-3/2 Co show a relatively linear decrease in transition temperatures with an increasing Co percentage. The minimum in the Neel temperature is estimated to be just under 6 K near x=0.80, which is also in good agreement with previous investigations [57]. The suppression of magnetic order on doping is much more pronounced on the Co-rich side of the phase diagram than on the Ni-rich side, indicating the robust nature of $Ni_3V_2O_8$ to Co doping and the sensitive nature of $Co_3V_2O_8$ to Ni doping. However, surprisingly, the suppression in transition temperatures on doping with spin-3/2 Co is smaller than that obtained on doping with spin-0 Zn. The initial rate of suppression in the transition temperatures is much larger for Cu doping than for Co doping. The rate of suppression

for Cu is similar on Cu doping to that observed for Zn doping initially. Above approximately 5% Cu doping, the heat capacity peak associated with the HTI to LTI transition in pure $Ni_3V_2O_8$ shifts to higher temperatures while the onset of magnetic ordering continues to be suppressed to lower temperatures. At 13% Cu doping, we observe only one clear magnetic ordering transition reaching a minimum transition temperature near x~0.2. This, along with the increase of magnetization in figure 6.3 for Cu doping, suggests that the magnetic structure for even modest Cu fractions may be closer to that found in $Cu_3V_2O_8$. This is unlike the situation for Co doping, where we did not find any evidence for $Co_3V_2O_8$ magnetic phases emerging until x~0.8.

As discussed in chapter 5, the non-magnetic doping of $MnWO_4$, another Kagome lattice multiferroic material, is qualitatively similar to $Ni_3V_2O_8$, where the multiferroic transition as well as the magnetic ordering transition is remarkably resilient to non-magnetic dopants Zn and Mg, and was found to be suppressed linearly with the increase of doping fraction [49, 50]. For Co doping, the transition temperature can be relatively stable [52], where the multiferroic transition persisted even at 15% doping of the $MnWO_4$ lattice, similar to our observations where the multiferroic transition in $Ni_3V_2O_8$ persisted even at 20% Co doping. However, Fe doping very strongly suppresses the magnetic ordering in $MnWO_4$ [51], where the multiferroic transition is destroyed by 5% Fe doping. In the case of $Ni_3V_2O_8$, we found Cu doping behaves similarly with 8% doping completely destroying the multiferroic ordering. In order to controllably tune the properties of $Ni_3V_2O_8$ and similar multiferroics through doping, it will be crucial to understand the mechanisms affecting the suppression of the ferroelectric transition temperature and, in particular, explain the qualitatively different behaviors observed on doping Co and Cu.

One possibility is that the development of a net ferromagnetic moment in $Ni_3V_2O_8$ with Cu doping, acts to quench the ferroelectricity. Introducing a weak ferromagnetic component through doping has been shown to modify the magnetic symmetry and strongly affect the magnetoelectric coupling in other systems [71]. The onset of weak ferromagnetism in the canted antiferromagnetic phase of undoped $Ni_3V_2O_8$ destroys the ferroelectric order, although this is typically associated with the vanishing of the inversion symmetry breaking low temperature incommensurate magnetic structure. However, attributing the rapid suppression of the multiferroic transition temperature in Cu substituted $Ni_3V_2O_8$ to the emergence of a ferromagnetic moment does not explain the similarly rapid decrease of T_C in Fe substituted $MnWO_4$, since no net magnetization develops in this system [52].

Another possibility, motivated by the compositional phase diagram shown in Fig. 6.10, is that the $Cu_3V_2O_8$ magnetic structure is more stable against doping than the $Ni_3V_2O_8$ magnetic structure, which is in turn more stable than the $Co_3V_2O_8$ structure. While this explanation is unsatisfying, as it depends on estimating the energetics of these different spin structures, we note that the magnetic ordering temperature of T_N=29 K for $Cu_3V_2O_8$ is significantly larger than the ordering temperature for $Ni_3V_2O_8$ (9 K) or $Co_3V_2O_8$ (11 K), which could be consistent with a more stable magnetic structure. This suggestion could be checked by mapping out the phase diagram for Co substituted $Cu_3V_2O_8$, which we would expect to agree with that measured for pure $Cu_3V_2O_8$ until relatively large Co fractions are introduced. Furthermore, the quantitatively different suppression in the ferroelectric suppression in $MnWO_4$ on Fe [51] and Co [52] doping can also be attributed to the emergence of new spin structures, particularly for Co doping, which suggests that the stability of the multiferroic phase may depend sensitively on the detailed nature of the dopants.

Finally, these measurements offer the tempting possibility that Cu substituted $Ni_3V_2O_8$ may be simultaneously ferroelectric and exhibit a small net magnetization, at least over some small range of temperatures and compositions. This opens the possibility of controlling the ferroelectricity through coupling to a ferromagnetic, rather than antiferromagnetic, spin structure. This would allow the response to more readily tuned using an applied magnetic field and for the magnetic structure to be probed using magnetometry rather than neutron scattering. Moreover, if the strong suppression of the multiferroic transition temperature on Cu doping can be understood, this may also suggest a route for introducing weak ferromagnetic properties in other multiferroic systems through doping with judiciously selected magnetic ions.

6.3: Spin-2 Fe doping and Spin-5/2 Mn doping of $Ni_3V_2O_8$

To further investigate how different spins affect the magnetic ordering in $Ni_3V_2O_8$, two other systems $(Fe_xNi_{1-x})_3V_2O_8$ and $(Mn_xNi_{1-x})_3V_2O_8$ were studied and the preliminary results are presented in this section. Spin-1/2 Cu doping and spin-3/2 Co doping of $Ni_3V_2O_8$ delivered markedly different results, where Cu doping surprisingly had a strong effect on magnetic ordering in $Ni_3V_2O_8$ while the effect of Co doping was very much smaller, even more so than expected with simple site dilution. The next step, naturally, is to investigate how transition metals with higher spins would cope as dopants. We started with spin-2 Fe^{2+}, and continued to the highest spin transition metal ion, Mn^{2+}.

Unfortunately, we encountered unexpected complications with our dielectric probe, and hence had to study the magnetic transition temperatures through heat capacity and magnetic measurements. As the dielectric, polarization and heat capacity peaks matched perfectly for all

samples for Zn, Cu and Co doping, it is reasonable to utilize heat capacity measurements to track changes in T_H and T_L for Fe and Mn doping. Figure 6.11 shows the specific heat capacity measurements from x=0.02 to x=0.3 for $(Fe_xNi_{1-x})_3V_2O_8$ samples.
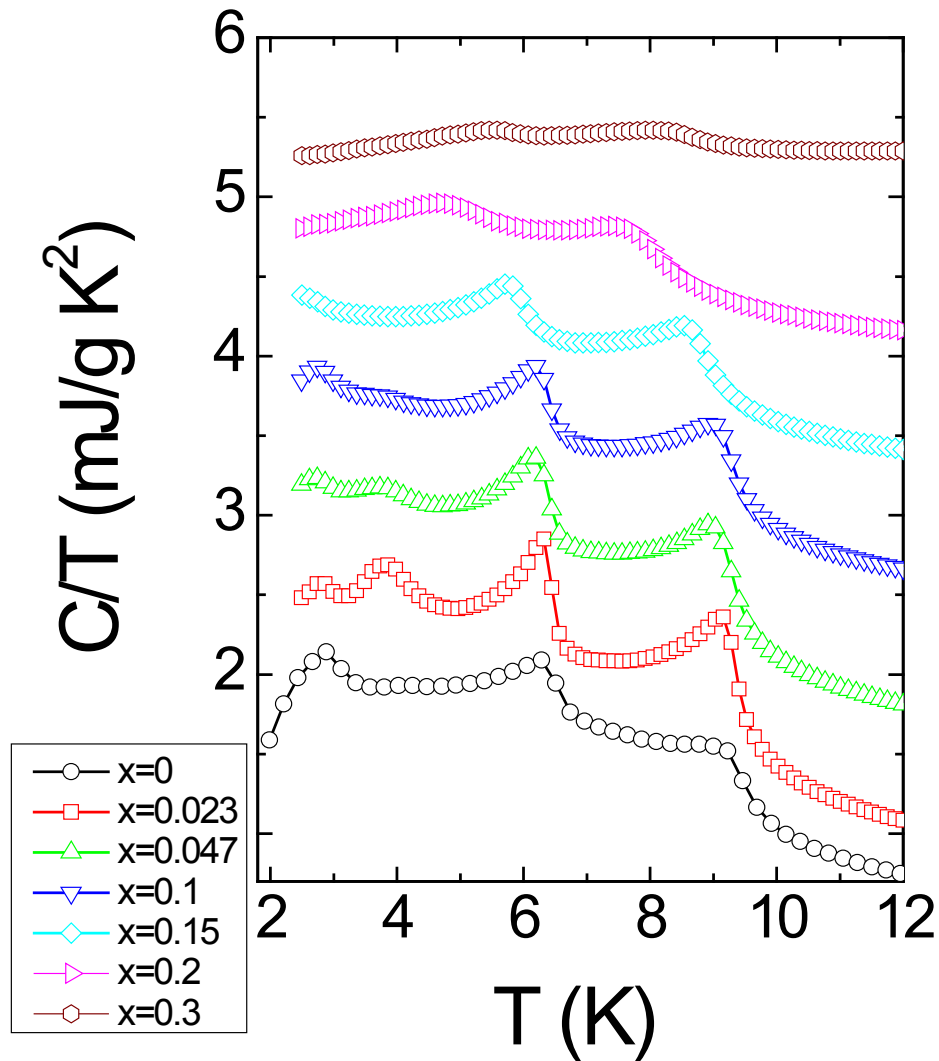
Figure 6.11: $(Fe_xNi_{1-x})_3V_2O_8$ specific heat capacity measurements

All samples, even at 30% Fe doping, clearly show the thermodynamic anomalies associated with both T_H and T_L magnetic transitions. At low doping fractions, transition temperatures show very little suppression while the peaks remain sharp compared with undoped $Ni_3V_2O_8$. Above x>0.2, peaks become considerably wider and less pronounced, however both features are clearly visible. This suggests that Fe doping has an extremely small effect on the magnetic ordering in the HTI and LTI phases in $Ni_3V_2O_8$ below the percolation threshold. This is surprising considering Cu doping had a very strong effect, and it is reasonable to expect that replacing spin-1 Ni ions with spin-2 Fe ions would have a larger effect than replacing them with spin-1/2 Cu ions, which is closer in spin to the Ni ions that it's replacing.

To clarify these results, the DC magnetization of two of the lower doped samples were measured using the SQUID magnetometer and are shown in figure 6.12 (a). The magnetic anomaly associated with the ~4 K transition can clearly be seen in both the 2% and 5% samples. However, there is a significant difference in magnetic moments between the two samples, including the T>9 K region where the material is expected to be paramagnetic. This led us to believe there may be some impurity phases in the sample, even though the XRD and Raman data showed no sign of any impurities. To clarify this, AC magnetization of these samples under a 10 Oe excitation were measured in the entire temperature range T = 2 K to 300 K, and are presented in figure 6.12 (b). Ac magnetization measurements are usually more sensitive to impurity phases because they provide both the in-phase and out of phase components of the magnetic susceptibility. Clear signs of impurities can be seen in all the samples. The broad feature than can be seen around ~150 K for the x=0.2 sample is similar to a feature observed for γ-Fe_2O_3 in AC magnetization measurements [72]. It is possible that these impurities may play a role in the

suppression being so small with Fe doping. However, it should be noted that the amount of impurity phases in the sample is expected to be fairly small because both Raman and XRD measurements failed to detect any signs of impurities while the heat capacity and DC magnetization curves strongly show the features expected for $Ni_3V_2O_8$.
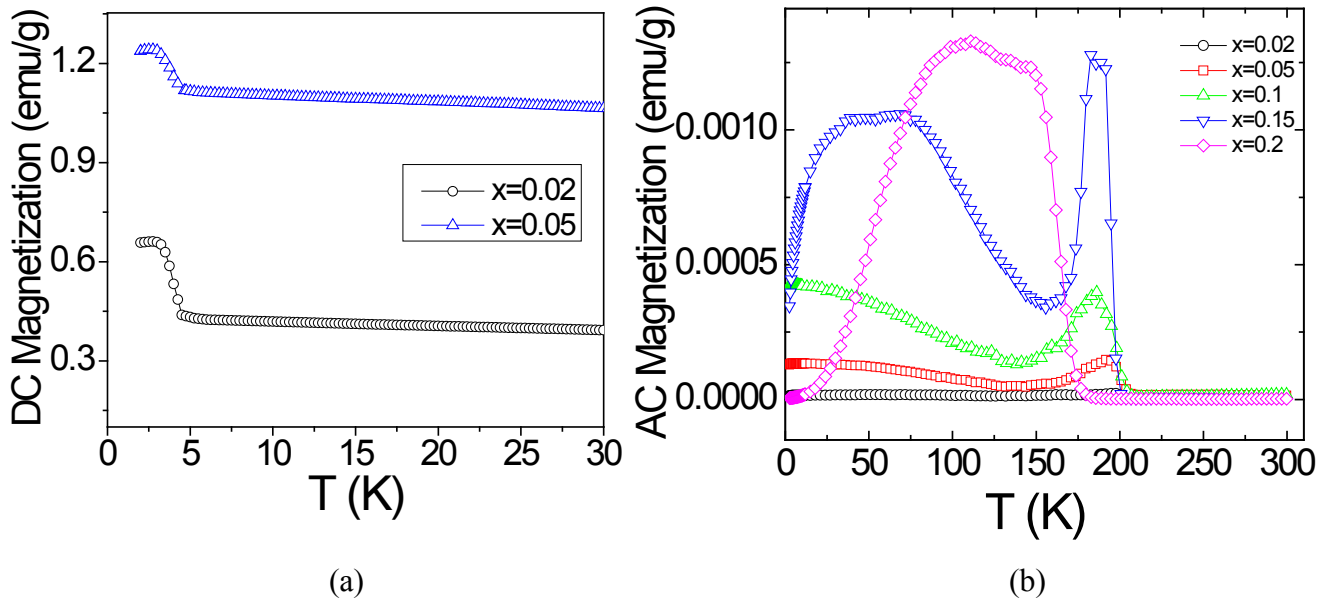
Figure 6.12: $(Fe_xNi_{1-x})_3V_2O_8$ magnetization measurements (a) DC magnetization under 100 Oe (b) AC magnetization under a 10 Oe excitation at 1 kHz

Finally, to explore the behavior with Mn doping, we measured the specific heat capacity of $(Mn_xNi_{1-x})_3V_2O_8$ samples and are presented in figure 6.13. At low doping fractions, the observed behavior is very similar to Fe doping, where the features associated with T_H and T_L remain sharp while the suppression in temperature is small. For $x>0.1$, the peaks become significantly wider and flatter, leading us to believe that the transitions may be strongly suppressed above 10% Mn doping.
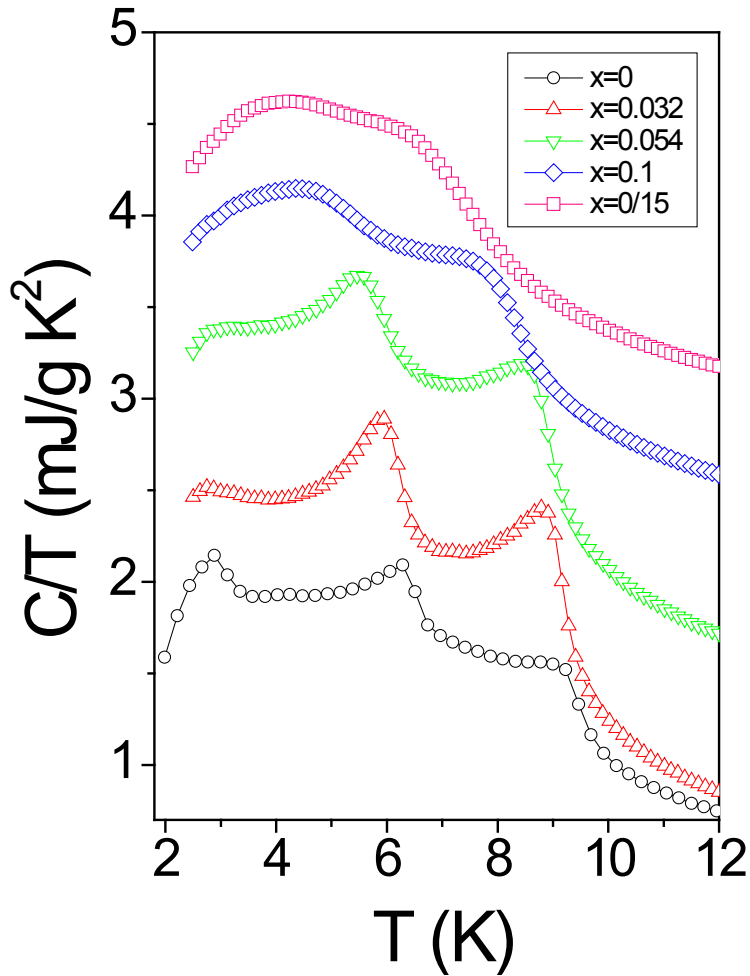
Figure 6.13: $(Mn_xNi_{1-x})_3V_2O_8$ specific heat capacity measurements

We also measured both the DC and AC magnetization for the Mn doped samples to check for any features and also for any possible impurities as with the case with Fe doping. The DC magnetization curve, shown in figure 6.15 shows the 2% sample is paramagnetic as expected above T>10, however the x=0.1 and x=0.15 samples show signs of ordered behavior below T<90 K. The AC magnetization measurements confirm this, where a sharp peak at T~80 K is observed for x=0.1 and x=0.15 samples. This feature however, is not associated with MnO, MnO_2, Mn_2O_3, Mn_3O_4 or $Mn_3V_2O_8$, so it is unclear which impurity phase is responsible. Similar to the case of

Fe doping, it should be noted that the amount of impurity phases in the sample is expected to be fairly small here as well for the same reasons, as both Raman and XRD measurements show no signs of impurities while the heat capacity and DC magnetization curves prominently show the features expected for $Ni_3V_2O_8$.
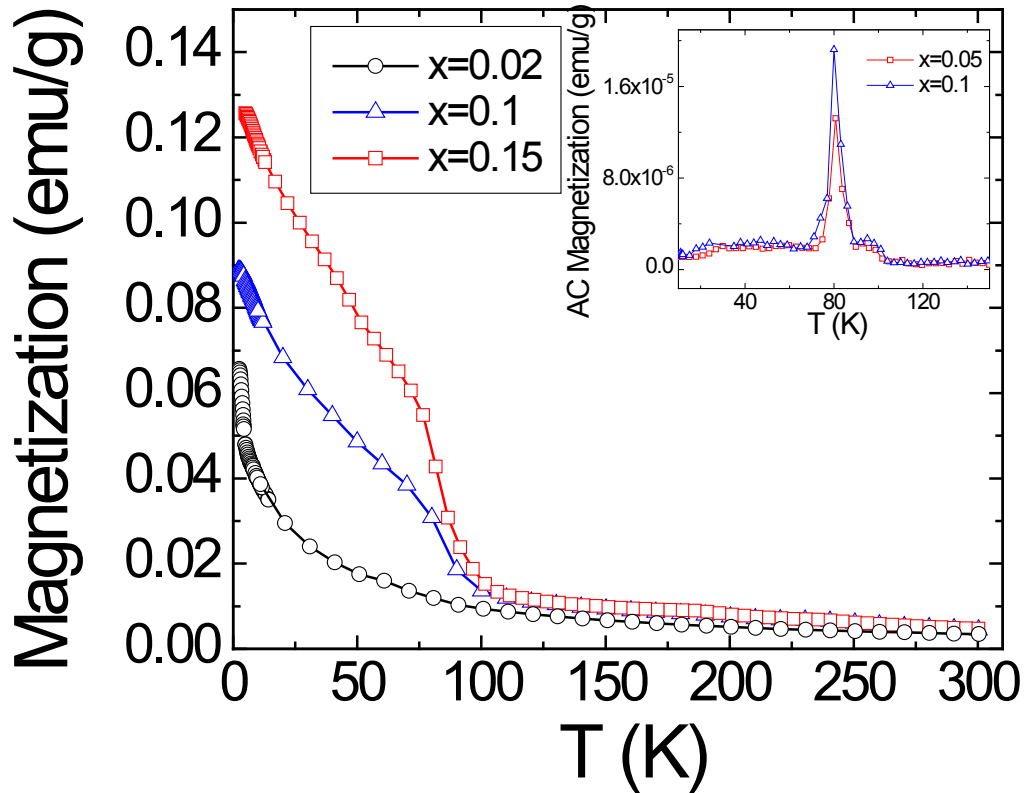
Figure 6.14: $(Mn_xNi_{1-x})_3V_2O_8$ magnetization measurements (a) DC magnetization under 100 Oe (b) AC magnetization under a 10 Oe excitation at 1 kHz

These measurements confirm that the Fe and Mn doped samples are not phase pure and may contain various impurities, although the major part of the sample is expected to be in the correct phase. The solid state reaction method using the oxides as the transition metal source

works well for Cu and Co doped samples, however does not work well for Fe and Mn dopes samples.

Finally, we plotted the T_H and T_L phase transition temperatures together for all the dopants. For T_H, Cu doping shows the highest initial suppression rate, and T_H and T_L combine into a single phase transition above x>0.1. Zn, Mn and Co show qualitatively similar linear suppression lines with Co showing a much smaller slope, while the Zn line is consistent with the suppression rate expected for 2-dimensional Ising spins as discussed in chapter 5. Fe shows an extremely slow suppression rate below x<0.1, however the slope becomes steeper for higher doping fractions.

In the case of T_L, Zn doping shows higher suppression at low temperatures, however. Cu rapidly overtakes Zn as the main suppressor above x>0.05. As discussed earlier, possible reasons for this behavior may be that Cu doping develops a strong non-zero net magnetization in the sample, and the robust nature of the $Cu_3V_2O_8$ lattice. Fe, surprisingly, shows the weakest effect on $Ni_3V_2O_8$ here as well, although the possibility of impurities may also play a role here. Both Zn and Co show fairly linear suppression curves, while $Ni_3V_2O_8$ seems most stable against Co doping with the multiferroic transition persisting up to ~20% doping.
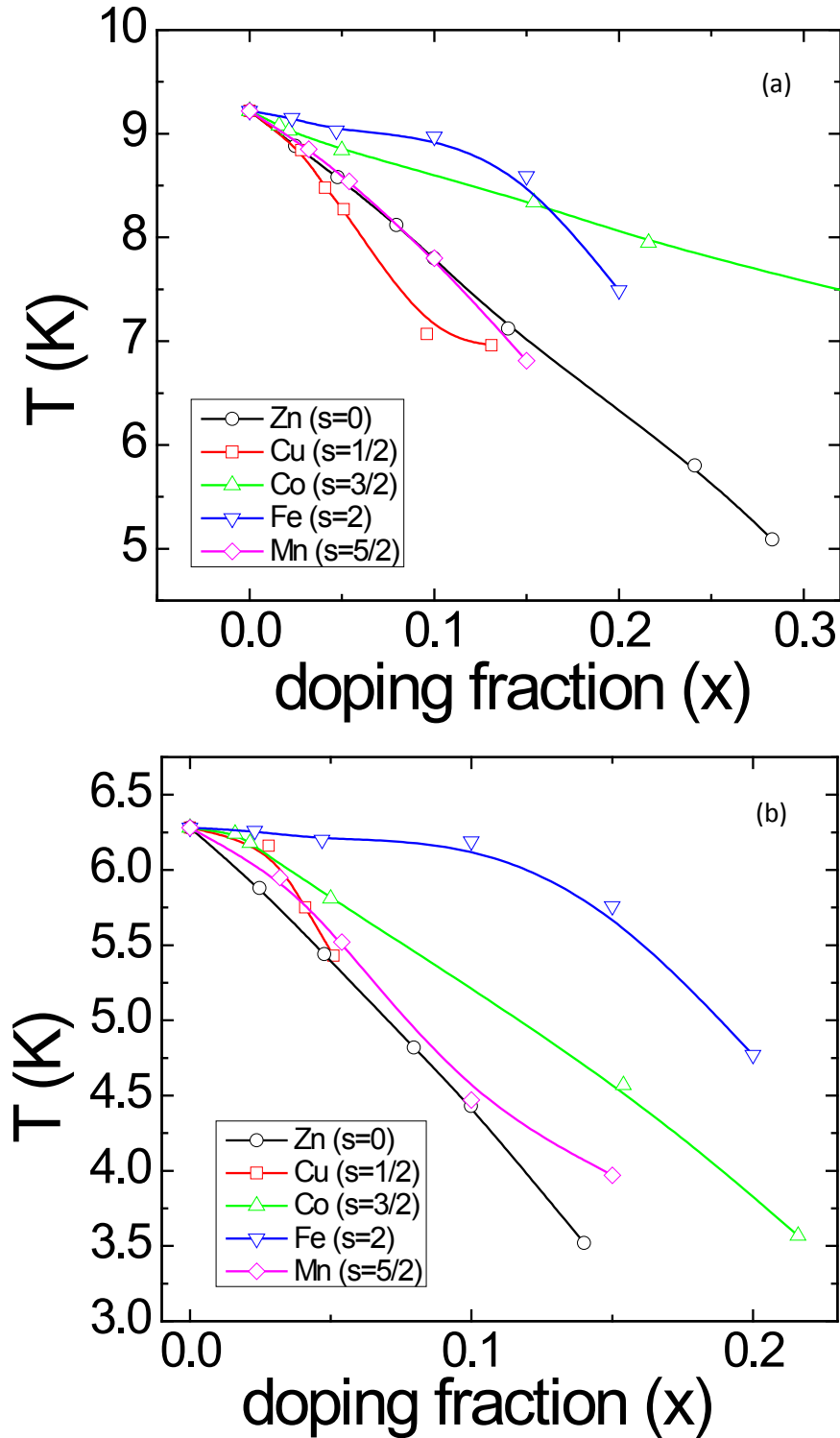
Figure 6.15: $(M_xNi_{1-x})_3V_2O_8$ phase diagrams for (a) Magnetic ordering temperature T_H (b) Multiferroic ordering temperature T_L

As discussed in chapter 5, Zn doping on $Ni_3V_2O_8$ is similar to non-magnetic Zn and Mg doping on multiferroic $FeVO_4$, albeit quantitatively different. The multiferroic phase as well as the magnetic ordering temperatures are found to suppress linearly with the increase of non-magnetic dopant fraction for both materials, while the rate of suppression is higher for $Ni_3V_2O_8$ and is consistent with 2-dimesniosnal site dilution. The smaller rate of suppression for $MnWO_4$ is consistent with the 3-dimensionality of its magnetic lattice. Co doping of $Ni_3V_2O_8$ is consistent with what is observed for $MnWO_4$, where the multiferroic transition persists at 15% Co doping. Cu doping of $Ni_3V_2O_8$ however, shows similar suppression that was observed with Fe doping for $MnWO_4$, where the multiferroic transition was completely destroyed by 5% Fe doping. The qualitative similarity between these two cases is that for $MnWO_4$, the spin 5/2 Mn^{2+} ions were replaced with spin-2 Fe^{2+} ions, while for $Ni_3V_2O_8$, the spin-1 Ni^{2+} ions were replaced with spin-1/2 Cu^{2+} ions. In each case, each magnetic site was diluted by ½ spin, although it is difficult to explain why a ½ spin dilution would be much stronger than a complete removal of the spin as in the case of non-magnetic dopants, or dilution by spin-1 in the case of Co doping of $MnWO_4$. Increasing the spin by 3/2 or 1 or 1/2 for $Ni_3V_2O_8$ (as in the case of Mn, Fe and Co doping respectively) seem to show consistently small effects in suppressing the magnetic transitions as well as the multiferroic ordering of $Ni_3V_2O_8$.

CHAPTER 7

MAGNETIC AND NON-MAGNETIC DOPING OF FeVO$_4$

Doping studies on Ni$_3$V$_2$O$_8$ provided us with intriguing results on how dopants with different spins affects the multiferroic ordering as well as the other phase transitions in a highly symmetric Kagome lattice compound. In this chapter, results from a similar doping study done on FeVO$_4$, which has a magnetic structure very different from Ni$_3$V$_2$O$_8$, will be presented. As discussed in chapter 4, FeVO$_4$ is a recently discovered multiferroic material which has a low symmetry magnetic structure with 3 different Fe^{3+} sites, with Fe^{3+} being the only magnetic ion in the material. FeVO$_4$ undergoes two antiferromagnetic transitions at low temperatures with a Neel temperature T_{N1} of 21 K and a second phase transition at T_{N2} ~15 K which is known to be multiferroic [7]. In the first phase FeVO$_4$ forms a collinear incommensurate structure while the low temperature phase has a non-collinear incommensurate structure.

The direction of the polarization in FeVO$_4$ depends on details of the microscopic magnetoelectric interaction as a result of its low symmetry [22] and thus information on these interactions can be more readily available through a doping study. We chose Zn as the first dopant as non-magnetic doping would be the easiest to analyze as is the case with Ni$_3$V$_2$O$_8$, followed by Cr and Mn ions, which readily forms 3+ ions and has roughly the same size as the Fe^{3+} ion they are expected to replace, and thus it is expected they would fit into the lattice. By replacing the magnetic Fe^{3+}(s=5/2) ions with dopants Zn^{2+} (s=0), Cr^{3+} (s=3/2), and Mn^{3+} (s=2), we expect see how the two phase transitions and the multiferroic phase are affected by dopants,

and to address the question of how the magnetic interactions among the Fe^{3+} spins produce multiferroic order.

As we were limited by previously discussed complications with the dielectric probe, we used magnetization measurements as an initial measurement followed by heat capacity measurements, which gave us the ability to track the phase transition temperatures. Finally, we carried out polarization measurements to confirm the ferroelectric nature of the samples.

As a first step, we performed magnetization measurements on these ceramic $Zn_xFe_{1-x}VO_4$ samples to track the changes in transition temperatures. Figure 7.1 shows the magnetization as a function of the temperature for the full range of 5 K – 300 K for Zn doped samples while the insert zooms in on the low temperature range. The samples show typical paramagnetic behavior at high temperatures with the ordering temperature T_{N1}~ 21 K clearly indicated by a sharp peak in all the doped samples. T_{N2}~15 K is shows up as a smaller anomaly which is consistent with the expected antiferromagnetic transition and previously observed magnetization curves for undoped $FeVO_4$ [8]. It is immediately clear that both magnetic transitions persist even with 20% doping of Zn, and very little suppression in transition temperature is observed. This indicates that the magnetic ordering, and the microscopic interactions responsible for magnetic ordering in $FeVO_4$ is very robust against non-magnetic doping.
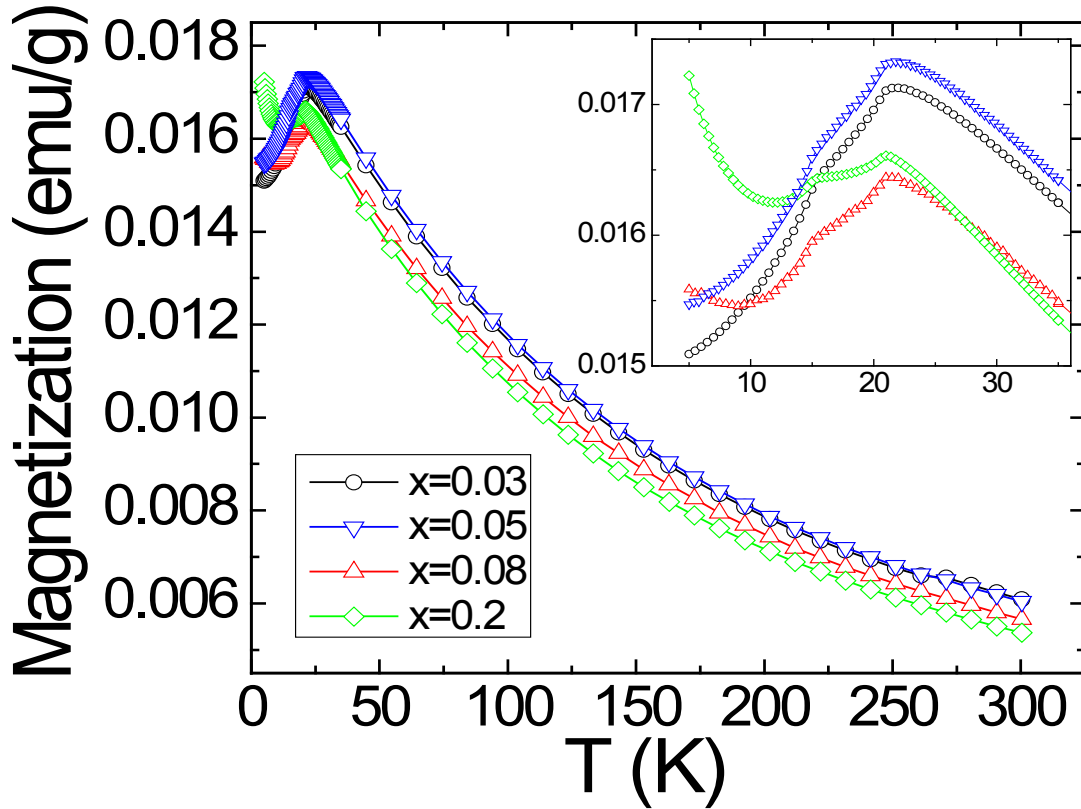
Figure 7.1: Magnetization measurements for $Zn_xFe_{1-x}VO_4$ over the entire temperature range, insert: magnetization curve at low temperatures showing the features

To investigate how the magnetic ordering in $FeVO_4$ are affected by magnetic dopants, we measured the magnetization measurements for spin-3/2 Cr^{3+} and spin-2 Mn^{3+} doped samples, and are shown in figure 7.2. These magnetization curves are very similar to the Zn doped samples, and the $T_{N2} \sim 15$ K transition appears as a small feature while the magnetic ordering temperature $T_{N1} \sim 21$ K is discerned by a sharp peak for all Cr and Mn doped samples. The behavior above the ordering temperature remains clearly paramagnetic (not shown) with the inverse susceptibility curve exhibiting linear behavior.
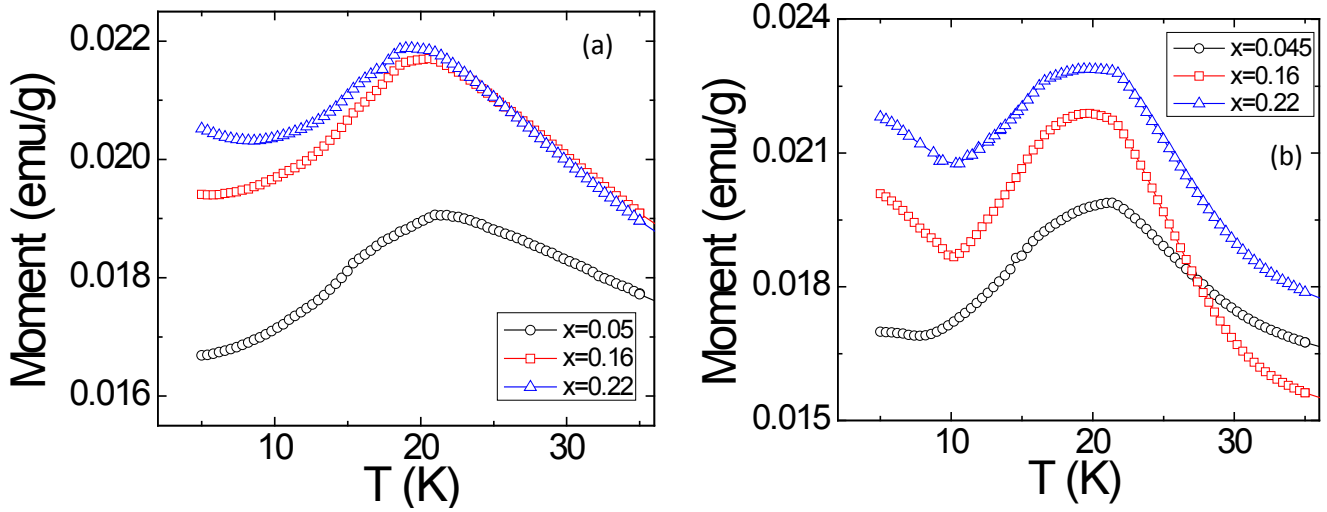
Figure 7.2: Low temperature magnetization measurements for $M_xFe_{1-x}VO_4$ for (a) M = Mn (b) M = Cr

We take the high temperature magnetization data (between 50 K and 300 K) and plot these in units of mole / Oe emu against the temperature (Figure 7.3). These curves are linear over the temperature range agreeing with the expected purely paramagnetic behavior at high temperatures. The effective moment pre transition metal ion in units of Bohr magnetons can be calculated using the Curie Weiss lax $\chi = C/(T - T_\theta)$, where $C = Ng^2\mu_B^2J(J + 1)/3k_B$ is the Curie constant and T_θ the Weiss temperature. Similar to the case of $Ni_3V_2O_8$, due to the orbital quenching in transition metal oxides, the spin-only value (J=S) agree better with the measured values.

We find the effective moments, per transition metal ion, to be 5.81 μ_B, 5.82 μ_B, and 5.85 μ_B for $FeVO_4$ doped with Zn, Cr and Mn, respectively. This is consistent with the expected effective moment of undoped $FeVO_4$, 5.9 μ_B, as a small decrease is expected when higher spin

Fe^{3+}(s=5/2) in removed from the lattice and is being replaced with lower spin Zn^{2+}(s=0), Cr^{3+}(s=3/2) and Mn^{3+}(s=2). The Curie-Weiss temperature (θ_{CW}) shows a larger change compared with undoped $FeVO_4$ for which θ_{CW} = -126 K, and are -111 K, -108K and -104 K for 5% Zn, Cr and Mn doped samples respectively. When the doping fraction is increased to 20%, we observe a larger change in the effective moment as well as the Curie-Weiss temperature, consistent with more Fe^{3+} ions being replaced with lower spin dopants. The effective moments derived from the curves are 5.44 μ_B, 5.5 μ_B, and 5.63 μ_B, and the Curie-Weiss temperatures -102 K, -93 K and -92 K for samples doped with 20% Zn, Cr and Mn respectively.
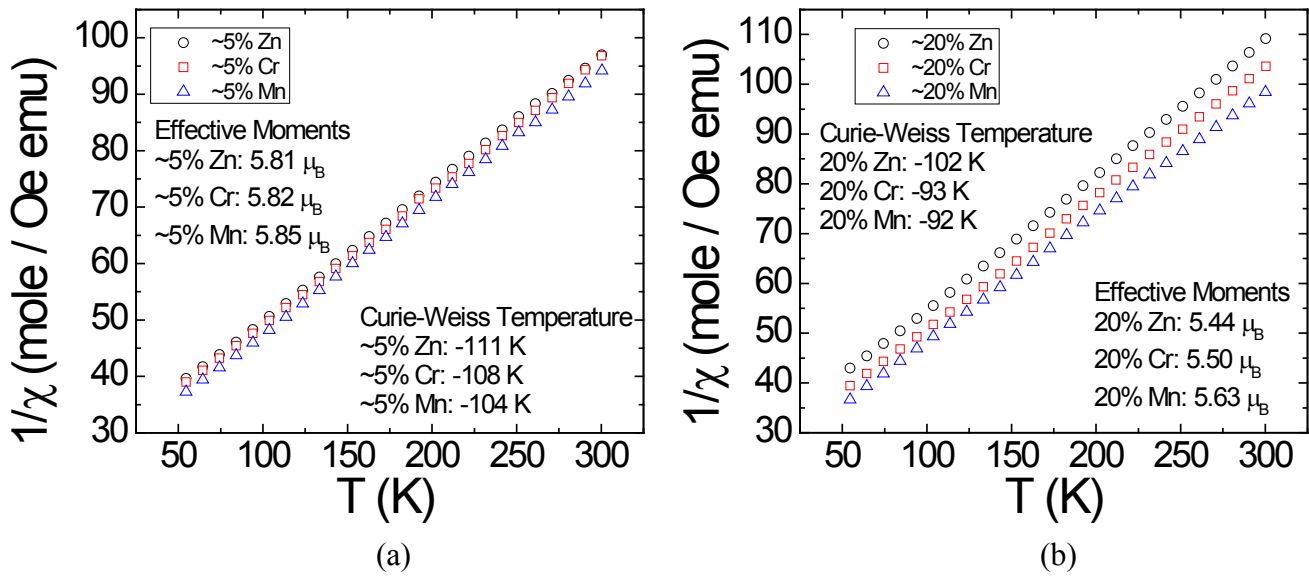
Figure 7.3: $1/\chi$ plots over the temperature range of 50 K – 300 K for (a) 5% TM doped samples (b) 20% TM doped samples

Since the onset of the multiferroic transition T_{N2} with the change of doping fraction was difficult to observe purely from magnetic measurements, we measure the heat capacity of this set

of samples over the entire composition range. In order to carry out heat capacity measurements, we mix the $Fe_{1-x}M_xVO_4$ powder with Ag powder at 1:1 mass ratio to increase the thermal conductivity and improve the integrity of the pellet, and later correct for the contribution from the Ag fraction to the heat capacity. Figure 7.4 shows the heat capacity curves obtained for all 3 dopants plotted together with undoped $FeVO_4$ in the range of 10 K – 30 K. The curves have been shifted in the vertical direction for clarity. Both T_{N1} and T_{N2} can be seen clearly by peaks in corresponding positions in the heat capacity measurements. The peaks observed for undoped $FeVO_4$ are consistent with previous studies [8], and the doped samples show a very small suppression in transition temperatures in the case of Zn and Mn, and increase in temperature slightly for Cr doping. The peak intensity as well as peak width shows no significant change with the increase of doping fraction.
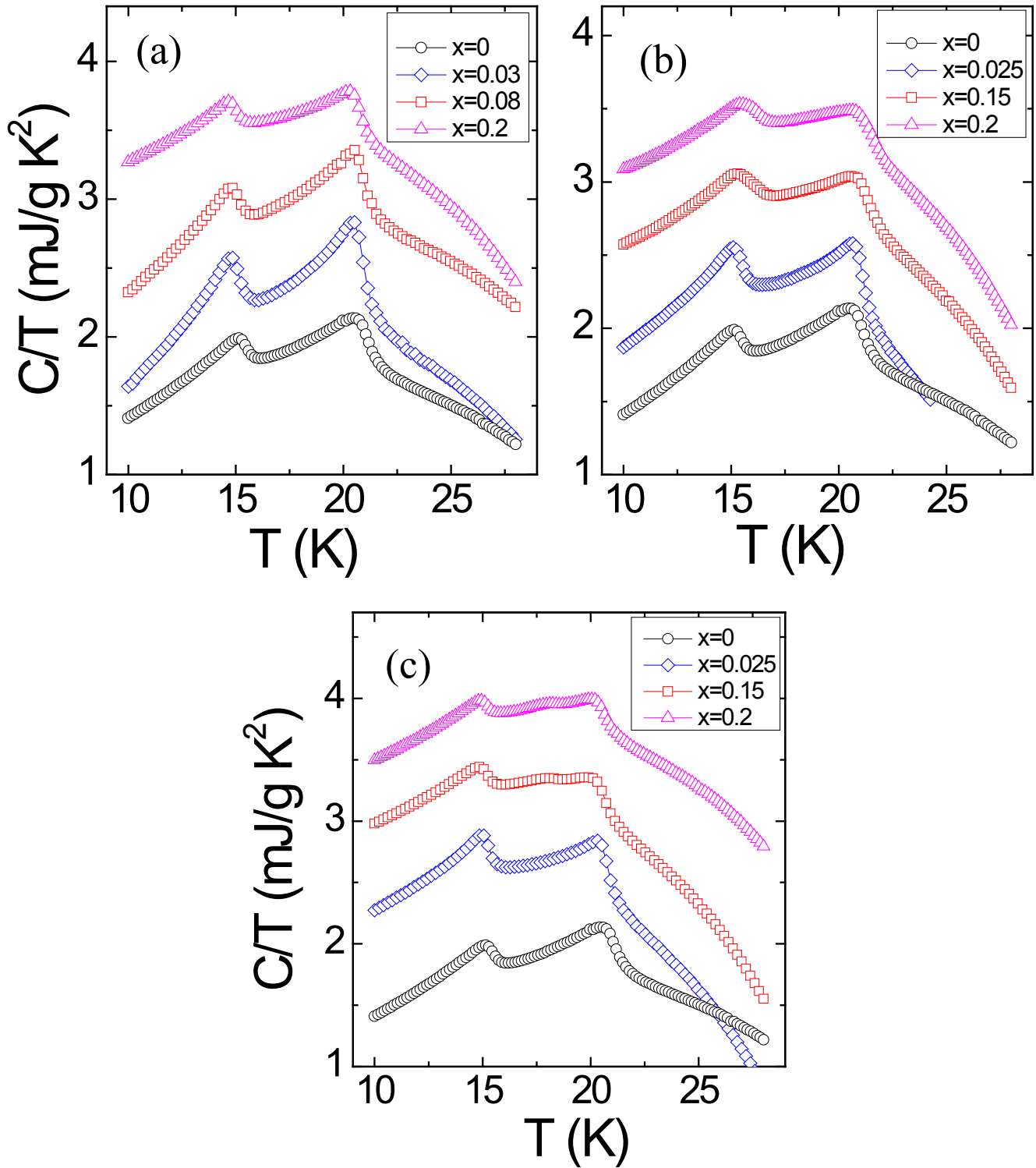
Figure 7.4: Heat Capacity measurements for $M_xFe_{1-x}VO_4$ plotted together with pure $FeVO_4$ for (a) M = Zn (b) M = Cr and (c) M = Mn

In order to confirm that these magnetic and thermodynamic signatures mark the onset of ferroelectric order, we measured the ferroelectric polarization for some of the samples. The polarization was calculated similar to the previous cases; the samples were cooled down past the transition temperature in a high poling field (+/-200 V), and the pyrocurrent was measured while warming up, which was finally integrated over time to obtain the ferroelectric polarization after drift current and noise was removed.
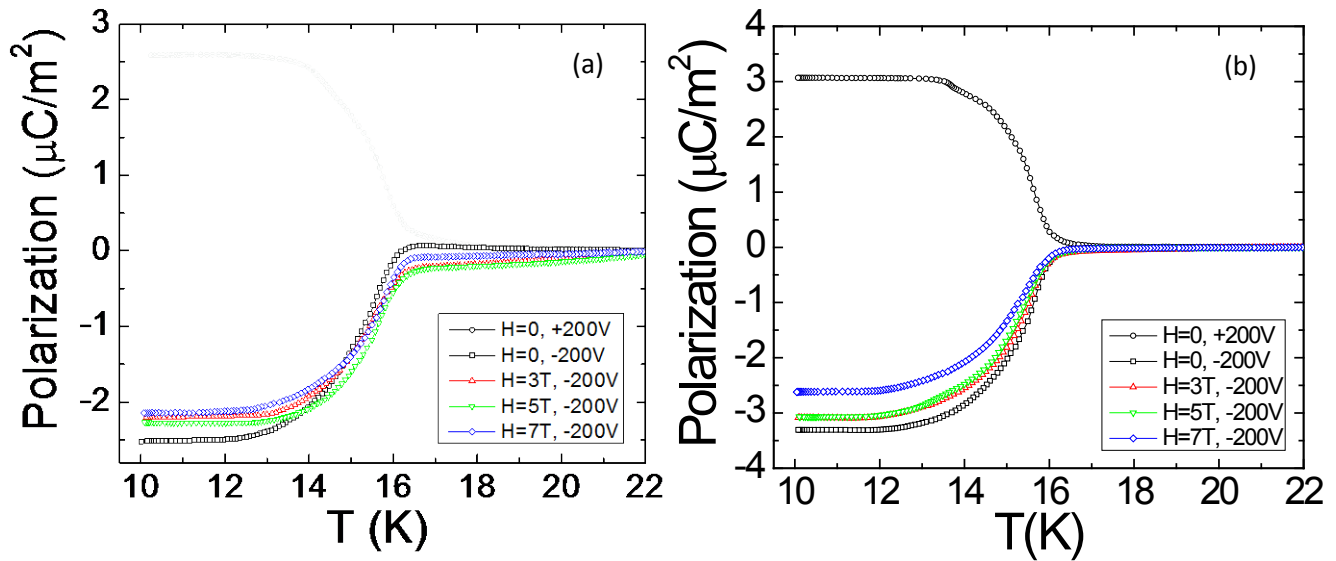
Figure 7.5: Ferroelectric Polarization measurements for $M_{0.05}Fe_{0.95}VO_4$ (a) M = Zn (b) M = Cr

Fig 7.5 (a) and (b) shows the ferroelectric polarization of 5% Cr and Mn doped $FeVO_4$ samples respectively, measured under different applied fields. The magnitudes of polarization for the 5% doped samples are 2.6 and 3.1 $\mu C\ m^{-2}$ for Cr and Mn doped samples respectively, and is electrically reversible by switching the direction of the applied field. This value is somewhat smaller than the previously reported ~6 $\mu C\ m^{-2}$ for pure $FeVO_4$ [8]. This can be attributed to the suppression of ferroelectricity when doped with Cr and Mn ions. In addition, inhomogeneity effects in the ceramic samples, a fairly large drift current, which can suppress the height of the

pyrocurrent peak, as well as geometric effects of the samples and contacts may attribute to the uncertainty of the magnitude of the signal. It should be noted that due to these reasons, the magnitudes of the polarization should not be directly taken quantitatively for comparison between the samples, but should merely act as evidence that the samples are indeed ferroelectric. The polarization measured under different applied fields (H = 3, 5 and 7 T) are somewhat smaller for all samples than when measured under zero field, but the difference is very small.
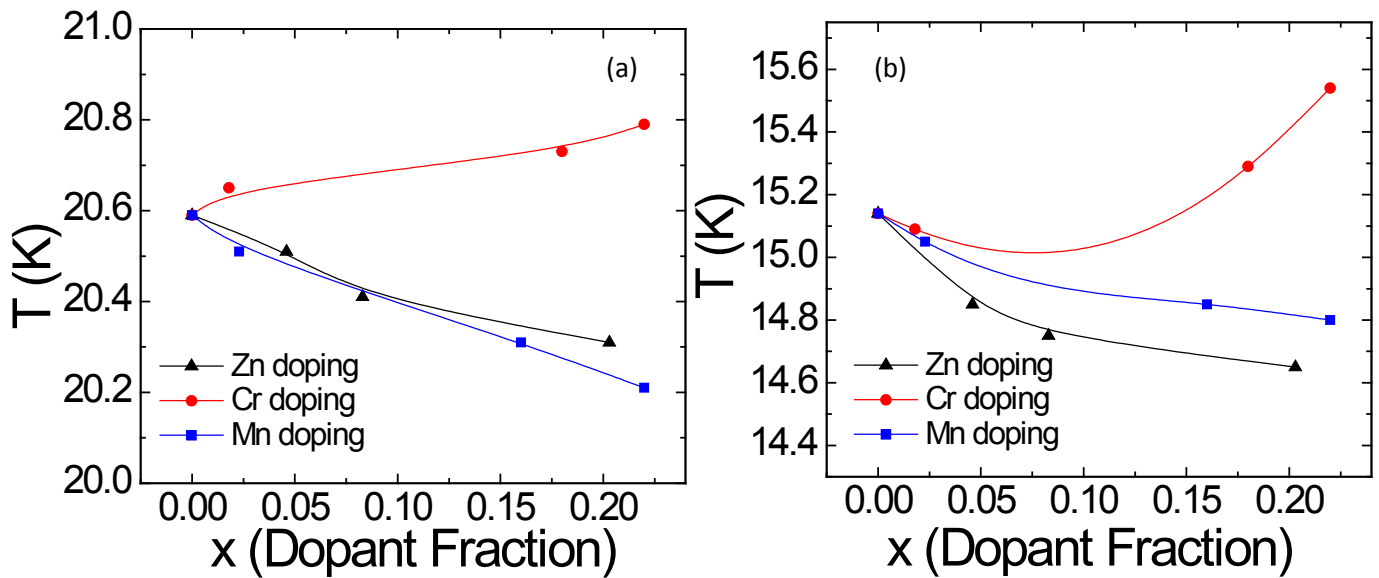
Figure 7.6: Phase diagrams for TM doped FeVO$_4$ (a) Change in T$_{N1}$ with doping (b) change in T$_{N2}$ with doping

To get a better perspective of how the phase transitions are suppressed, we extracted peak positions from the heat capacity measurements as they show the most prominent peaks, and plotted the peak position as a function of dopant fraction to obtain phase diagrams for M$_x$Fe$_{1-x}$VO$_4$ for both T$_{N1}$, the ordering temperature (figure 7.6-a) and T$_{N2}$, the multiferroic transition temperature (figure 7.6-b). The suppression of T$_{N1}$ for Zn and Mn doping is only ~2% at 20%

doping, while T_{N2} shows only 3.2% for Mn and 2.2% for Cr at 20% doping. On Cr doping, T_{N1} shows an increase of ~1% and T_{N2} shows an increase of 2.6% by 20% doping. All these are remarkably small numbers, when compared with previously observed results for $Ni_3V_2O_8$ such as Zn doped $Ni_3V_2O_8$ which shows a 30% suppression of the ordering temperature and a 55% suppression of the multiferroic transition temperature.

Although not wholly satisfactory, one possible explanation for this extremely low suppression is the low symmetry magnetic structure of $FeVO_4$. When a material has a highly symmetric magnetic structure, replacing some of the magnetic ions with a dopant can be expected to more significantly affect the magnetic interactions in the material that is responsible for ferroelectric ordering, as we observed with Cu doped $Ni_3V_2O_8$. However, when the magnetic structure has low symmetry as in $FeVO_4$ with 3 unique Fe^{3+} sites, it may become possible that the effect of a dopant is weaker.

In summary, the dopants Zn, Cr and Mn only minimally affects the multiferroic ordering as well as the magnetic ordering temperature of $FeVO_4$. This provides an excellent opportunity to use very high dopant fractions to tune the multiferroic properties of $FeVO_4$.

CHAPTER 8

SUMMARY AND FUTURE WORK

We have presented results describing how non-magnetic (Zn^{2+}) doping and magnetic doping with dopants of different spins (spin-1/2 Cu^{2+}, spin 3/2 Co^{2+}, spin-2 Fe^{2+}, and spin-5/2 Mn^{2+}) of $Ni_3V_2O_8$ as well as non-magnetic (Zn^{2+}) and magnetic (spin-3/2 Cr^{3+}, and spin-2 Fe^{3+}) of $FeVO_4$ affects their magnetic phase transitions as well as the multiferroic ordering. In the case of non-magnetic Zn doping, we observed the magnetic ordering temperature T_H and he multiferroic phase transition temperature T_L is suppressed linearly in temperature with the increase of dopant fraction. The normalized suppression rate calculated for T_H is 1.6, which agrees very well with the expected value for Ising spins which is 1.6 - 1.9. This confirmed the HTI phase has a 2-D Ising like spin structure through this doping study, which confirmed observations from previous neutron scattering studies.

The suppression rate for T_L, 2.9, agrees well with the expected values of Heisenberg spins which is ~3. This confirms that the LTI phase predominantly exhibits a 2-D Heisenberg spin structure which also agrees well with previous neutron studies. We observed that the magnetic ordering phase transition at T_H clearly persists at 30% Zn doping, while the TH transition also persists up to this fraction, and remains multiferroic at least up to 15% doping. Considering the delicate balance of competing magnetic interactions and the phase competition in $Ni_3V_2O_8$, this was a surprising result. However, similar results have been observed in another complex multiferroic system since then; $MnWO_4$ has been found to be extremely robust against non-

magnetic dopants with similar linear phase transition suppression lines. $MnWO_4$ however, shows a much smaller rate of suppression as compared with $Ni_3V_2O_8$, highlighting the difference of the dimensionality of spin structures between these two materials; the faster suppression in $Ni_3V_2O_8$ is consistent with site dilution in a 2-dimensional spin system, while the relatively small suppression rate in $MnWO_4$ is a result of the 3-dimensional character of the magnetic interactions in $MnWO_4$.

In contrast, Cu doping on $Ni_3V_2O_8$ suppressed both T_H and T_L strongly. The multiferroic behavior is completely suppressed by 10% doping, while above $x>0.13$ only a single clear phase transition persists. However, below the $x < 0.1$ range, there is a sharp increase of net magnetization in the system, enabling the possibility of having a net magnetization and a sizable ferroelectric polarization simultaneously with fairly strong magnetoelectric coupling, which is a very exciting result for device development. There are several possibilities for this strong suppression due to Cu doping, one being the development of this net ferromagnetic moment itself. Another possibility is that $Cu_3V_2O_8$ has a much stronger magnetic structure than $Ni_3V_2O_8$.

Conversely, $Co_3V_2O_8$ seem to have a much weaker magnetic structure as compared with $Ni_3V_2O_8$, as observed from Co doping results. $Ni_3V_2O_8$ type magnetic transitions are observed up to ~80% Co fractions, with the multiferroic phase persistent at least to $x\sim0.2$ doping fraction. This concurrently means that $Co_3V_2O_8$ is extremely sensitive to Ni doping. This is somewhat similar to results observed for Co doped $MnWO_4$, where the multiferroic transition persisted up to 15% doping. Higher spins such as Fe and Mn seem to have a similar effect on $Ni_3V_2O_8$, with the suppression rates being fairly low and both T_H and T_L transitions observed up to 30% doping. However, higher doped Fe and Mn samples are not phase pure.

It would be very interesting to study the magnetic lattice of some of these doped samples with neutron scattering. The Kagome magnetic lattice of $Ni_3V_2O_8$ has 2 inequivalent Ni^{2+} sites, and it was generally assumed the dopant spins has no site preference and would sit at these two different positions homogeneously. However, especially at higher doping fractions, it is possible that some dopants may prefer a particular type of Ni^{2+} site. Because the spine Ni^{2+} sites contribute mostly to the magnetic ordering in the HTI phase, and both spine and cross tie spins contribute to the magnetic structure in the LTI phase, if a dopant has a preference for cross tie sites, it may not have as much an effect on the HTI phase as a dopant which prefers the spine sites. Neutron scattering would provide the details of the magnetic lattice and would show if a dopant has an inhomogeneous distribution among the different Ni^{2+} sites.

We have also presented initial doping studies, both non-magnetic (Zn) and magnetic (Cr and Mn) on a recently discovered multiferroic, $FeVO_4$. The direction of ferroelectric polarization in $FeVO_4$ depends on the magnetic lattice as well as details of the microscopic magnetoelectric interaction as a result of its low symmetry, and thus information on these interactions can be more readily available through a doping study. We found that the magnetic transition temperatures as well as the multiferroic ordering in $FeVO_4$ are remarkably robust against all 3 dopants. The suppression of T_{N1} for Zn and Mn doping is only ~2% at 20% doping, while T_{N2} shows only 3.2% for Mn and 2.2% for Cr at 20% doping. On Cr doping, T_{N1} even shows a small increase. All these are remarkably small numbers, when compared with previously observed results for $Ni_3V_2O_8$ such as Zn doped $Ni_3V_2O_8$ which shows a 30% suppression of the ordering temperature and a 55% suppression of the multiferroic transition temperature. A possible explanation for this extremely low suppression is the low symmetry magnetic structure of $FeVO_4$ which may suppress the effect of a dopant on the magnetic ordering.

We have completed a systematic transition metal doping study on $Ni_3V_2O_8$ and laid the groundwork for systematic doping study in $FeVO_4$. It would be extremely interesting to see how other transition metal dopants such as Cu, Co and Ni affect the magnetic ordering temperatures and the multiferroic ordering in $FeVO_4$. It would also be very interesting to see how rare earth metals like Sc, Gd, etc. would affect the magnetic properties of both $Ni_3V_2O_8$ and $FeVO_4$. We have successfully synthesized Gd doped $FeVO_4$ for small doping fractions, and initial results (not presented in this thesis) show similarly strong robustness for $FeVO_4$ against Gd doping. However, this behavior may rapidly change at higher doping fractions; as rare earth metals have much larger diameters, they may possibly also introduce lattice distortions in the magnetic lattice, which may lead to more complex behavior.

In summary, we have demonstrated that the two multiferroic oxides, $Ni_3V_2O_8$ and $FeVO_4$ are in general extremely robust against perturbations provided by both non-magnetic and magnetic dopants. It is possible that other multiferroic systems, or in general, other multifunctional oxides may also have similar properties and will be resilient to high doping fractions. This will provide an excellent opportunity to tune the properties of these materials because high doping concentrations can be used.

APPENDIX A

ANNEALING EFFECTS ON MAGNETIC

PROPERTIES OF Gd$_2$O$_3$ NANOPARTICLES

Results of Gd$_2$O$_3$ nanoparticle work studying how the post-preparation annealing treatment and in turn, the crystallinity, of the Gd$_2$O$_3$ nanoparticles affect their magnetic properties are presented in this appendix. Gd$_2$O$_3$ nanoparticles having a diameter of approximately 25 nm were synthesized using a co-precipitation technique. These nanoparticles were then heated at different temperatures to explore the effects of annealing conditions on their magnetic characteristics. We found that a minimum temperature of 600 ^{o}C is required to crystallize the nanoparticles in a cubic structure, and the degree of crystallinity increases with annealing temperature up to 1000 ^{o}C. The magnetic moment increases with annealing temperature, and a small hysteresis also develops.

Multifunctional magnetic nanoparticles have attracted a great deal of attention recently as they have great potential to be used for various medical applications. These include medical diagnostics and treatment, and biomedical imaging, especially Magnetic Resonance Imaging (MRI). MRI is a powerful non-invasive imagining technique that can provide excellent spatial resolution and soft tissue contrast with no radiation exposure to the patient. MRI obtains contrast in the images using different properties of human tissues such as difference in proton densities and proton relaxation times. The spin of the proton precesses about an externally applied magnetic field at this Larmor frequency given by $\omega_0 = \gamma B_0$ where γ is the gyromagnetic ratio of

the proton. Larmor frequency depends on the applied field, so if a spatially varying field is applied across a sample would produce spatially varying frequency components given by $\omega(\mathbf{x}) = \gamma B(\mathbf{x})$. Lauterbur and Mansfield showed in 1973 that these different frequency components can be deconvoluted to obtain spatial information about the sample.
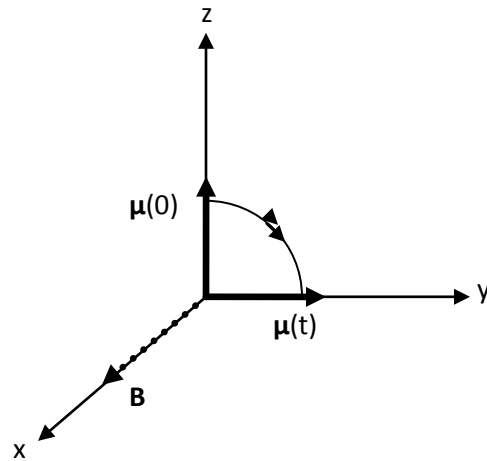
Figure A.1: Effect of an external field on a proton

If the spins are initially pointing along the z direction as shown in figure A.1, a magnetic pulse (usually referred to as a radiofrequency or RF pulse) applied along the x direction is used to flip the spins in y direction. This creates a transverse magnetization along y direction, which will decay with time when the RF pulse is removed. Thus, the spin along z direction will increase with time after the RF pulse as initial moment recovers. The characteristic time T_1 describes the recovery of the magnetization along the z direction, and is defined by equation A.1 [73].

$$M_z(t) = M_0 \, (1 - e^{-t/T1}) \qquad\qquad (A.1)$$

T_1 depends on the interaction of spins with their local environment and is different for different materials. This concept can be used to obtain contrast in a MR image in a method known as T_1 weighted imaging. This technique uses the difference in T_1 relaxation times to identify different local environments in the sample. However, other relaxation effects can also alter the signal. These include the T_2 relaxation time, which parameterizes the dephasing time of spins in the x-y plane from the original y direction due to spin-spin interactions

Based on the two preliminary relaxation times; longitudinal relaxation time (T_1), and transverse relaxation time (T_2), two common MRI techniques exist; T_1-weighted and T_2-weighted imaging. Here the variable image contrast is obtained from the difference in relaxation times in the tissues, and contrast agents can induce extra proton spin relaxation in the relevant tissues, providing better contrast in the image. Any contrast agent would in general affect both T_1 and T_2, but depending on which relaxation time is affected to a greater degree, the agent will be categorized as a T_1 or T_2 agent. Since magnetic nanoparticles can be successfully used to modify the relaxation times, MRI has benefited greatly from the introduction of magnetic nanoparticles as contrast enhancing agents [74,75].

The most widely used contrast agents in current use are based on Gd^{3+}, as this ion has a large magnetic moment with 7 unpaired electrons. However, due to the toxicity of metallic Gd, these are used in the form of ionic complexes with chelating ligands [74, 75, 76]. Gd^{3+} is preferred over other lanthanides with larger moments (eg. Dy^{3+} and Ho^{3+}) because the symmetric S-state produces a slower relaxation rate in the surrounding water molecules. Paramagnetic Gd chelates are T_1 based agents that predominantly lower the longitudinal relaxation time, increasing the signal intensity. Conversely, another emerging contrast agent, superparamagnetic

Iron Oxide (SPIO) [77, 78] are often used as a negative contrast agent that shorten the T_2 relaxation time. Using an agent in nanoparticle form is especially attractive because the fraction of surface atoms is very high in nanoparticles as compared with bulk. Gd_2O_3 nanoparticles can provide a large number of magnetic ions per unit volume compared with Gd chelates [79], which is important for obtaining both a high contrast and a large signal.

Gd_2O_3 nanoparticles have shown great promise as a MRI contrast agent because of their ability to provide good image contrast and a high signal to noise ratio [79, 80, 81]. Oxidation also reduces the difficulties associated with handling the material, as bare Gd nanoparticles are extremely reactive. Gd_2O_3 nanoparticles have shown a considerable increase in relaxivity compared with Gd-DTPA, the most common Gd^{3+} chelates in use. A study by Engstrom *et. al.* finds that both T_1 and T_2 relaxivities in the presence of dextran coated Gd_2O_3 particles were approximately twice as large as the corresponding values for Gd–DTPA in aqueous solutions [82]. Gd_2O_3 in nanoparticle form is especially attractive for cell labeling studies and molecular targeting studies combined with magnetic imaging. Currently, SPIO is often used for these cell labeling studies, which carries the inherent disadvantage of providing lesser contrast as SPIO is a negative agent. Klasson *et. al.* [83] finds that dextran coated Gd_2O_3 nanoparticles have the potential to be used as a tissue specific contrast agent, and will provide strong signal intensity at relatively low concentrations. Fortin *et. al.* finds that capping the nanoparticles with polyethylene glycol will enhance the relaxivity and increase the signal intensity even further [79], as compared with dextran coated nanoparticles. A recent study confirms that diethylene glycol-Gd_2O_3 nanoparticles provide much higher relaxivities, where r_1 and r_2 relaxivities increase approximately 4 times as compared to the corresponding values of Gd-DTPA [84].

Although considerable research has been directed towards characterizing the effectiveness of Gd_2O_3 nanoparticles as an MRI contrast agent, there remains less understanding of how the crystallinity of the nanoparticles affects the overall performance of Gd_2O_3 as a contrast agent and their magnetic properties. In this study, we expect to lay the groundwork to address these two issues. We synthesize and anneal Gd_2O_3 nanoparticles at various temperatures, and explore the effect of annealing conditions on the magnetic characteristics of Gd_2O_3 nanoparticles, as well as conduct some preliminary relaxation studies.

A.1 Synthesis
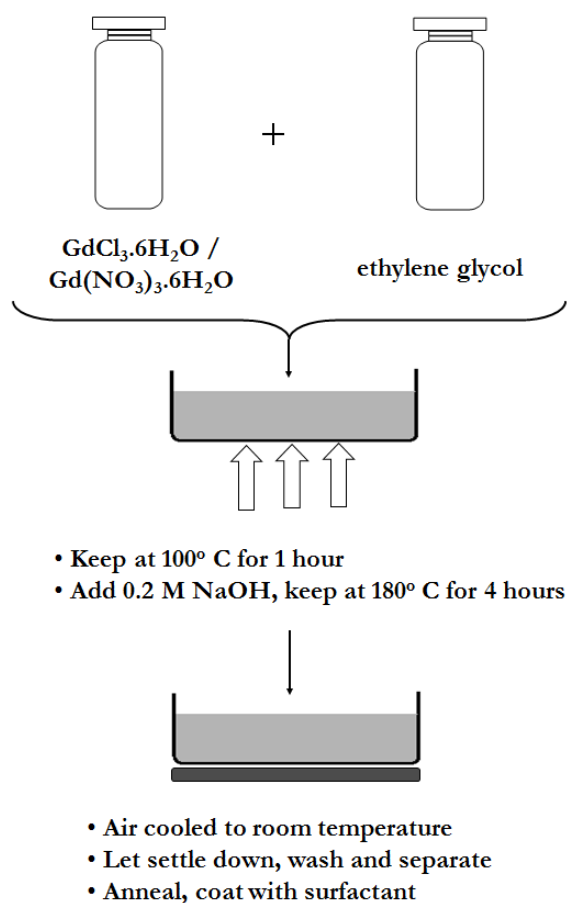
Figure A.2: Synthesis technique for Gd_2O_3 nanoparticles

Gd$_2$O$_3$ nanoparticles were synthesized using a co-precipitation technique similar to previous approaches [79], as shown in figure A.2. Gd(NO$_3$)$_3$.6H$_2$O 99.9% purity (Alfa Aesar catalog# 12917) was used as the Gd(III) source which was dissolved in diethylene glycol to prepare a 0.2 molar Gd(III) solution. This was heated to 120 ^{o}C until the Gd(NO$_3$)$_3$ was completely dissolved, and then 0.2 molar NaOH was added dropwise and the temperature raised to 180 ^{o}C, while stirring continuously. At this temperature Gd$_2$O$_3$ nanoparticles begin to precipitate out of solution. After letting the solution cool down to room temperature, the nanoparticles were allowed to settle down at the bottom of the container and removed. These were then washed several times with deionized water and allowed to dry. An oil bath was used throughout the synthesis to keep the temperatures stable. After synthesis, the nanoparticles were annealed at temperatures ranging from 400 ^{o}C to 1000 ^{o}C in air in order to improve the crystallinity of the nanoparticles. To reduce the toxicity of the nanoparticles and to increase the suspension in aqueous solutions, a coating of dextran was applied to the outside of the nanoparticles, following an approach previously used to coat iron oxide nanoparticles [78]. However, annealed nanoparticles developed agglomeration and suspending the nanoparticles in solution proved difficult which could affect the relaxation properties of these nanoparticles as discussed later.

A.2 Characterization and Magnetic Measurements

X-ray diffraction (XRD) studies were conducted using a Rigaku RU2000 powder diffractometer. Figure A.3 shows the XRD patterns obtained for the as-prepared sample compared with samples annealed at 400 ^{o}C, 600 ^{o}C, 800 ^{o}C and 1000 ^{o}C. We find that the as-prepared nanoparticles are amorphous, with a temperature of at least 600 ^{o}C being required to

crystallize the Gd_2O_3 nanoparticles in the expected cubic structure. The sharpness of the XRD peaks, reflecting the crystallinity, improves markedly with annealing temperature. As an example, if the most intense peak (which originates from the 222 plane) of the spectrum is considered, the full widths at half maximum are 0.49, 0.31 and 0.22 for samples annealed at 600, 800 and 1000 $^{\circ}$C respectively. This is consistent with a previous study [85], which finds amorphous Eu doped Gd_2O_3 nanoparticles crystallizing into a cubic structure at temperatures starting from 325 $^{\circ}$C and becoming well crystallized at 800 $^{\circ}$C. This is also consistent with many studies on thin film Gd_2O_3 where a temperature of 600 $^{\circ}$C to 700 $^{\circ}$C was required to start crystallizing the film in cubic gadolinium structure [86, 87, 88].
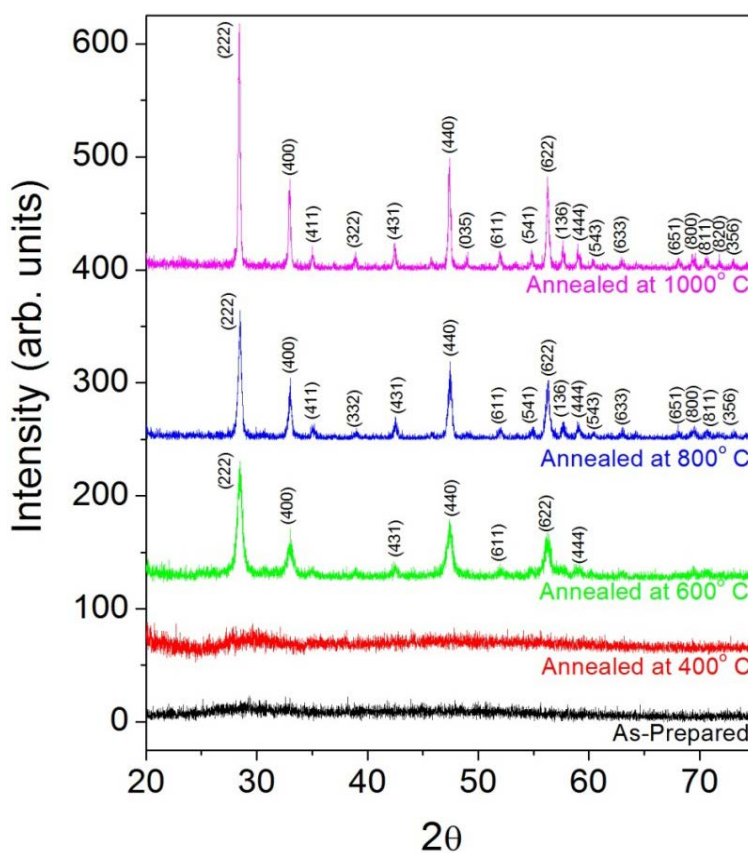
Figure A.3: X-ray diffraction patterns for Gd_2O_3 nanoparticles, as indicated. Spectra have been offset vertically for clarity

All peaks can be indexed to the Gd_2O_3 structure, as shown in Fig. 1, and no impurity phases are observed. The crystallite size, estimated using the Debye-Scherrer method, is ~20 nm for particles annealed at 600 °C, 25 nm for particles annealed at 800 °C and ~33 nm for particles annealed at 1000° C, with the particles annealed at lower temperatures appearing to be amorphous. Transmission electron microscope (TEM) images of nanoparticles annealed at 800 °C, shown in figure A.4 (a), confirm that the nanoparticle size falls between ~20 nm and ~30 nm. This image also suggests that nanoparticles have agglomerated to form clumps of roughly ~200 nm in size. Agglomeration is known to be a common problem associated with Gd_2O_3 nanoparticles synthesized using this co-precipitation method [79, 80], so this may not be associated solely with the procedure to fix the samples for TEM imaging.
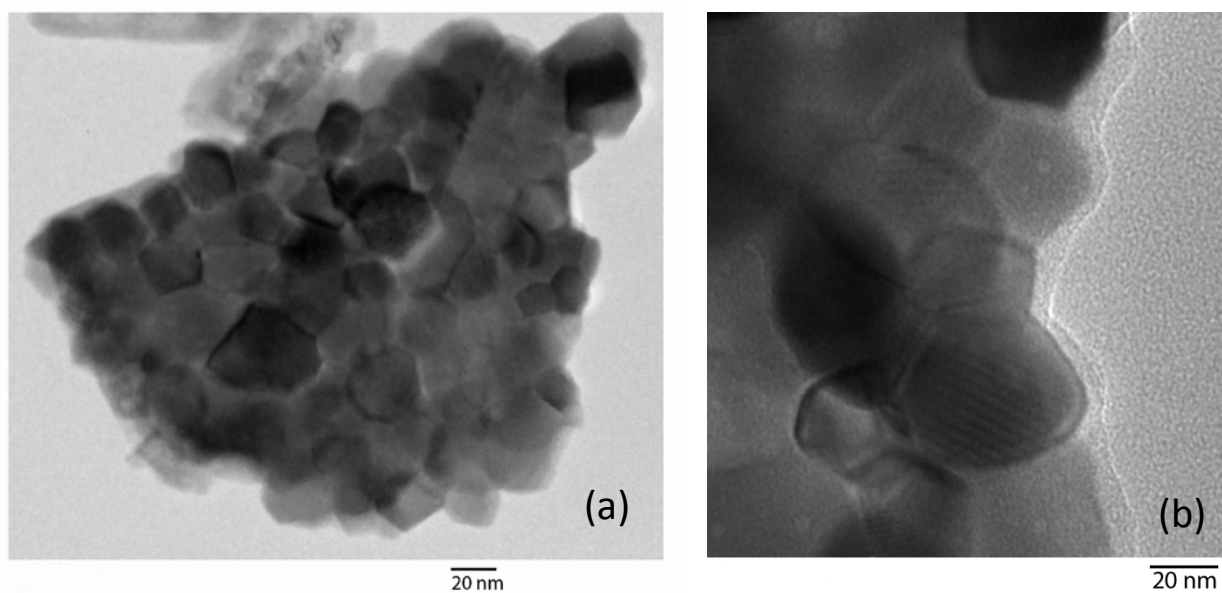
Figure A.4: TEM images of Gd_2O_3 nanoparticles (a) annealed at 800 °C (b) Annealed at 800 °C and Dextran Coated. Particles are 20 nm - 30 nm in size with the Dextran layer being ~5 nm thick

Figure A.4 (b) shows a TEM image of the nanoparticles after a dextran coating has been applied. The dextran coating can be seen as the lower contrast shell having thickness of approximately 5 nm over the Gd_2O_3 nanoparticles. Instead of coating each nanoparticle individually, the coating may cover an entire cluster of nanoparticles. TEM images of as-prepared nanoparticles (not shown) indicate that similar agglomeration is present, but to a smaller degree than observed in the annealed nanoparticles.
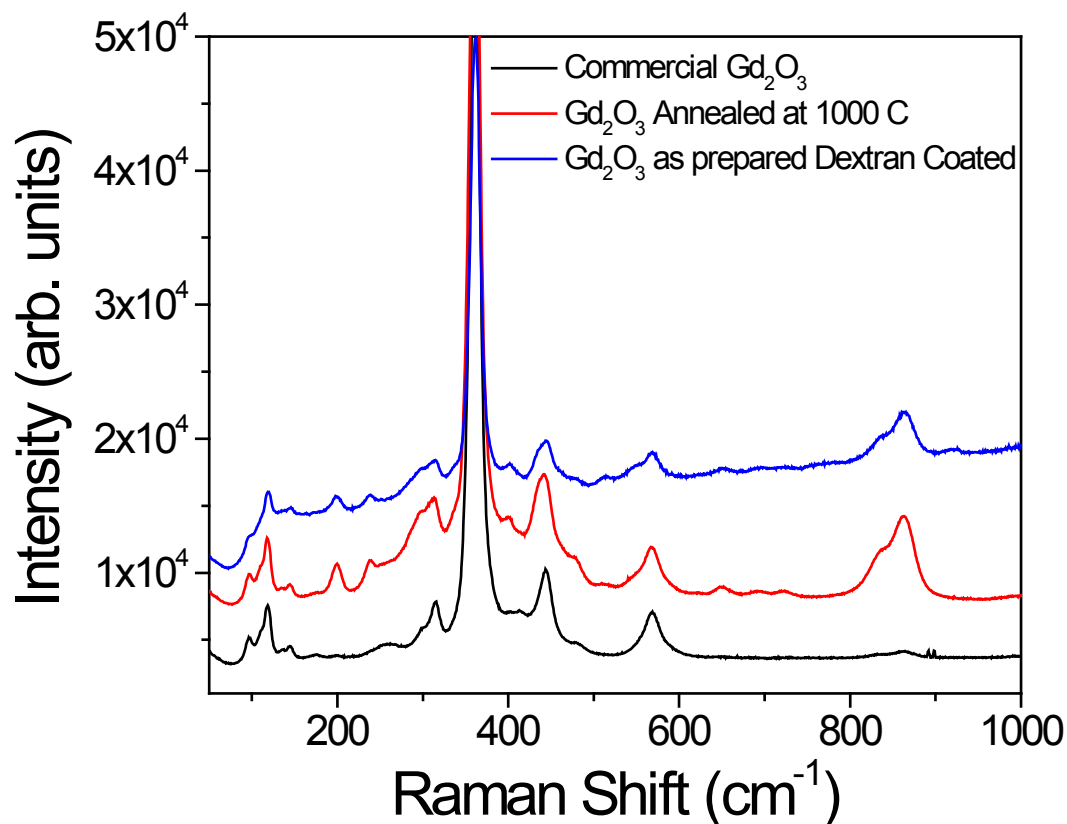
Figure A.5: Raman spectra comparison of Gd_2O_3 in bulk, nanoparticle, and nanoparticle coated with dextran

Raman spectra obtained from bulk Gd_2O_3, Gd_2O_3 nanoparticles annealed at 1000° C and

the (as-prepared) dextran coated nanoparticles are shown in Fig. A.5. The nanoparticles show

peaks at the same positions as bulk Gd_2O_3. Annealing to the nanoparticles appears to slightly

enhance the amplitude of the vibrational modes. The Raman peaks at 313, 359, 442 and 568 cm^{-1}

of the nanoparticle samples are known peaks arising from the cubic Gd_2O_3 structure [89]. Raman

spectroscopy studies confirm that both the annealed and as-prepared nanoparticles are in pure

Gd_2O_3 form with no trace of impurities.
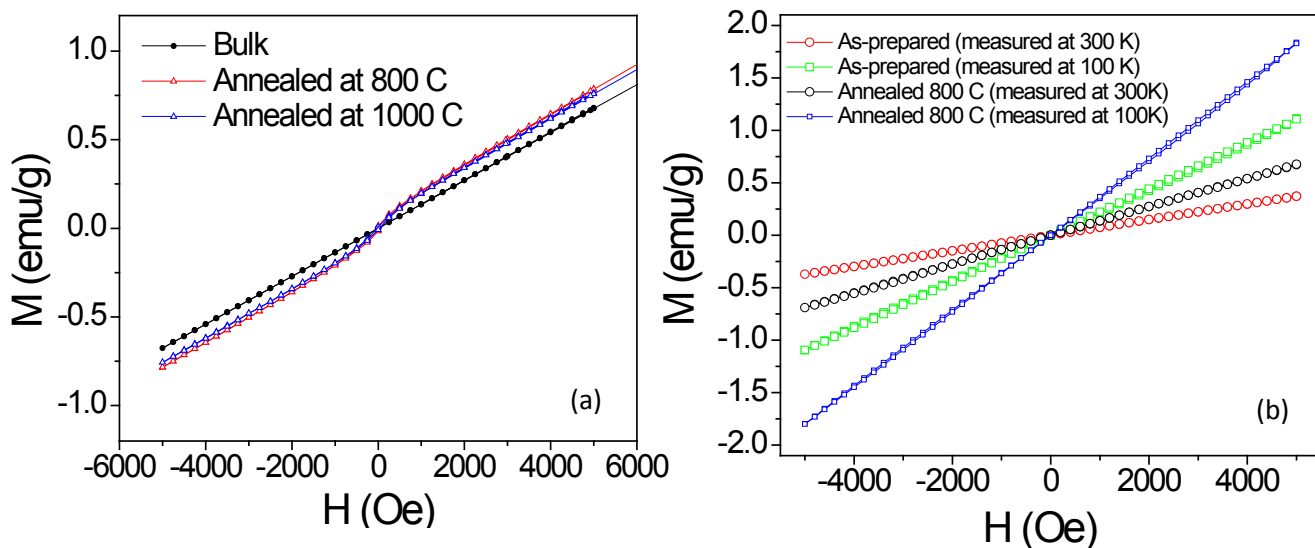
Figure A.6: (a) Magnetization curves of as-prepared and annealed at 800 ^{o}C nanoparticles, measured at room temperature and at 100 K (b) Increase in magnetization compared with bulk (commercially available) Gd_2O_3

We used room temperature magnetization measurements as an initial characterization of

the magnetic properties of the Gd_2O_3 nanoparticles. Figure A.6 (a) shows the magnetization

against applied field for bulk Gd_2O_3, the as-prepared nanoparticles and nanoparticles annealed at

800 ^{o}C, measured at room temperature. Since bulk Gd_2O_3 is paramagnetic, the M-H curve is

approximately linear over the field range studied. When measured in nanoparticles form, we see a slight increase in magnetic moment, possibly due to the additional contribution from the surface spins.

The as-prepared nanoparticles show minimal hysteresis, as expected for a paramagnetic system. The nanoparticles annealed at 800 ^{o}C show similar properties, although they have a significantly enhanced magnetization. The nanoparticles annealed at 1000 ^{o}C show qualitatively and quantitatively similar properties to the nanoparticles annealed at 800 ^{o}C, including a small non-linearity in the magnetization curve near zero field.
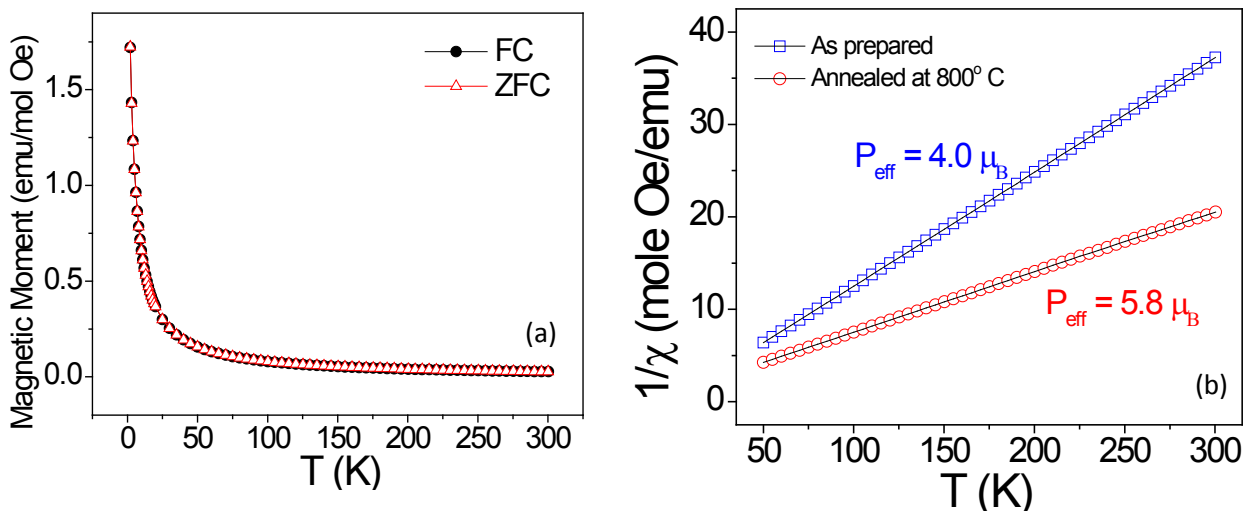
Figure A.7: (a) Field cooled and zero field cooled magnetization measurements for as-prepared nanoparticles show purely paramagnetic behavior and no ZFC/FC splitting (b) Effective moments extracted from high-temperature Curie-Weiss law fittings; annealing considerably increases the effective moment

As a further probe of the magnetic properties of these nanoparticles, we measured of the magnetization as a function of temperature between 2 K and 300 K. These data are plotted in terms of the inverse susceptibility in figure A.7 (b). The temperature dependent magnetization is consistent previously published results for Gd_2O_3 nanoparticles [79, 80]. We observed splitting in the magnetization curves measured under zero-field-cooled and field-cooled conditions (not shown), and Gd_2O_3 remains paramagnetic even at 2 K. This is consistent with [79] where it is reported that no evidence of a blocking temperature was found for Gd_2O_3 nanoparticles, suggesting that the nanoparticles remain paramagnetic down to at least 2 K. Pure gadolinium nanoparticles however exhibit superparamagnetic properties with a blocking temperature of ~ 45 K [90, 91].

The plot of $1/\chi$ vs. temperature gives a straight line consistent with Curie Law susceptibility. We estimate the effective moment of Gd as 4 μ_B for the as-prepared nanoparticles, while annealing at 800 ^{o}C increases the effective moment to 5.8 μ_B. This is much larger than the typical Fe_3O_4 moment; ~2-3 μ_B [92]. For bulk Gd_2O_3 (not shown) the effective moment is 4.1 μ_B (per Gd mole), indicating the nanoparticles have a much higher moment. We repeated these magnetic measurements three months after samples were synthesized and first measured (not shown), and found that the moment for the as-prepared sample had increased to ~5.5 μ_B, which is very close to the moment of annealed samples. The annealed samples were also re-measured after 3 months and the effective moment did not change significantly over time. We believe that some of the Gd^{3+} ions in the as-prepared samples may not have been oxidized immediately after preparation, leading to an increase of the effective moment as they oxidize. Since annealing at

high temperature completely oxidizes Gd to Gd_2O_3, no further increase in effective moment is observed.
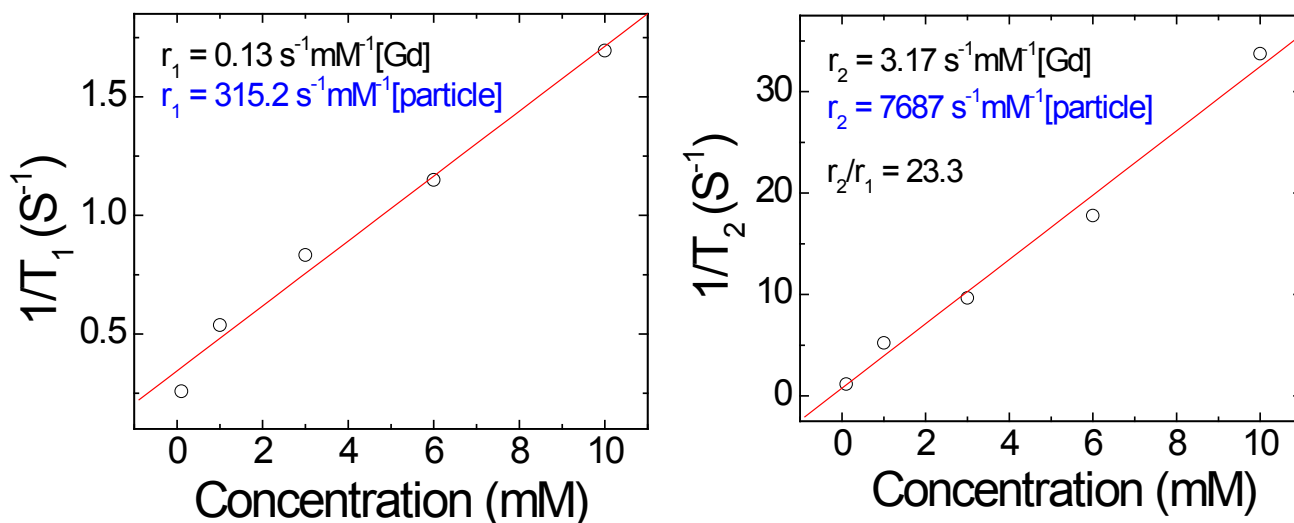
Figure A.10: T_1/T_2 measurements for as-prepared nanoparticles in 0.2 M NaOH

We also measured the relaxivity of these Gd_2O_3 nanoparticles to test their suitability as MRI contrast agents. For these measurements, as-prepared nanoparticles were suspended in a 0.2 M NaOH solution with varying concentrations from 0.1 to 10 mM [Gd]. We measured the relaxation times T_1 and T_2 as a function of concentration using a 1.5 T Bruker Minispec mq60 NMR at 37 ^oC. The slope of the plot $1/T_1$ (T_2) against concentration gives the relaxation time r_1 (r_2). Calculated per mole (by weight) of gadolinium, we find $r_1 = 0.13$ $s^{-1}mM^{-1}$, $r_2 = 3.17$ $s^{-1}mM^{-1}$ and the r_2/r_1 ratio is 23.1. For comparison, the values of r_1 for diethylene glycol (DEG) covered Gd_2O_3 nanoparticles range from 3.6 $s^{-1}mM^{-1}$ in cell culture medium for particles sized 2 - 5 nm [83] to 9.8 $s^{-1}mM^{-1}$ in 1 M hydroxylamine buffer for particles sized 5 – 10 nm [82], while polyethylene glycol (PEG) covered Gd_2O_3 of ~3 nm size yields a r_1 relaxivity of 9.4 $mM^{-1}s^{-1}$ [79]. The r_2/r_1 ratios are 3.5 and 1.2 for DEG-Gd_2O_3 and 1.4 for PEG-Gd_2O_3 respectively in these

studies. Another important measure of the relaxivity is the change in rate per nanoparticle. Using this metric, the r_1 relaxivity is 315.2 $s^{-1}mM^{-1}$, which is also somewhat smaller than what has been observed previously for Gd_2O_3 nanoparticles [93]. However, we were unable to measure the relaxation studies of the annealed nanoparticles because annealing increased the agglomeration significantly and the nanoparticles would precipitate out of the solution before the relaxivity measurements were completed. Hence we are unable to directly compare the effect annealing has on the relaxivities.

The relaxivity for Gd_2O_3 nanoparticles is well known to depend on their size. For larger Gd_2O_3 nanoparticles Fortin *et. al.* reports r_1 to be 0.1 $s^{-1}mM^{-1}$ for nanoparticles with a ~40 nm diameter [79], and McDonald *et. al.* reports r_1 to be 0.2 $s^{-1}mM^{-1}$ for nanoparticles varying from 20 nm – 40 nm [94], a reduction of almost two orders of magnitude from the values for smaller nanoparticles, and r_2/r_1 ratios of 81 and 34 respectively. In the study on 40 nm nanoparticles, in contrast to our experiments, the nanoparticle agglomeration was minimized by centrifuge filtration, although the relaxivity values are very similar to our measurements. This suggests that possible agglomeration may have had only a somewhat small effect on these relaxivity measurements. Moreover, our measurements also imply that although the crystallinity of the Gd_2O_3 nanoparticles can have a significant effect on their magnetic properties, this produces only a minimal change in their relaxivity in solution. Since contrast agents require a large value for r_1 and an r_2/r_1 ratio close to unity, this study indicates that smaller Gd_2O_3 nanoparticles are likely to make superior contrast agents to larger nanoparticles, even if the smaller nanoparticles are more amorphous.

In summary, we have found that thermal annealing at temperatures above 600 oC increases the crystallinity of Gd_2O_3 nanoparticles. This improves their magnetic properties, increasing the effective moment from 4.0 μ_B/Gd for the as-prepared nanoparticles to 5.8 μ_B/Gd for the fully crystallized samples, and produces a small ferromagnetic signal. The effective moment of as-prepared nanoparticles become very similar to annealed nanoparticles after ~3 months, most likely due to further oxidation of the non-oxidized Gd left in the sample. Neither the as-prepared nor annealed nanoparticles show NMR relaxivities that are competitive with much smaller Gd_2O_3 nanoparticles, having a small r_1 relaxation time and a high r_2/r_1 ratio. These investigations suggest that smaller, more amorphous Gd_2O_3 nanoparticles may have superior relaxivity properties than larger, more crystalline Gd_2O_3 nanoparticles, which means that low temperature synthesis techniques may provide the best method for preparing these materials for use as NMR contrast agents.

As a potential solution against the agglomerated nanoparticles difficulty to stay suspended in solution, it is possible to use gels to suspend the nanoparticles in an aqueous solution. Preliminary studies have shown that nanoparticles can be successfully suspended in agarose gel, which will be especially useful in performing relaxivity measurements more accurately.

APPENDIX B

MEASUREMENT TECHNIQUES

Magnetization Measurements

DC Magnetization measurements presented in this thesis were taken using a SQUID (Superconducting QUantum Interference Device) based Quantum Design Magnetometer (MPMS-5S) and a Quantum Design Model 6000 Particle Property Measurement System (PPMS), while the AC Magnetization measurements were taken using the PPMS. The SQUID based MPMS has a range of 2 K to 400 K with a ± 5 T maximum applied magnetic field and a measurement sensitivity of ~10^{-8} emu, while the PPMS has a range of 2 K to 400 K with a ± 9 T maximum applied magnetic field and a measurement sensitivity of ~10^{-5} emu. To prepare samples for these measurements, approximately 30 mg to 60 mg of powder samples were placed inside small gelatin capsules which were then stuffed with cotton to avoid sample movement during the measurement. The gel capsule was then mounted inside a plastic drinking straw in a fixed position by sewing it with cotton thread. The diamagnetic contribution from the capsule, thread and the straw is often negligibly small compared with the magnetic signal obtained from the sample. However, when the response was extremely small and this diamagnetic contribution was non-negligible, it was subtracted from the final measurements.

Heat Capacity Measurements

Polycrystalline samples were mixed with Ag powder on a 1:1 ratio by weight to improve the thermal conductivity and to hold the sample together, and pressed into pellets weighing ~30 mg. The pellets were mounted in a heat capacity puck with N-type thermal grease, and the measurements were done using a standard heat capacity option on the PPMS. The contribution to the heat capacity from Ag was finally subtracted from the data.

Dielectric Measurements

In order to do temperature and field dependent dielectric measurements, polycrystalline samples were pressed into pallets of approximately ~1 mm in thickness and 4 mm in diameter. Ag epoxy was used to make electrodes on the two flat sides of the pellets to use a standard parallel plate capacitor configuration. The capacitance is then given by

$$C = \frac{\varepsilon_0 \varepsilon A}{d}$$

(B.1)

where ε_0 is the permittivity of free space, ε is the permittivity of the sample, A the average electrode area and d the distance between the electrodes, i.e. the thickness of the pellet. The measurements were taken using an Agilent 4284A LCR meter using a 30 kHz frequency with the temperature and magnetic field control provided by the PPMS. Finally, the capacitance was normalized using the following formula to remove any geometric effects.

$$\frac{\varepsilon}{\varepsilon_{T=x}} = \frac{C - C_{T=x}}{C_{T=x}} \times 100$$

(B.2)

where $C_{T=x}$ is the capacitance at a particular temperature and $\varepsilon_{T=x}$ is the corresponding dielectric constant at that temperature.

Polarization Measurements

Ferroelectric polarization was obtained using an indirect method where the pyrocurrent of the samples were integrated with respect to time. Samples were prepared similar to dielectric measurements, and were placed under a high poling field of $\pm$ 200 V. Then the samples were cooled down past the transition temperature, the poling field removed, and the pyrocurrent of the samples were measured using a Keithley 6517A electrometer while warming up at a slow rate (4-6 K/min). The temperature and the magnetic field control were provided by the PPMS. The samples show a sharp pyrocurrent feature in the vicinity of the ferroelectric transition, and the pyrocurrent vanishes above the transition temperature. The measured pyrocurrent was then integrated with respect to elapsed time to obtain the spontaneous ferroelectric polarization in the sample.

REFERENCES

[1] B. B. Van Aken, J. P. Rivera, H. Schmid and M. Fiebig, *Nature,* **449**, 702-705 (2007)

[2] O. Auciello, J. F. Scott, and R. Ramesh, *Physics Today*, **51**, 22–27 (1998).

[3] I. J. Busch-Vishniac, *Physics Today,* **51**, 28 (1998).

[4] D. Khomskii, *Physics,* **2**, 20 (2009)

[5] N. Rogado, G. Lawes, D. A. Huse, A. P. Ramirez and R. J. Cava, *Solid State Communications,* **124**, 229 (2002)

[6] G. Lawes, M. Kenzelmann, N. Rogado, K. H. Kim, G. A. Jorge, R. J. Cava, A. Aharony, O. Entin-Wohlman, A. B. Harris, T. Yildirim, Q. Z. Huang, S. Park, C. Broholm, and A. P. Ramirez, *Physical Review Letters*, **93**, 247201 (2004)

[7] A. Daoud-Aladine, B. Kundys, C. Martin, P. G. Radaelli, P. J. Brown, C. Simon, and L. C. Chapon, *Physical Review B*, **80**, 220402 (2009)

[8] A. Dixit and G. Lawes, *Journal of Physics: Condensed Matter,* **21**, 456003 (2009)

[9] Stephen Blundell, Magnetism in Condensed Matter, Oxford University Press, 2001

[10] J. B. Goodenough, *Physical Review,* **100**, 564 (1955)

[11] J. Kanamori, *Journal of Physics and Chemistry of Solids,* **10**, 87 (1959)

[12] P. W. Anderson, Magnetism, Academic Press, 1963

[13] M. A. Ruderman and C. Kittel, *Physical Review*, **96**, 99 (1954)

[14] N. Setter, D. Damjanovic, L. Eng, G. Fox, S. Gevorgian, S. Hong, A. Kingon, H. Kohlstedt, N. Y. Park, G. B. Stephenson, I. Stolitchnov, A. K. Taganstev, D. V. Taylor, T. Yamada, and S. Streiffer, *Journal of. Applied Physics,* **100**, 051606 (2006)

[15] D. Damjanovic, *Reports on Progress in Physics,* **61**, 1267 (1998)

[16] H. Zheng, J. Wang, S. E. Lofland, Z. Ma, L. Mohaddes-Ardabili, T. Zhao, L. Salamanca-Riba, S. R. Shinde, S. B. Ogale, F. Bai, D. Viehland, Y. Jia, D. G. Schlom, M. Wuttig, A. Roytburd, R. Ramesh, *Science*, **303,** 661 (2004)

[17] B. Van Aken, T. T. M. Palstra, A. Filippetti, and N. A. Spaldin, *Nature Materials,* **3**, 164 (2004)

[18] J. Wang, J. B. Neaton, H. Zheng, V. Nagarajan, S. B. Ogale, B. Liu, D. Viehland, V. Vaithyanathan, D. G. Schlom, U. V. Waghmare, N. A. Spaldin, K. M. Rabe, M. Wuttig, and R. Ramesh, *Science,* **299**, 1719 (2003)

[19] T. Kimura, T. Goto, H. Shintani, K. Ishizaka, T. Arima and Y. Tokura, *Nature*, **426**, 55 (2003)

[20] G. Lawes, A. B. Harris, T. Kimura, N. Rogado, R. J. Cava, A. Aharony, O. Entin-Wohlman, T. Yildirim, M. Kenzelmann, C. Broholm, and A. P. Ramirez, *Physical Review Letters*, **95**, 087205 (2005)

[21] G. Lawes, M. Kenzelmann, and C. Broholm, *Journal of Physics: Condensed Matter,* **20** 434205 (2008)

[22] A. Dixit, G. Lawes, and A. B. Harris, *Physical Review B,* **82**, 024430 (2010)

[23] N. A. Hill, *The Journal of Physical Chemistry B,* **104**, 6694 (2000)

[24] R. Seshadri and N. A. Hill, *Chemistry of Materials*, **13**, 2892 (2001)

[25] A. A. Belik, S. Iikubo, T. Yokosawa, K. Kodama, N. Igawa, S. Shamoto, M. Azuma, M. Takano, K. Kimoto, Y. Matsui, and E. Takayama-Muromachi, *Journal of the American Chemical Society*, **129**, 971 (2007)

[26] N. Ikeda, K. Kohn, N. Myouga, E. Takahashi, H. Kitoh, and S. Takekawa, *Journal of the Physical Society of Japan,* **69,** 1526 (2000)

[27] S. Mercone, A. Wahl, A. Pautrat, M. Pollet, and C. Simon, *Physical Review B,* **69**, 174433 (2004)

[28] N. Hur, S. Park, P. A. Sharma, J. S. Ahn, S. Guba, and S. W. Cheong, *Nature*, **429**, 392 (2004)

[29] J. van den Brink and D. I. Khomskii, *Journal of Physics: Condensed Matter,* **20,** 434217 (2008)

[30] T. Tohei, H. Moriwake, H. Murata, A. Kuwabara, R. Hashimoto, T. Yamamoto, and I. Tanaka, *Physical Review B*, **79**, 144125 (2009)

[31] O. Heyer, N. Hollmann, I. Klassen, S. Jodlauk, L. Bohatý, P. Becker, J. A. Mydosh, T. Lorenz and D. Khomskii *Journal of Physics: Condensed Matter*, **18**, 471 (2006)

[32] B. Kundys, C. Simon, and C. Martin, *Physical Review B*, **77**, 172402 (2008)

[33] I. A. Sergienko and E. Dagotto, *Physical Review B,* **73**, 094434 (2006)

[34] G. H. Wannier, *Physical Review,* **79**, 357 (1950)

[35] Y. J. Choi, H. T. Yi, S. Lee, Q. Huang, V. Kiryukhin and S. W. Cheong, *Physical Review Letters,* **100,** 047601 (2008)

[36] L. Onsager, *Physical Review,* **65**, 117 (1944)

[37] L. D. Landau and E. M. Lifshitz, <u>Electrodynamics of Continuous Media,</u> Pergamon Press, 1960

[38] N. R. Wilson, O. A. Petrenko, and G. Balakrishnan, *Journal of Physics: Condensed Matter*, **19**, 145257 (2007)

[39] A. K. Singh, D. Jain, V. Ganesan, A. K. Nigam, and S. Patnaik, *Europhysics Letters*, **86**, 57001 (2009)

[40] A. B. Harris, T. Yildirim, A. Aharony, and O. Entin-Wohlman, *Physical Review B*, **73**, 184433 (2006)

[41] Z. He, J. Yamaura, and Y. Ueda, *Journal of Solid State Chemistry*, **181**, 2346 (2008)

[42] Y. Benfang, L. Meiya, J. Liu, D. Guo, L. Pei, and X. Zhao, *Journal of Physics D: Applied Physics*, **41**, 065003, (2008)

[43] D. Kothari, V. R. Reddy, A. Gupta, C. Meneghini, and G. Aquilanti, *Journal of Physics: Condensed Matter*, **22**, 356001 (2010)

[44] Y. Du, Z. X. Cheng, X. L. Wang, and S. X. Dou, *Journal of Applied Physics*, **107**, 09D908 (2010)

[45] D. O'Flynn, C. V. Tomy, M. R. Lees, and G Balakrishnan, *Journal of Physics: Conference Series*, **200**, 012149 (2010)

[46] Q. Zhang, W. Knafo, P. Adelmann, P. Schweiss, K. Grube, N. Qureshi, Th. Wolf, H. v. Lohneysen, and C. Meingast, *Physical Review B*, **84**, 184429 (2011)

[47] V. A. Khomchenko, D. A. Kiselev, M. Kopcewicz, M. Maglione, V. V. Shvartsman P. Borisov, W. Kleemann, A. M. L. Lopes, Y. G. Pogorelov, J. P. Araujo, R. M. Rubinger, N. A. Sobolev, J. M. Vieira, and A. L. Kholkin, *Journal of Magnetism and Magnetic Materials*, **321**, 1692 (2009)

[48] J. Andres, M. Cagigas, D. S. Candela, and E. Baggio-Saitovitch, *Journal of Physics: Conference Series*, **200**, 012134 (2010)

[49] L. Meddar, M. Josse, P. Deniard, C. La, G. Andre, F. Damay, V. Petricek, S. Jobic, M.-H. Whangbo, M. Maglione, and C. Payen, *Chemistry of Materials*, **21**, 5203 (2009)

[50] R. P. Chaudhury, F. Ye, J. A. Fernandez-Baca, B. Lorenz, Y. Q. Wang, Y. Y. Sun, H. A. Mook, and C. W. Chu, *Physical Review B*, **83**, 014401 (2011)

[51] R. P. Chaudhury, B. Lorenz, Y. Q. Wang, Y. Y. Sun, and C. W. Chu, *New Journal of Physics*, **11**, 033036 (2009)

[52] R. P. Chaudhury, F. Ye, J. A. Fernandez-Baca, Y. Q. Wang, Y. Y. Sun, B. Lorenz, H. A. Mook, and C. W. Chu, *Physical Review B*, **82**, 184422 (2010)

[53] T. Lancaster, S. J. Blundell, P. J. Baker, D. Prabhakaran, W. Hayes, and F. L. Pratt, *Physical Review B*, **75**, 064427 (2007)

[54] N. Rogado, M. K. Haas, G. Lawes, D. A. Huse, A. P. Ramirez, and R. J. Cava, *Journal of Physics: Condensed Matter*, **15**, 907 (2003)

[55] A. A. Mukhin, V. Yu. Ivanov, A. M. Kuz'menko, A. S. Prokhorov, A. A. Pronin, S. N. Barilo, G. L. Bychkov, and S. V. Shiryaev, *Journal of Experimental and Theoretical Physics Letters*, **91**, 147 (2010)

[56] N. Qureshi, H. Fuess, H. Ehrenberg, T. C. Hansen , C. Ritter, K. Prokes, A. Podlesnyak, and D. Schwabe, *Physical Review B*, **74**, 212407 (2006)

[57] Q. Zhang, W. Knafo, K. Grube, H. V. Lohneysen, C. Meingast, and T. Wolf, *Physica B: Physics of Condensed Matter*, **403**, 1404 (2008)

[58] R. Szymczak, M. Baran, J. Fink-Finowicki, B. Krzymanska, P. Aleshkevych, H. Szymczak, S. N. Barilo, G. L. Bychkov, and S. V. Shiryaev, *Journal of Non-Crystalline Solids*, **354**, 4186 (2008)

[59] W. Friedrich, P. Knipping, and M. v. Laue, Interferenz-Erscheinungen bei Röntgenstrahlen, Sitzungsberichte der Mathematisch-Physikalischen Classe der Königlich-Bayerischen Akademie der Wissenschaften zu München, 1912

[60] C. V. Raman, *Nature*, **121**, 501 (1928)

[61] J. R. Ferraro, K. Nakamoto, and C. W. Brown, Introductory Raman spectroscopy, Academic Press, 2003

[62] J. J. Laserna, Modern techniques in Raman spectroscopy, John Wiley & Sons, 1996

[63] V. Brazdova, M. V. Ganduglia-Pirovano, and J. Sauer, *Journal of Physical Chemistry B*, **109**, 394 (2005)

[64] F. Yonezawa, S. Sakamoto, and M. Hori, *Physical Review B*, **40**, 636 (1989)

[65] S. W. Cheong, A. S. Cooper, L. W. Rupp Jr., B. Batlogg, J. D. Thompson, Z. Fisk, *Physical Review. B,* **44**, 9739 (1991)

[66] P. Kharel, A. Kumarasiri, A. Dixit, N. Rogado, R. J. Cava, and G. Lawes, *Philosophical Magazine,* **89,** 1923 (2009)

[67] A. Kumarasiri and G. Lawes, *Physical Review B*, **84**, 064447 (2011)

[68] N. R. Wilson, O. A. Petrenko and G. Balakrishnan, *Journal of Physics: Condensed Matter*, **19**, 145257 (2007)

[69] N. Rogado, G. Lawes, D. A. Huse, A. P. Ramirez and R. J. Cava, *Solid State Communications*, **124**, 229 (2002)

[70] M. Kenzelmann, A. B. Harris, A. Aharony, O. Entin-Wohlman, T. Yildirim, Q. Huang, S. Park, G. Lawes, C. Broholm, N. Rogado, R. J. Cava, K. H. Kim, G. Jorge, and A. P. Ramirez, *Physical Review B*, **74**, 014429 (2006)

[71] D. L. Fox, D. R. Tilley and J. F. Scott, *Physical Review B,* **21**, 2926 (1980)

[72] C. Caizera and I. Hrianca, *Europian Physical Journal B,* **31**, 391 (2003)

[73] E. M. Haacke, R. W. Brown, M. R. Thompson, and R. Venkatesan, <u>Magnetic Resonance Imaging; Physical Principles and Sequence Design</u>, John Wiley and Sons, 1999

[74] P. Caravan, J. J. Ellison, T. J. McMurry, and R. B. Lauffer, *Chemical Review,* **99**, 2293 (1999)

[75] P. Caravan, *Chemical Society Review*, **35**, 512 (2006)

[76] M. Mikawa, H. Kato, M. Okumura, M. Narazaki, Y. Kanazawa, N. Miwa, and H. Shinohara, *Bioconjugate Chemistry*, **12**, 510 (2001)

[77] L. Babes, B. Denizot, G. Tanguy, J. J. Le Jeune, and P. Jallet, *Journal of Colloid and Interface Science*, **212**, 474 (1999)

[78] P. Drake, H. J. Cho, P. S. Shih, C. H. Kao, K. F. Lee, C. H. Kuo, X. Z. Linb and Y. J. Lin, *Journal of Materials Chemistry,* **17**, 4914 (2007)

[79] M. A. Fortin, R. M. Petoral Jr., F. Soderlind, A. Klasson, M. Engstrom, T. Veres, P. O. Kall, and K. Uvda, *Nanotechnology*, **18**, 395501 (2007)

[80] M. A. McDonald, K. L. Watkin, *Academic Radiology,* **13**, 932 (2006)

[81] J. Miyawaki, M. Yudasaka, H. Imai, H. Yorimitsu, H. Isobe, E. Nakamura, and S. Iijima, *Journal of Physical Chemistry B*, **110**, 5179 (2006)

[82] M. Engström, A. Klasson, H. Pedersen, C. Vahlberg, P O. Käll, and K. Uvdal, *Magnetic Resonance Materials in Physics,* **19,** 180 (2006)

[83] A. Klassona, M. Ahrenc, E. Hellqvistd, F. Soderlindc, A. Rosend, P. O. Kallc, K. Uvdalc and M. Engstrom, *Contrast Media & Molecular Imaging*, **3**, 106 (2008)

[84] M. Ahren, L. Selegard, A. Klasson, F. Soderlind, N. Abrikossova, C. Skoglund, T. Bengtsson, M. Engstrom, P. O. Kall, and K. Uvdal, *Langmuir,* **26**, 5753 (2010)

[85] C. Louis, R. Bazzi, Marco A. Flores, W. Zheng, K. Lebbou, O. Tillement, B. Mercier, C. Dujardin, and P. Perriat, *Journal of Solid State Chemistry,* **173**, 335 (2003)

[86] C. Le Luyer, A. Garcıa-Murillo, E. Bernstein and J. Mugnier, *Journal of Raman Spectroscopy,* **34**, 234 (2003)

[87] Y. Lia, N. Chena, J. Zhoua, S. Songa, L. liua, Z. Yina, C. Cai, *Journal of Crystal Growth,* **265**, 548 (2004)

[88] H. Guoa, X. Yang, T. Xiao, W. Zhanga, L. Loub, and J. Mugnier, *Applied Surface Science*, **230,** 215 (2004)

[89] G. Hai, Z. Weiping, Y. Min, L. Liren, and X. Shangda, *Journal of Rare Earths,* **22**, 365 (2004)

[90] J. A. Nelson, L. H. Bennett, and M. J. Wagner, *Journal of American Chemical Society,* **124**, 2979 (2002)

[91] Z. C. Yan, Y. H. Huang, Y. Zhang, H. Okumura, J. Q. Xiao, S. Stoyanov, V. Skumryev, and G. C. Hadjipanayis, *Physical Review B*, **67**, 054403 (2003)

[92] N. Pérez, F. Bartolomé, L. M. García, J. Bartolomé, M. P. Morales, C. J. Serna, A. Labarta, and X. Batlle, *Applied Physical Letters,* **94**, 093108 (2009)

[93] J. L. Bridot, A. C. Faure, S. Laurent, C. Riviere, C. Billotey, B. Hiba, M. Janier, V. Josserand, J. L. Coll, L. V. Elst, R. Muller, S. Roux, P. Perriat, and O. Tillement , *Journal of American Chemical Society,* **129**, 5076 (2007)

[94] M. A. McDonald and K. L. Watkin, *Investigative Radiology,* **38**, 305 (2003)

ABSTRACT

EFFECTS OF TRANSITION METAL DOPING ON MULTIFERROIC ORDERING IN $Ni_3V_2O_8$ AND $FeVO_4$

by

AKILA KUMARASIRI

December 2012

Advisor   **:** Dr. Gavin Lawes

Major   **:** Physics

Degree   **:** Doctor of Philosophy

We have studied the effects of doping both non-magnetic and magnetic ions on the phase transitions and multiferroic ordering in two multiferroic oxides; $Ni_3V_2O_8$ and $FeVO_4$. Magnetic, dielectric, specific heat, polarization and AC susceptibility measurements were used to track changes in phase transition temperatures. We found that the two higher temperature magnetic transitions in $Ni_3V_2O_8$; $T_H = 9.1$ K and $T_L = 6.3$ K are suppressed to lower temperatures with all transition metal dopants. For Zn doping, the rates of the suppression of both T_H and T_L with dopant fraction are consistent with simple site dilution for two-dimensional spin systems, with the suppression of T_H consistent with Ising spins and the suppression of T_L consistent with Heisenberg spins. However, samples remain multiferroic at least up to 15% Zn doping. Conversely, spin-1/2 Cu doping strongly suppresses both transitions, for which the multiferroic

magnetic structure is completely suppressed at only 10% Cu doping. However, below 10% Cu doping, the samples show enhanced ferroelectric polarization, and a sizable net magnetization also develops.

With spin-3/2 Co doping, suppression is very small, with the multiferroic transition persisting even at 30% doping and the material showing $Ni_3V_2O_8$ magnetic characteristics up to 80% doping. On the Co rich side of the composition, we find that the magnetic ordering temperatures for $Co_3V_2O_8$ are suppressed rapidly with Ni doping. With higher spin dopants (e.g. spin-2 Fe and spin-5/2 Mn), suppression remains fairly low. We also present phase diagrams for $(Ni_{1-x}M_x)_3V_2O_8$ (M = Zn, Cu, Co, Fe and Mn). These studies suggest that the spin structures in $Ni_3V_2O_8$ responsible for the development of ferroelectric order are relatively robust against perturbations produced by both magnetic and non-magnetic dopants, with the most significant disruption of the magnetic structure developing for Cu doping.

In the case of $FeVO_4$, we find that the magnetoelectric coupling in $FeVO_4$ is remarkably robust to dopants with minimal suppression in transition temperatures for 3 transition metal dopants, Zn, Cr and Fe. We observe clear reversible polarization even at 20% doping suggesting the multiferroic order persists even at a large doping fraction. It is possible that the low symmetry and the 3-dimensional spin structure of $FeVO_4$ are responsible for this remarkable robustness against dopants.

These results indicate multiferroic ordering in $Ni_3V_2O_8$ and $FeVO_4$ show high resilience to dopants which can be extremely important in tuning the properties of multiferroics in general. Cu doped $Ni_3V_2O_8$ studies show it is possible to develop a sizable net magnetization simultaneously with strong polarization and good magnetoelectric coupling which is a much desirable property to have for device development.

AUTOBIOGRAPHICAL STATEMENT

Akila D. Kumarasiri
dv4364@wayne.edu

EDUCATION

- Ph.D. (Physics), Wayne State University, August 2012

- M.Sc. (Physics), Wayne State University, May 2010

- B.Sc. (Honors) in Engineering Physics, University of Colombo, Sri Lanka, August 2005

PUBLICATIONS

1. **A. Kumarasiri** and G. Lawes, Control of the multiferroic transition in $Ni_3V_2O_8$ by transition metal doping, *Physical Review B,* **84**, 064447 (2011)

2. P. Kharel, **A. Kumarasiri**, A. Dixit, N. Rogado, R. J. Cava, and G. Lawes, Scaling behavior of magnetic transitions in $Ni_3V_2O_8$, *Philosophical Magazine*, **89**, 1923 (2009)

3. T. N. Narayanan, B. P. Mandal, A. K. Tyagi, **A. Kumarasiri**, X. Zhan, M. W. Hahm, M. R. Anantharaman, G. Lawes and P. M. Ajayan, Hybrid Multiferroic Nanostructures with Magnetic-Dielectric Coupling, Nano Letters (2012, accepted and in production)

4. **A. Kumarasiri**, M. J. Allen and G. Lawes, Effect of annealing temperature on magnetic properties of Gd_2O_3 nanoparticles, manuscript under preparation

5. **A. Kumarasiri**, A. Dixit and G. Lawes, Stability of Multiferroic Transition in $FeVO_4$ against Transition Metal Doping, manuscript under preparation

6. **A. Kumarasiri** and U. J. Sonnadara, Performance of an artificial neural network on forecasting the daily occurrence and annual depth of rainfall at a tropical site, *Hydrological Processes,* **22**, 3535 (2008)

7. **A. Kumarasiri**, U. J. Sonnadara, Rainfall Forecasting: An Artificial Neural Network approach, Institute of Physics, Sri Lanka, Proceedings of the 22nd Technical Session (2006)

AWARDS

- Graduate Dissertation Fellowship, Summer 2012

- MIND scholarship, 2004 - 2005, a scholarship offered for excellence in undergraduate studies by the Munasinghe Institute for Development (MIND), Sri Lanka